A MEASUREMENT OF $W\gamma$ AND $Z\gamma$ CROSS SECTIONS IN THE MUON CHANNEL IN $\sqrt{s} = 1.8$ TeV $\bar{\text{p}}$-p COLLISIONS

BY

CHRISTOPHER B. LUCHINI

B.S., New Mexico State University, 1986
M.S., University of Illinois at Urbana-Champaign, 1990

THESIS

Submitted in partial fulfillment of the requirements
for the degree of Doctor of Philosophy in Physics
in the Graduate College of the
University of Illinois at Urbana-Champaign, 1994

Urbana, Illinois

UNIVERSITY OF ILLINOIS AT URBANA-CHAMPAIGN

THE GRADUATE COLLEGE

DECEMBER 17, 1993

WE HEREBY RECOMMEND THAT THE THESIS BY

CHRISTOPHER B. LUCHINI

ENTITLED A MEASUREMENT OF Wγ AND Zγ CROSS SECTIONS IN
THE MUON CHANNEL IN $\sqrt{S} = 1.8$ TEV $\overline{P}$-P COLLISION

BE ACCEPTED IN PARTIAL FULFILLMENT OF THE REQUIREMENTS FOR

THE DEGREE OF DOCTOR OF PHILOSOPHY

Steven Errede
Director of Thesis Research

Shau-jin Chang
Head of Department

Committee on Final Examination†

Steven Errede
Chairperson

Munir H. Nayfeh

Lorella M. Jones

† Required for doctor's degree but not for master's.

O-517

UNIVERSITY OF ILLINOIS AT URBANA-CHAMPAIGN

GRADUATE COLLEGE DEPARTMENTAL FORMAT APPROVAL

THIS IS TO CERTIFY THAT THE FORMAT AND QUALITY OF PRESENTATION OF THE THESIS

SUBMITTED BY Christopher B. Luchini AS ONE OF THE

REQUIREMENTS FOR THE DEGREE OF Doctor of Philosophy

ARE ACCEPTABLE TO THE Department of Physics.

Full Name of Department, Division or Unit

January 21, 1994

Date of Approval

Departmental Representative

A MEASUREMENT OF $W\gamma$ AND $Z\gamma$ CROSS SECTIONS IN THE MUON CHANNEL IN $\sqrt{s} = 1.8$ TEV $\bar{\text{p}}$-p COLLISIONS.

Christopher B. Luchini, Ph.D.
Department of Physics
University of Illinois at Urbana-Champaign, 1994
Professor Steven Errede, Advisor

We have measured the production cross sections × decay branching ratios for $W+\gamma$ and $Z+\gamma$ in the muon channel in $\sqrt{s} = 1.8\ TeV$ $\bar{\text{p}}$-p collisions, from $3.54 \pm 0.24\,pb^{-1}$ of muon W and Z data from the CDF 1988-89 Tevatron collider run. For photons in the central region ($|\eta| < 1.1$) of the CDF detector with transverse energies $E_T^{\gamma} > 5.0$ GeV and lepton-photon angular separation $\Delta R_{\ell\gamma} > 0.7$, 5 $W\gamma$ candidates and 2 $Z\gamma$ candidates were observed. From these events, the $\sigma \cdot BR(W+\gamma)$ and $\sigma \cdot BR(Z+\gamma)$ cross sections for the muon samples are measured, and compared with Standard Model predictions. We also determined the cross section ratios, $W\gamma/W$, $Z\gamma/Z$ and $W\gamma/Z\gamma$, which, along with with the previous CDF measurement(s) of the W/Z cross section ratio provide new insight on the Standard Model, and are sensitive to anomalous couplings of the W and Z bosons. Using the $W\gamma$ and $Z\gamma$ absolute cross section measurements, the absence of an excess of hard photons accompanying W and Z boson production enables us to obtain direct limits on anomalous $WW\gamma$, $ZZ\gamma$ and $Z\gamma\gamma$ couplings. For saturation of unitarity, these experimental limits impose constraints on possible internal (composite) structure for the W and Z bosons with compositeness scale sensitivity up to $\Lambda_W \sim 1\ TeV$ and $\Lambda_Z \sim 250-500$ GeV, respectively. These compositeness scale limits probe the possible internal structure of the W to $\sim< 2 \times 10^{-4} fm$ and internal structure of the Z to $\sim< 4-7 \times 10^{-4} fm$. Limits on the anomalous $W\gamma$ and $Z\gamma$ couplings also impose constraints on the higher order static and transition EM moments of the W and Z boson, respectively. The muon channel measurements were combined

with those made from the electron channel to arrive at $\mu + e$ combined $\sigma \cdot BR(W + \gamma)$ and $\sigma \cdot BR(Z + \gamma)$ absolute cross sections, and limits on the anomalous couplings for combined $\mu + e$ $W\gamma$ and $Z\gamma$.

Dedication

To my parents, Ben and Ingrid, who started me on this journey,

and to Laura who helped me finish it.

Acknowledgements

First and foremost, I would like to thank my family, for ingraining in me a love of exploration and discovery, without which I would never have started on this journey. (Be sure to read this through to the end, there will be a quiz.)

I would like to thank my advisor, Steve Errede, for his patience, perseverance, and his rabid attention to detail. This last, though it came close to driving this experimenter insane, has paid off, and I hope, rubbed off.

I would like to thank Doug Benjamin, Mary Roach, and the rest of the members of the DiBoson group, for all the work that went into making all the parts and pieces of this analysis come together.

Dave and Ray, for the many glasses of brew, the many hours of talk, and the occasional muddy climb through the guts of some subterranean hole that made the time in front of a terminal bearable.

For the many friends not yet named, the chili dinners, strange oriental cooking, coffee house chats, the one perfect shot, taser wars in the dark, late night phone calls, and Winkie's on Wednesdays.

Laura who has made me realize that physics, despite it's allure, is not the be all and end all of existence (as well as making me come home at a reasonable hour).

This research was supported in part by the U.S. Department of Energy under contracts DE-AC02-76ER-01195 and DOE-FG02-91ER-40677, and the A.P. Sloan Foundation.

TABLE OF CONTENTS

LIST OF TABLES

LIST OF FIGURES

Chapter 1

$W\gamma$ and $Z\gamma$ Production

1.1 Introduction

The Standard Model (SM) of electroweak interactions unifies the electromagnetic and weak interactions into a single interaction described by the gauge group $SU(2)_L \otimes U(1)_Y$. This theory predicts the existence of the $W^{\pm}$ vector bosons as carriers of the charged weak currents and two neutral vector bosons as carriers of the neutral currents, the γ and the Z^0. The measurement of W and Z production cross sections and decay properties in $\sqrt{s} = 1.8\ TeV$ $\bar{\text{p}}$-p collisions tests the strength and nature of the couplings of gauge boson to fermions (quarks and leptons). The measurement of the $W^{\pm}\gamma$ and $Z^0\gamma$ di-boson production cross sections and final-state kinematics provides an experimental test of the predicted strength and nature of the trilinear gauge boson couplings between these particles and also simultaneously provides information on the static and transition EM moments of the of the W and Z bosons[1, 2] respectively.

Additionally, composite models of W and Z bosons predict cross sections for $W\gamma$ and $Z\gamma$ production well above that for the Standard Model. [3].

The inclusive muon W and Z data samples from the 1988-89 collider run were used as a starting point for this analysis, since the $W\gamma$ and $Z\gamma$ events of interest for this measurement are contained within the inclusive W and Z data samples. The same event selection as was used in the measurement of the muon channel inclusive W and Z cross sections[4], and the W/Z cross section ratios[5], were used in this analysis, with the additional requirement that the events contain a high E_T isolated photon.

The measured production cross section × branching ratio, $\sigma \cdot BR(W + \gamma)$ and $\sigma \cdot BR(Z + \gamma)$, were used to obtain limits on the respective $W\gamma$ and $Z\gamma$ anomalous couplings, as well as limit on the static and transition electromagnetic moments of the W and Z bosons.

The small integrated luminosity presently available for studying the rare $W\gamma$ and $Z\gamma$ processes, means that the measurement of $W\gamma$ and $Z\gamma$ cross sections and limits on anomalous $WW\gamma$, $ZZ\gamma$ and $Z\gamma\gamma$ couplings will have limited statistical precision. The detailed analysis presented here is part of a foundation for a series of progressively more powerful measurements to be made over the next decade as more luminosity is acquired. In the Standard Model the universal coupling of gauge bosons to fermions allows the combining of the individual muon and electron $W\gamma$ and $Z\gamma$ cross section results in order to decrease the statistical uncertainties on the measurement of these cross sections.

Chapter 2

Theory of $W\gamma$ and $Z\gamma$ Production

The Feynman diagrams for $W\gamma$ and $Z\gamma$ production and decay are shown in Figures 2.1 and 2.2.

2.1 $W\gamma$ Theory

For $W\gamma$, the processes of interest are the trilinear gauge coupling diagrams, Figures 2.1c & 2.1d. These diagrams are distinct only in the limit of a zero width W, since the W has non-zero width ($\Gamma_W = 2.1$ GeV), these diagrams represent different kinematic regions of the same process. The processes represented by Figures 2.1a, 2.1b and 2.1e also produce events with a W and γ, though with different kinematics. The Feynman diagrams shown in Figures 2.1a & 2.1b for the **u**- and **t**-channel processes are associated with initial-state radiation from the incoming quark lines. The processes shown in Figure 2.1c and 2.1e are known as radiative W decay (Figure 2.1e is the final state inner bremsstrahlung diagram). In the limit of a zero width W it is possible to distinguish these different processes by a measurement of the invariant mass of the $W\gamma$ system. However the W boson has a non-zero total width, hence in the vicinity of

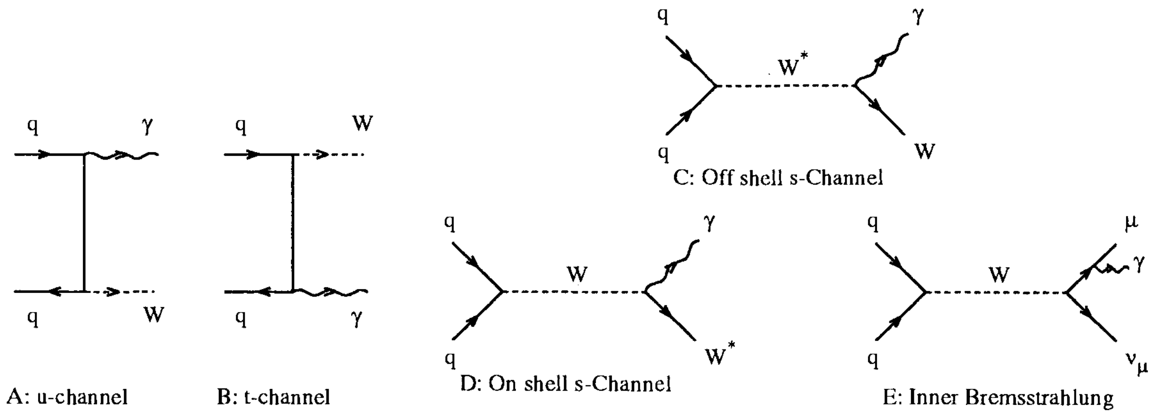

A: u-channel B: t-channel C: Off shell s-Channel D: On shell s-Channel E: Inner Bremsstrahlung

Figure 2.1: Feynman diagrams for $W\gamma$

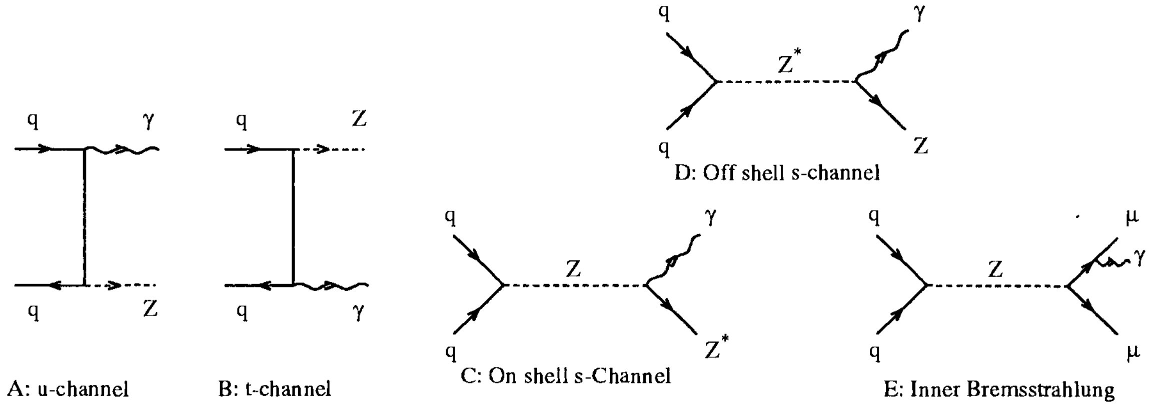

A: u-channel B: t-channel C: On shell s-Channel D: Off shell s-channel E: Inner Bremsstrahlung

Figure 2.2: Feynman diagrams for $Z\gamma$

the W mass, these processes are indistinguishable in the final state; their amplitudes must be added together coherently in order to produce a matrix element which preserves electromagnetic gauge invariance[6].

The most general effective Lagrangian[7] compatible with Lorentz and electromagnetic gauge invariance for the processes shown in Figures 2.1 is

$$\begin{aligned}\mathcal{L}_{WW\gamma} \;=\;& -ie\Big[W^\dagger_{\mu\nu}W^\mu A^\nu - W^\dagger_\mu A_\nu W^{\mu\nu} \\ & +\kappa_f W^\dagger_\mu W_\nu F^{\mu\nu} + \frac{\lambda_f}{M_W^2} W^\dagger_{\lambda\mu} W^\mu_\nu F^{\nu\lambda} \\ & +\tilde{\kappa}_f W^\dagger_\mu W_\nu F'^{\mu\nu} + \frac{\tilde{\lambda}_f}{M_W^2} W^\dagger_{\lambda\mu} W^\mu_\nu F'^{\nu\lambda}\Big]\end{aligned} \tag{2.1}$$

Where A^{μ} and W^{μ} are the photon and W^{-} fields, respectively, and $W_{\mu\nu} = \partial_{\mu} W_{\nu} - \partial_{\nu} W_{\mu}$, $F_{\mu\nu} = \partial_{\mu} A_{\nu} - \partial_{\nu} A_{\mu}$, $F^{'}_{\mu\nu} = \frac{1}{2}\epsilon_{\mu\nu\rho\sigma} F^{\rho\sigma}$, e is the charge of the proton, and M_W is the W mass. The photon is taken to be on shell, and both the virtual and on-shell W couple to essentially massless fermions allowing $\partial_{\mu} W^{\mu} = 0$.

The $WW\gamma$ vertex function can also be used to describe the behavior of the $WW\gamma$ for p̄-p→ $W^{\pm}\gamma$. The vertex function is [8]:

$$\begin{aligned}
\Gamma^{\alpha\beta\mu}(q_1, q_2, P) \; = & \\
& \mp\frac{1}{2}\Big[(2 + \Delta\kappa_f)(q_1 - q_2)^{\mu} g^{\alpha\beta} \\
& + \frac{\lambda_f}{M_W^2}\,(q_1 - q_2)^{\mu}\,(P^2 g^{\alpha\beta} - 2P^{\alpha}P^{\beta}) \\
& - 4\,P^{\beta} g^{\mu\alpha} \; + \; 2\,(2 + \Delta\kappa_f + \lambda_f)\,P^{\alpha} g^{\mu\beta} \\
& + 2\,(\tilde{\kappa}_f + \tilde{\lambda}_f)\,\epsilon^{\mu\alpha\beta\rho} q_{2\rho} \\
& + \frac{\tilde{\lambda}_f}{M_W^2}\,(q_1 - q_2)^{\mu} \epsilon^{\alpha\beta\rho\sigma} P_{\rho}\,(q_1 - q_2)_{\sigma}\Big]
\end{aligned} \tag{2.2}$$

Here P and q_1 are the four momenta of the incoming and outgoing W boson respectively (Lorentz indices μ and α respectively), and q_2 is the four momentum of the final state on-shell photon (Lorentz index β).

The tree-level Standard Model predictions for the values of the momentum-dependent form factors are $\Delta\kappa_f = \kappa_f - 1 = \lambda_f = \tilde{\kappa}_f = \tilde{\lambda}_f = 0$. The form factors $a_f = \Delta\kappa_f$, λ_f, $\tilde{\kappa}_f$, and $\tilde{\lambda}_f$ are assumed to be of the generalized dipole form [6]:

$$a_f(P^2 = \hat{s},\; \bar{q}^2 = M_W^2,\; q^2 = 0) \; = \; \frac{a_0}{(1 + \hat{s}/\Lambda_W^2)^n} \tag{2.3}$$

The anomalous contributions to the $W\gamma$ helicity amplitudes grow like $\sqrt{\hat{s}}/M_W$ for $\Delta\kappa$, $\tilde{\kappa}$ and $(\sqrt{\hat{s}}/M_W)^2$ for λ, $\tilde{\lambda}$. The form factor scale Λ_W represents the scale at which new physics becomes important in the weak boson sector, due to a composite structure of the W boson. The choice of the exponent $n = 2$ guarantees that unitarity is preserved. If the exponent is sufficiently above the minimum value of 1/2 (1) for κ_f, $\tilde{\kappa}_f$ (λ_f, $\tilde{\lambda}_f$) then one ensures that $W\gamma$ production is suppressed at energies $\sqrt{\hat{s}} >> \Lambda_W >> M_W$, where multiple weak boson or resonance phenomena are expected to dominate [7]. The behavior of the form factors is such that they stay essentially constant for $\hat{s} << \Lambda_W^2$ and start to decrease only when the scale Λ_W is passed, in analogy to the behavior associated with the well-known nucleon form factors. The Fourier transform of the form factor, with a form factor power of $n = 2$ corresponds to a Yukawa potential.

For an arbitrary spin-S particle, $2S + 1$ electromagnetic moments are allowed. Thus, the W vector boson is expected to have a magnetic dipole moment and an electric quadrupole moment in the Standard Model. The W electric dipole and magnetic quadrupole moments arrise from terms in the vertex function involving the $\tilde{\kappa}$ and $\tilde{\lambda}$ parameters, and are $\mathcal{P}-$odd and violate $\mathcal{CP}$ (i.e. violate $\mathcal{T}$). Note that the SM predictions for higher order corrections to κ, λ, etc, are expected to be of order α. In the SM of electro-weak interaction, at the tree level, the relativistic $WW\gamma$ anomalous couplings κ, λ, $\tilde{\kappa}$, and $\tilde{\lambda}$, are related, in the static limit ($E_\gamma \to 0$), to the classical parameters (with $\hbar = c = 1$)

$$\begin{array}{rcrl} \mu_W & = & \frac{e}{2M_W}(1+\kappa+\lambda) & \text{Magnetic Dipole Moment} \\ Q^e_W & = & -\frac{e}{M_W^2}(\kappa-\lambda) & \text{Electric Quadrupole Moment} \\ d_W & = & \frac{e}{2M_W}(\tilde{\kappa}+\tilde{\lambda}) & \text{Electric Dipole Moment} \\ Q^m_W & = & -\frac{e}{M_W^2}(\tilde{\kappa}-\tilde{\lambda}) & \text{Magnetic Quadrupole Moment} \\ < R_W^2 > & = & \frac{1}{M_W^2}(\kappa+\lambda) & \text{Mean-Squared Charge Radius} \end{array}$$

2.2 Unitarity Constraints for $W\gamma$

Partial wave unitarity places restrictions on the reduced amplitudes, $A^W_{\lambda_W\lambda_\gamma}$, for anomalous $WW\gamma$ couplings. Since the reduced amplitudes contain $\Delta\kappa$ and λ terms, theoretical limits on these anomalous parameters can be obtained. There are two such unitarity restrictions, one associated with $W+\gamma$ production and another associated with W^+W^- production. The unitarity restriction for $W+\gamma$ production is [6, 8]:

$$\sum_{\lambda_W\lambda_\gamma} \left| A^W_{\lambda_W\lambda_\gamma} \right|^2 < \frac{3\sin^2\theta_W}{\alpha^2(\hat{s})\left(1-\frac{M_W^2}{\hat{s}}\right)} \tag{2.4}$$

where λ_W, λ_γ are the final-state W boson and photon helicities, respectively. For our assumed generalized dipole form factor (Equation 2.3) and form factor power ($n = 2$), unitarity is violated in the $W+\gamma$ process if

$$\frac{(\frac{\hat{s}}{M_W^2}-1)}{(1+\frac{\hat{s}}{\Lambda_W^2})^4} \left[(\Delta\kappa+\lambda)^2 + \left(\frac{\hat{s}}{M_W^2}\right) \left(\Delta\kappa\left(\frac{M_W^2}{\hat{s}}\right)+\lambda\right)^2 \right] \geq \frac{6\sin^2\theta_W}{\alpha^2(\hat{s})} \tag{2.5}$$

over the $\sqrt{\hat{s}}$ range $M_W < \sqrt{\hat{s}} < 1.8$ TeV.

For W^+W^- production, the unitarity restriction is [6, 8]:

$$\sum_{\lambda_{W^+}\lambda_{W^-}} \left| A^{W}_{\lambda_{W^+}\lambda_{W^-}} \right|^2 < \frac{3\,(3-6\sin^2\theta_W + 8\sin^4\theta_W)}{5\alpha^2(\hat{s})\left(1-\frac{4M_W^2}{\hat{s}}\right)^{\frac{3}{2}}} \tag{2.6}$$

where λ_{W^+}, λ_{W^-} are the final-state W^+, W^- boson helicities, respectively. For the assumed form factor, unitarity is violated in the W^+W^- process if

$$\begin{aligned} &\frac{(1-\frac{4M_W^2}{\hat{s}})^{\frac{3}{2}}}{(1+\frac{\hat{s}}{\Lambda_W^2})^4} \left[\left(\frac{\hat{s}}{M_W^2}\right)(\Delta\kappa+\lambda)^2 + \frac{1}{2}\left(\frac{\hat{s}}{M_W^2}\right)^2\lambda^2 + \frac{1}{4}\left(\frac{\hat{s}}{M_W^2}\right)^2\Delta\kappa^2\right] \\ &\qquad \geq \frac{3\,(3-6\sin^2\theta_W + 8\sin^4\theta_W)}{5\alpha^2(\hat{s})} \end{aligned} \tag{2.7}$$

over the $\sqrt{\hat{s}}$ range $2M_W < \sqrt{\hat{s}} < 1.8$ TeV.

If only a single anomalous coupling is assumed to be non-zero at a time, then for $\Lambda_W >> M_W$ and the assumed dipole form factor and form factor power, the unitarity limits are:

$$W\gamma: \quad |\Delta\kappa| < \frac{37.1\ \text{TeV}}{\Lambda_W} \quad (\lambda = 0) \quad \text{and} \quad |\lambda| < \frac{3.9\ \text{TeV}^2}{\Lambda_W^2} \quad (\Delta\kappa = 0) \tag{2.8}$$

$$W^+W^-: \quad |\Delta\kappa| < \frac{7.3\ \text{TeV}^2}{\Lambda_W^2} \quad (\lambda = 0) \quad \text{and} \quad |\lambda| < \frac{5.3\ \text{TeV}^2}{\Lambda_W^2} \quad (\Delta\kappa = 0) \tag{2.9}$$

It should be noted that these unitarity bounds have some model dependence due to the choice of the form factor power n used in the generalized form factor. In the absence of experimental measurement of the form factor behavior of the anomalous couplings, the choice of the generalized form factor power is somewhat arbitrary, as long as the form factor power $n_\kappa > \frac{1}{2}$ and $n_\lambda > 1$, since the anomalous invariant amplitudes grow as $\sqrt{\hat{s}}$ and $\hat{s}$ respectively [6]. A form factor power of $n_\kappa = n_\lambda = n = 2$ was chosen by analogy to the nucleon form factor.

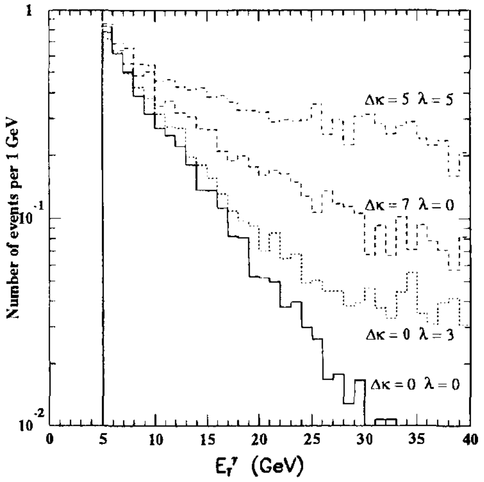

Figure 2.3: E_t of Central γ from $(W \rightarrow \mu\nu_\mu) + \gamma$ for some values of the anomalous couplings

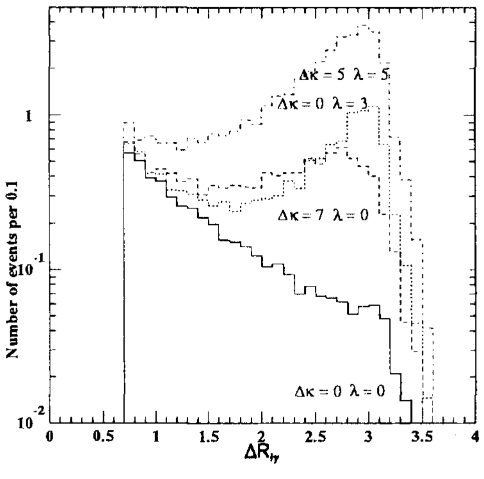

Figure 2.4: ΔR of Central γ from $(W \rightarrow \mu\nu_\mu) + \gamma$ for some values of the anomalous couplings.

If instead of $n = 2$, a form factor power of $n = 1$ had been chosen, the unitarity bounds on $\Delta\kappa$ and λ are more strict by a factor of ~ 4.

Even though none of the diagrams can be neglected because of interference effects, in certain kinematic regions a subset of the diagrams contribute most of the signal. In the initial-state radiation processes (Figures 2.1a & 2.1b) the radiation is sharply peaked in angle along the incident quark/anti-quark directions. The vast majority of photons from the radiative W decay tend to be co-linear with the decay lepton. Both initial and final state radiation are sharply peaked at low energy, as is the radiation from $W\gamma$. However, the photons from $W\gamma$ production are not correlated with the lepton, and are not bounded by the mass of the W boson.

At large angles between the lepton and the photon the **u** and **t** channel diagrams cancel the s channel diagram, resulting in a "gauge zero" in the $W^{\pm}\gamma$ overall amplitude, and hence the $W\gamma$ cross section at $\cos\theta^* = \mp\frac{1}{3}$.[1] Experimentally, this gauge zero will be at least partially filled in by structure function effects, background processes, event mis-reconstruction, as well

---

[1] The angle θ^* is defined as the angle between the photon and the incoming quark in the $W\gamma$ rest frame.

as by non-gauge theory values of κ, λ, $\tilde{\kappa}$ and $\tilde{\lambda}$[1]. Measurement of the depth of the dip in the cross section at $\cos\theta^* = \mp\frac{1}{3}^*$ and the shape of the $cos\theta^*$ distribution provides a sensitive measurement of the values of these parameters. Measurement of the $W\gamma$ cross section also constrains κ and λ, albeit in a less powerful manner.

2.3 $Z\gamma$ Theory

In the case of $Z\gamma$ production, since the Z boson is its own anti-particle, the Z does not have any ***static*** electromagnetic multipole moments like charge, magnetic dipole or electric quadrupole moments. Hence, the SM of electroweak interactions predicts no $ZZ\gamma$ or $Z\gamma\gamma$ tri-linear gauge couplings at the tree-level. The Feynman diagrams for SM $Z\gamma$ production are shown in Figures 2.2a, 2.2b and 2.2e, corresponding to initial state and final state radiation (inner bremsstrahlung). Non-SM Feynman diagrams for anomalous $Z\gamma$ couplings are shown in Figures 2.2c and 2.2d. These two Feynman diagrams are distinct only in the limit of a zero-width Z. Since the Z boson has a non-zero width ($\Gamma_Z = 2.5$ GeV) these two diagrams represent different kinematic regions of the same process. The SM initial and final-state radiation for $Z\gamma$ tends to produce photons sharply peaked in angles about the beam directions and the decay lepton directions, respectively.

Four different anomalous couplings are allowed by electromagnetic gauge invariance and Lorentz invariance. The most general anomalous $Z\gamma Z$ vertex function is given by[9]

$$\Gamma^{\alpha\beta\mu}_{Z\gamma Z}(q_1,\ q_2,\ P) = \tag{2.10}$$

$$\frac{P^2 - q_1^2}{M_Z^2}\left[h_1^Z\left(q_2^\mu g^{\alpha\beta} - q_2^\alpha g^{\mu\beta}\right) +\right.$$

$$\frac{h_2^Z}{M_Z^2} P^\alpha \left(P \cdot q_2 g^{\mu\beta} - q_2^\mu P^\beta\right) + h_3^Z \epsilon^{\mu\alpha\beta\rho} \, q_{2\rho} + \frac{h_4^Z}{M_Z^2} P^\alpha \epsilon^{\mu\beta\rho\sigma} P_\rho q_{2\sigma} \Big]$$

where M_Z is the Z boson mass, P and q_1 are the incoming and outgoing Z boson four-momenta (Lorentz indices μ and α respectively), and q_2 is the four-momentum of the outgoing (on-shell) photon (Lorentz index β). The most general $Z\gamma\gamma$ vertex function can be obtained from the $Z\gamma Z$ vertex function by replacing

$$\frac{P^2 - q_1^2}{M_Z^2} \rightarrow \frac{P^2}{M_Z^2} \quad \text{and} \quad h_i^Z \rightarrow h_i^\gamma, \quad i = 1, \ldots 4$$

The overall $ZZ\gamma$ and $Z\gamma\gamma$ coupling strengths $g_{ZZ\gamma}$ and $g_{Z\gamma\gamma}$ are chosen to be e, where e is the proton charge. The overall factor of $P^2 - q_1^2$ in the $Z\gamma Z$ vertex function is a consequence of Bose symmetry, whereas the factor of P^2 in the $Z\gamma\gamma$ vertex function is a consequence of electromagnetic gauge invariance; note that the $Z\gamma\gamma$ vertex function vanishes identically if both photons are on-shell.

The form factors h_i^Z and h_i^γ are dimensionless functions of q_1^2, q_2^2 and P^2. Similar to the form factors in the $WW\gamma$ vertex function, the values of h_i^Z and h_i^γ at low energies are constrained by S-matrix unitarity[7]. The $Z\gamma$ form factors h_i^V are assumed to be of the generalized dipole form [10]:

$$h_i^V(P^2 = \hat{s}, \; q_1^2 = M_Z^2, \; q_2^2 = 0) \;=\; \frac{h_{i0}^V}{(1 + \hat{s}/\Lambda_Z^2)^n} \tag{2.11}$$

Note that all couplings are $\mathcal{C}$−odd; h_1^V and h_2^V ($V = Z, \; \gamma$) violate $\mathcal{CP}$ (i.e. violate $\mathcal{T}$).

In the static limit ($E_\gamma = k \to 0$), the higher order transition moments of the Z boson are related to the h_{i0}^Z anomalous $ZZ\gamma$ couplings by (with $\hbar = c = 1$)[11]

$$\begin{aligned}
d_{Z_T} &= -\tfrac{e}{M_Z}\tfrac{1}{\sqrt{2}}\tfrac{k^2}{M_Z^2}\left(h_{30}^Z - h_{40}^Z\right) && \text{Electric Dipole Trans. Moment} \\
Q_{Z_T}^m &= \tfrac{e}{M_Z^2}\sqrt{10}\,(2h_{30}^Z) && \text{Magnetic Quadrupole Trans. Moment} \\
\mu_{Z_T} &= -\tfrac{e}{M_Z}\tfrac{1}{\sqrt{2}}\tfrac{k^2}{M_Z^2}\left(h_{10}^Z - h_{20}^Z\right) && \text{Magnetic Dipole Trans. Moment} \\
Q_{Z_T}^e &= \tfrac{e}{M_Z^2}\sqrt{10}\,(2h_{10}^Z) && \text{Electric Quadrupole Trans. Moment}
\end{aligned}$$

Thus the experimental limits on the $ZZ\gamma$ anomalous couplings also place limits on the transition moments of the Z boson. In the Standard Model, at the tree level, all $ZZ\gamma$ couplings as well as all SM transition moments vanish. However, at the one-loop level, only the $\mathcal{CP}-$conserving couplings h_3^V and h_4^V are non-zero. Like the one-loop SM corrections to the κ and λ parameters for $W\gamma$, the higher order SM contributions to $Z\gamma$ are also expected to be quite small, e.g. $h_3^Z \sim 2 \times 10^{-4}$[12].

2.4 Unitarity Constraints for $Z\gamma$

Partial wave unitarity places restrictions on the reduced amplitudes, $A_{\lambda_Z\lambda_\gamma}^Z$ for arbitrary values of h_{i0}^Z ($i = 1 - 4$) for anomalous $ZZ\gamma$ couplings [13, 10]:

$$\sum_{\lambda_Z\lambda_\gamma} \left|A_{\lambda_Z\lambda_\gamma}^Z\right|^2 < \frac{24\sin^2\theta_W\ \cos^2\theta_W}{5\ \alpha^2(\hat{s})\left(1 - \frac{M_Z^2}{\hat{s}}\right)^3} \tag{2.12}$$

where λ_Z, λ_γ are the final-state Z boson and photon helicities, respectively. For the assumed generalized dipole form factor and form factor powers ($n = 3$ for h_{30}^Z and $n = 4$ for h_{40}^Z), unitarity is violated for anomalous h_{30}^Z and h_{40}^Z $ZZ\gamma$ couplings if

$$\frac{(\frac{\hat{s}}{M_Z^2}-1)^3}{(1+\frac{\hat{s}}{\Lambda_Z^2})^6}\left[\left(h_{30}^Z-\frac{1}{2}h_{40}^Z\frac{(\frac{\hat{s}}{M_Z^2}-1)}{(1+\frac{\hat{s}}{\Lambda_Z^2})}\right)^2+(h_{30}^Z)^2\frac{M_Z^2}{\hat{s}}\right]\geq\frac{48\sin^2\theta_W\;\cos^2\theta_W}{5\alpha^2(\hat{s})} \tag{2.13}$$

over the $\sqrt{\hat{s}}$ range $M_Z < \sqrt{\hat{s}} < 1.8$ TeV. A similar unitarity relation holds for anomalous h_{10}^Z and h_{20}^Z $ZZ\gamma$ couplings, replacing $h_{30}^Z \rightarrow h_{10}^Z$ and $h_{40}^Z \rightarrow h_{20}^Z$ [13, 10].

Partial wave unitarity also places restrictions on the reduced amplitudes for arbitrary values of h_{i0}^γ $(i = 1-4)$ for anomalous $Z\gamma\gamma$ couplings [13, 10]:

$$\sum_{\lambda_Z\lambda_\gamma}\left|A^\gamma_{\lambda_Z\lambda_\gamma}\right|^2<\frac{3\,(3-6\sin^2\theta_W+8\sin^4\theta_W)}{5\;\alpha^2(\hat{s})\left(1-\frac{M_Z^2}{\hat{s}}\right)^3} \tag{2.14}$$

where λ_Z, λ_γ are the final-state Z boson and photon helicities, respectively. For the assumed form factor, unitarity is violated for anomalous h_{30}^γ and h_{40}^γ $Z\gamma\gamma$ couplings if

$$\begin{aligned}\frac{(\frac{\hat{s}}{M_Z^2}-1)^3}{(1+\frac{\hat{s}}{\Lambda_Z^2})^6}\quad&\left[\left(h_{30}^\gamma-\frac{1}{2}h_{40}^\gamma\frac{(\frac{\hat{s}}{M_Z^2}-1)}{(1+\frac{\hat{s}}{\Lambda_Z^2})}\right)^2+(h_{30}^\gamma)^2\frac{M_Z^2}{\hat{s}}\right]\\&\geq\frac{6\,(3-6\sin^2\theta_W+8\sin^4\theta_W)}{5\alpha^2(\hat{s})}\end{aligned} \tag{2.15}$$

over the $\sqrt{\hat{s}}$ range $M_Z < \sqrt{\hat{s}} < 1.8$ TeV. A similar unitarity relation holds for h_{10}^γ and h_{20}^γ $Z\gamma\gamma$ couplings, replacing $h_{30}^\gamma \rightarrow h_{10}^\gamma$ and $h_{40}^\gamma \rightarrow h_{20}^\gamma$ [13, 10].

If only one anomalous $ZZ\gamma$ coupling is assumed to be non-zero at a time and $\Lambda_Z >> M_Z$, then for the assumed form factor, the unitarity limits are:

$$|h_{10}^Z|,\ |h_{30}^Z|\ <\ \frac{1.00\ \text{TeV}^3}{\Lambda_Z^3}\qquad(h_{20}^Z=h_{40}^Z=0,\quad n=3) \tag{2.16}$$

$$|h_{20}^{Z}|,\ |h_{40}^{Z}| \ < \ \frac{0.030\ \mathrm{TeV}^5}{\Lambda_Z^5} \qquad (h_{10}^{Z} = h_{30}^{Z} = 0, \quad n = 4) \tag{2.17}$$

For anomalous $Z\gamma\gamma$ couplings, the unitarity limits are:

$$|h_{10}^{\gamma}|,\ |h_{30}^{\gamma}| \ < \ \frac{1.20\ \mathrm{TeV}^3}{\Lambda_Z^3} \qquad (h_{20}^{\gamma} = h_{40}^{\gamma} = 0, \quad n = 3) \tag{2.18}$$

$$|h_{20}^{\gamma}|,\ |h_{40}^{\gamma}| \ < \ \frac{0.036\ \mathrm{TeV}^5}{\Lambda_Z^5} \qquad (h_{10}^{\gamma} = h_{30}^{\gamma} = 0, \quad n = 4) \tag{2.19}$$

As in the case of $W\gamma$, the $Z\gamma$ unitarity bounds and the sensitivity of the experimental limits to the choice of Λ_Z have some model-dependence associated with the choice of the form factor power(s) used in the generalized form factor. The choice of form factor power is arbitrary as long as $n > \frac{3}{2}$ for $h_{10,30}^{V}$ and $n > \frac{5}{2}$ for $h_{20,40}^{V}$ [7]. These lower limits on the form factor power are a consequence of the high-energy behavior of the anomalous part of the amplitudes, which grow as $(\sqrt{\hat{s}}/m_Z)^3$ for $h_{1,3}^{V}$ and $(\sqrt{\hat{s}}/m_Z)^5$ for $h_{2,4}^{V}$. Our choice of $n = 3$ for $h_{1,3}^{V}$ and $n = 4$ for $h_{2,4}^{V}$ was motivated mainly by the requirement that unitarity be preserved at high energies ($\sqrt{\hat{s}} >> \Lambda_Z >> M_Z$) and that terms proportional to $h_{20,40}^{V}$ have the same high-energy behavior as those proportional to $h_{10,30}^{V}$. For a different choice of form factor powers, e.g. $n = 2$ for $h_{1,3}^{V}$ ($n = 3$ for $h_{2,4}^{V}$), the unitarity bounds on the $h_{10,30}^{V}$ ($h_{20,40}^{V}$) anomalous couplings are made more stringent by factors of ~ 2.6 (~ 2.9), respectively. For these choices of form factor powers, sensitivity to Λ_Z is reduced by factors of ~ 1.4 (~ 1.2) respectively. These effects are partially offset by an increase in the the predicted rate of $Z\gamma$ production for the choice of form factor powers of $n = 2$ for $h_{1,3}^{V}$ ($n = 3$ for $h_{2,4}^{V}$) *vs.* the choice of $n = 3$ for $h_{1,3}^{V}$ ($n = 4$ for $h_{2,4}^{V}$).

As mentioned previously, non-standard $WW\gamma$, $ZZ\gamma$ and $Z\gamma\gamma$ couplings are momentum dependent form factors which must vanish at large momentum transfer to guarantee that S-

matrix unitarity is not violated[14]. Sensitivity limits for the anomalous couplings found from experimental data will thus depend on the the form factor scale Λ which characterizes the energy above which the form factor starts to decrease. Λ is generally assumed to be connected to some novel interactions operative at energies $\approx \Lambda$, and is expected to be at least of order of a few hundred GeV. For $\bar{p}p$ interactions at 1.8 TeV, the dependence of the sensitivity limits on the scale Λ is rather mild for the $WW\gamma$ couplings, but it is much stronger for $ZZ\gamma$ and $Z\gamma\gamma$ couplings.

2.5 Effects of Destructive Interference

Destructive interference between the diagram involving the $WW\gamma$ vertex and the **u** and **t** channel graphs for the SM $W\gamma$ process results in a radiation amplitude zero. This destructive interference is not present for the SM $Z\gamma$ process. The ratio of experimentally observed $W\gamma/Z\gamma$ cross section × branching ratios is expected to be ~ 4, in contrast to the ratio of the inclusive W/Z cross section × branching ratios of ~ 11. For non-SM values of κ and λ, etc. or the h_i^V parameters, the $W\gamma$ and $Z\gamma$ cross sections vary quadratically with these parameters. Due to interference effects and the different $\hat{s}-$dependencies of the various anomalous terms in the overall invariant amplitude, the minimum of the $W\gamma$ cross section does not occur for the SM values of κ and λ; for similar reasons, the minimum of the $Z\gamma$ cross section does not occur at the SM values of the h_{io}^Z (h_{io}^γ) parameters.

Chapter 3

Experimental Apparatus

The Tevatron $p\bar{p}$ collider at Fermilab operates at a center of mass energy of 1.8 TeV and a luminosity[1] 10^{30} $\mathrm{cm}^{-2}\mathrm{sec}^{-1}$. The CDF[15] detector at the Tevatron is a multi-component, 5000-ton detector that covers most of 4π solid angle. A perspective view of the CDF detector with coordinate axes indicated is shown in Figure 3.2, and a cut away view is shown in Figure 3.1.

3.1 The Detector

The CDF coordinate system is defined with the z axis in the direction of the proton beam, the y axis vertical, and the x axis pointing radially outward from the center of the Tevatron ring. Spherical coordinates are used, and refer to the z axis as $\theta = 0$ and the x axis as $\phi = 0$. A useful coordinate frequently used in high-energy physics is the approximately Lorentz-invariant coordinate, pseudo-rapidity, $\eta = -log(tan\frac{\theta}{2})$.

---

[1] Luminosity, $\mathcal{L}$, is defined to be the product of incident beam flux with mean target density. A process with a cross section σ, has a rate given by $\sigma \cdot \mathcal{L}$. In particular, if σ describes a production process, like $q\bar{q} \rightarrow Z^0 \rightarrow e^+e^-$, $\sigma \cdot \mathcal{L}$ gives the event rate, and integrating $\sigma \cdot \mathcal{L}$ over time gives the total number of events observed.

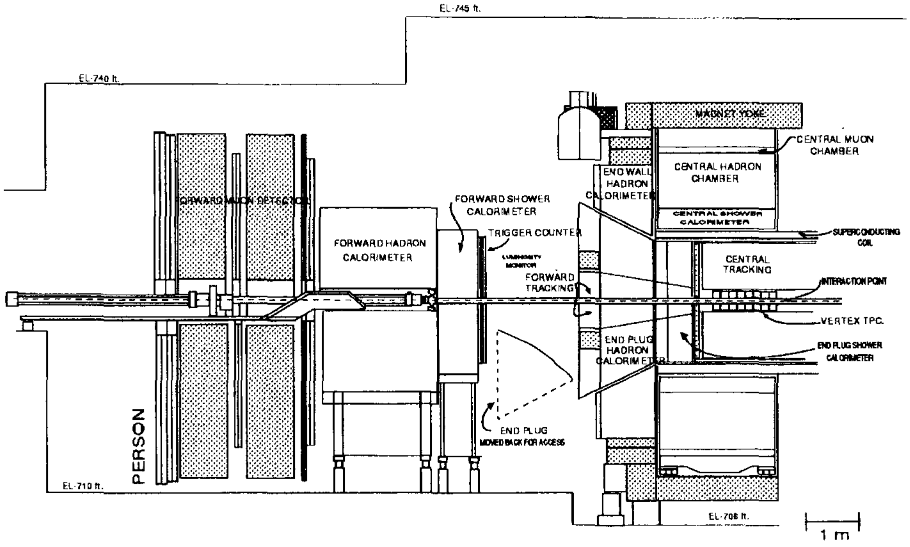

Figure 3.1: A cutaway view showing the main systems of the CDF detector. The detector is symmetric about the $\eta = 0$ plane.

The CDF detector includes three tracking detectors, six calorimeter subsystems, and two muon detection systems. The tracking systems are all enclosed in a 1.4116 T axial magnetic field generated by a 5 m long by 3 m diameter superconducting solenoid. The curvature of the charged particles within the solenoid uniquely determines the charged particle momentum.

Outside of this solenoid are layers of hermetic calorimeters arranged in projective towers that are aligned to the nominal interaction region. The calorimeters have uniform granularity in η and ϕ, and extend to within 2° of the beamline. All of these systems are interleaved to cover most of the 4π steradians of solid angle.

3.2 Beam-Beam Counters

Immediately outside of the forward and backward calorimeters are the Beam Beam Counters (BBC), a plane of scintillation counters located at $z = \pm$ 5.8 m from the nominal interaction

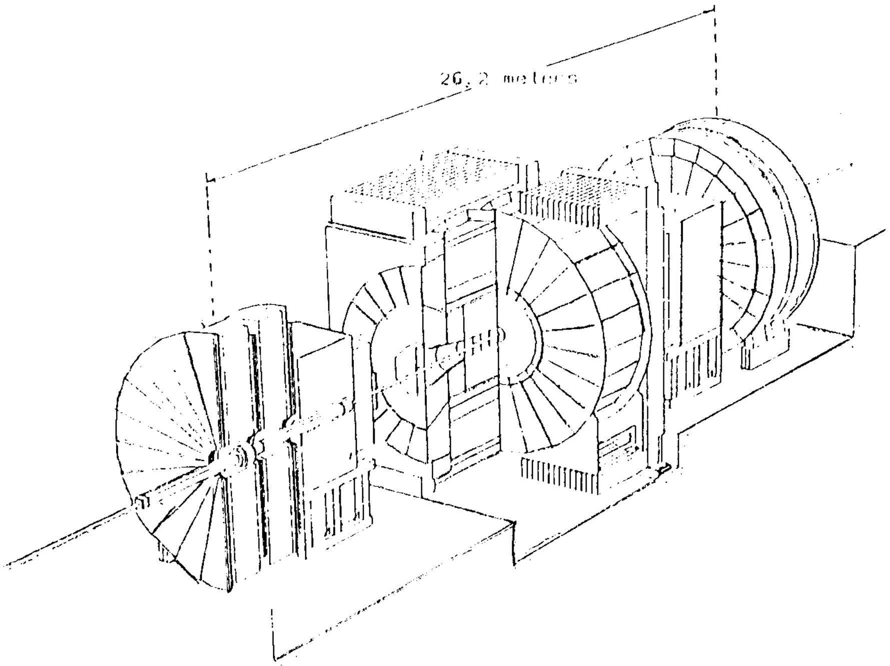

Figure 3.2: A perspective view of the CDF detector, showing the 15° segmentation of the central wedge.

point. The BBC covers the beam-fragmentation region in the pseudo-rapidity range $3.2 < |\eta| < 5.9$. The BBC is used in the minimum bias, or Level 0 trigger, which requires that at least one counter in each plane of the BBC fire within a time window of 15 ns centered around the beam crossing time. It is also used as the primary luminosity monitor for CDF.

3.3 Tracking Systems

The CDF central tracking system is composed of a time projection chamber located near the vertex (the VTPC), a large volume central tracking chamber (the CTC) contained within the 1.4116 Tesla magnetic field.

The innermost tracking detector is the Vertex Time Projection Chambers (VTPC), consisting of eight modules placed end-to-end for a total length of 2.8 m along the beamline [16]. The VTPC is designed to measure charged tracks in the r-z plane down to $|\eta| \simeq 3.5$ ($\theta = 3.5°$)

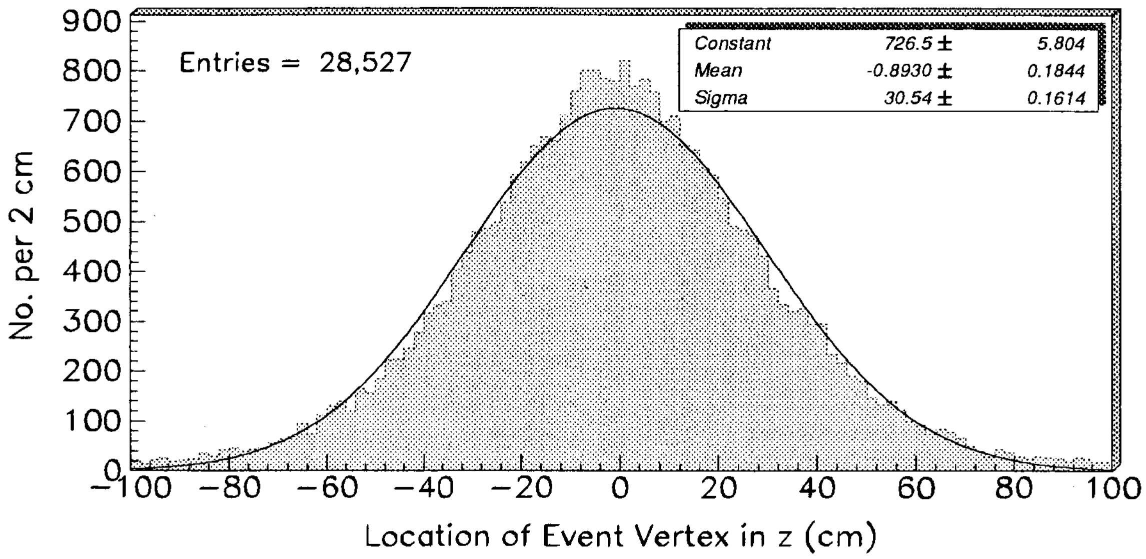

Figure 3.3: The Z distance (cm) of the event vertex from the origin of the CDF coordinate system.

and because alternating chambers are rotated 11.3° in ϕ, the VTPC provides $r - \phi$ stereo information as well. VTPC track segments were used to determine the event vertices to within $\sigma_Z = 1$ mm rms.

The location of the $p\bar{p}$ interaction region was well maintained by the accelerator operators during the collider run to occur near the origin of the CDF detector (Figure 3.3). The gaussian spread of the event vertex's location along the z axis is due to the length and shape of the beam bunches, and is not due to any detector limitations.

The Central Tracking Chamber (CTC) is a 3.2 m long cylindrical drift chamber extending radially 0.3 m to 1.3 m from the beam line, and is used to measure charged tracks in 3 dimensions down to $|\eta| < 1.0$ [17]. The effective rms momentum resolution of the the CTC is approximately $\frac{\delta P_T}{P_T} = 0.0020 P_T$ (P_T in GeV/c) for isolated tracks, with an effective coverage of $40° \leq \theta \leq 140°$. Tracks beyond this range suffer from degraded resolution and loss of track finding efficiency. Since the transverse position of the beam is known to $\sigma_{x,y} \simeq 20 \mu m$ on a run-to-run basis,

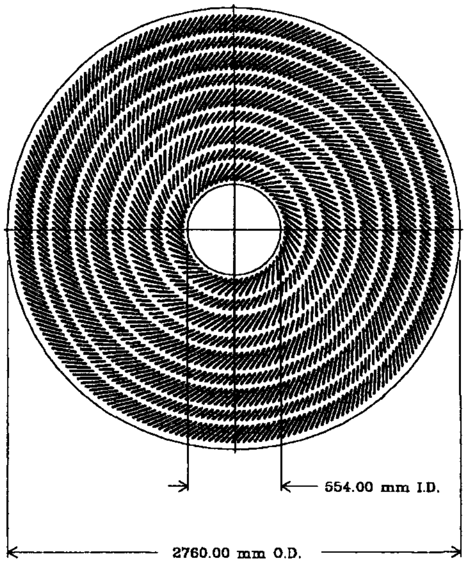

Figure 3.4: An end view of the CTC chamber, showing wire placement into 'superlayers' and the 45° cell-tilt to compensate for the Lorentz angle of the ionization drift.

imposing the constraint that the track originates from the event vertex results in an improved momentum resolution of $\frac{\delta P_T}{P_T} = 0.0011 P_T$.

3.4 Calorimeter Systems

The CDF calorimeter system were designed with projective tower structure to combine fine granularity with good energy resolution. The towers are oriented to align with the nominal interaction region and consist of multiple layers of absorbing material interleaved with a readout mechanism.

The central calorimeters cover the region $|\eta| \leq 1.1$ with a granularity of $\Delta\phi = 5°$ by $\Delta\eta = 0.1$. Each tower consists of two systems, a Central Electromagnetic (CEM) [18] and a Central Hadronic (CHA) [19] system. Each slice of 15° in ϕ is called a wedge, and consists of the inner most detector, the CEM, then the CHA.

The CEM is approximately 18 radiation lengths thick, and uses 31 layers of polystyrene scintillator interleaved with 30 layers of lead. A wavelength shifting material coupled to acrylic lightguides transports the light to photomultiplier tubes. The CEM calibration was maintained during the run to approximately 0.5% using cesium sources and a xenon flash. The CEM has an energy resolution of $\delta E/E = 13.5\%/\sqrt{E_T} \oplus 2\%$ (E in GeV). The CEM is used in muon identification by detection of their minimum ionizing energy deposition in the calorimeter, and identifies photons by a trackless EM cluster in the calorimeter.

The Central Hadronic calorimeter (CHA) is 4.5 absorption lengths thick, and is similar to the CEM in construction and geometry, except that the CHA uses iron instead of lead as the absorptive material, and does not use wave-shifters on the light output path. The CHA is calibrated in a test stand using beams of known-energy pions, and has a energy resolution of $\delta E/E = 75\%/\sqrt{E} \oplus 3\%$ for isolated pions.

3.5 Central Electromagnetic Strip Chambers

The Central Electromagnetic Strip chambers (CES) consists of a multiwire proportional chamber embedded inside each wedge of the central EM calorimeter, located at a radius of 184.15 cm from the beam. The CES can be used to determine shower position and transverse development of an electromagnetic shower near shower maximum (about 6 radiation lengths) by measurement of the charge deposition on orthogonal strips and wires. The CES anode wires measure ϕ and the cathode strips measure η. Figure 3.6 shows the orientation of the cathode strips and anode wires in the CES. In this analysis the CES information is used to separate single photons from the multiple photon background, as well as provide a precise Z and ϕ position of the EM

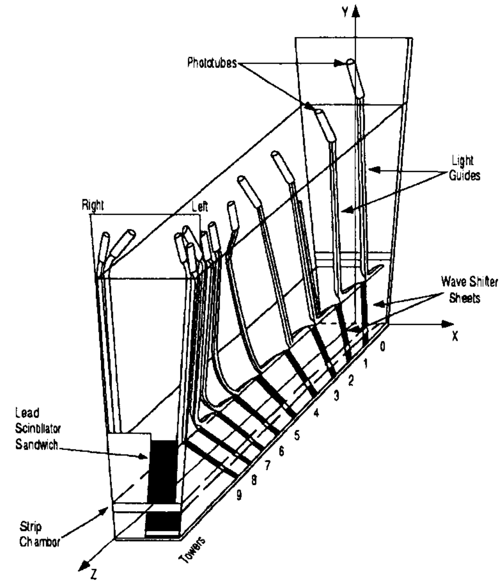

Figure 3.5: A view of a central calorimeter wedge, showing the locations of the pads and strips, as well as the projective tower structure.

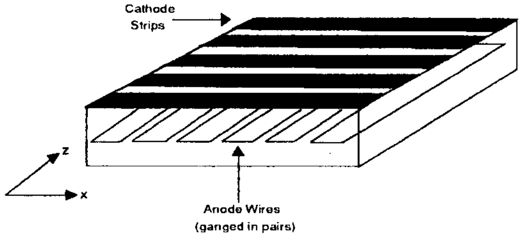

Figure 3.6: Orientation of the Strips and Wires in the CES.

calorimeter cluster. The r-z position measurement is determined to an rms accuracy of 3.0 cm, and 1.7 cm in $r - \phi$.

3.6 Muon Chambers

The Central Muon Chambers (CMU) are the outermost part of the central detector apparatus, located behind approximately 5 hadronic absorption lengths of central calorimeter at a distance of 3470 mm from the interaction region [20]. These drift chambers consist of a four-by-four array of drift cells operated in limited-streamer mode. A diagram of the chambers is shown in Figure 3.7. Two of the four layers of cells are offset in order to resolve the left-right ambiguity remaining when drift times were used to measure the track position. Figure 3.7 show the position of the CMU chambers within a wedge.

In order to reduce the total number of electronic channels to be read out, the sense wires of alternate layers are 'ganged' at $\theta = 90^\circ$, and the wires are read out only on the outer sides of the wedges. The CMU uses drift time, charge-division and the offset geometry of the CMU chamber stack to provide 3 dimensional reconstruction of the muon tracks traversing the chambers. The resulting muon "stubs" are then combined with CTC tracks to fully reconstruct the muons passing through the detector.

Three muon chambers are located side-by-side per calorimeter wedge, and, discounting small cracks, cover 12.6° of the 15° spanned by the wedge, leaving a 2.4° gap between adjacent wedges. The CMU chambers extend to $|\eta| < 0.63$, with a 3° gap in coverage around the $\theta = 90^\circ$ crack that divides the positive and negative η wedges.

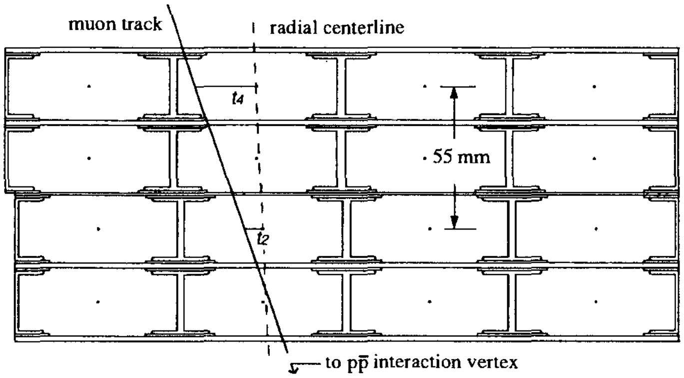

Figure 3.7: An endview of a CMU chamber, showing the 4x4 array that makes up a single chamber, three of which are in a wedge.

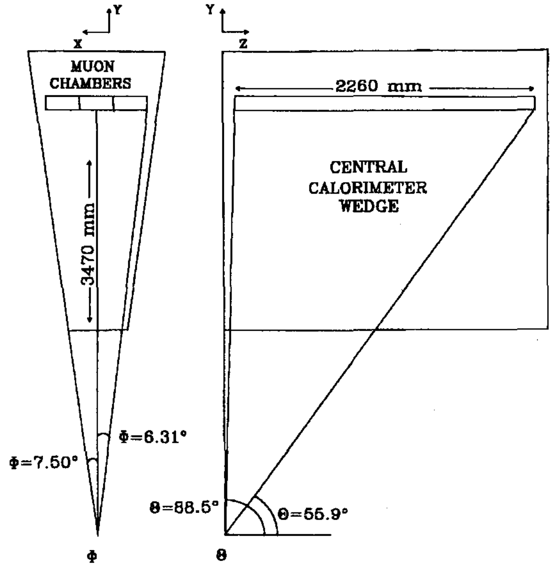

Figure 3.8: Central Muon chambers with respect to a calorimeter wedge.

Chapter 4

Event Selection

The starting point for the $W\gamma$ and $Z\gamma$ analysis in the muon channels is the inclusive muon W and Z data samples used for the inclusive muon W and Z absolute cross section × branching ratio measurements [21] and the muon W/Z cross section ratios [5]. This data set was used because it is well understood, and many of the efficiencies, acceptances, and systematics have been previously determined.

4.1 The Muon Trigger

In the 1988-89 Tevatron collider run, CDF collected $\int \mathcal{L}_\mu \mathrm{dt} = 3.54 \pm 0.24$ pb^{-1} of high P_T muon data[22]. The uncertainty in the integrated luminosity is 6.8%, due primarily to the uncertainty associated with that part of the total inelastic $\bar{\text{p}}$-p cross section observed by the Beam-Beam Counters (BBC), $\sigma_{BBC} = 46.8 \pm 3.2\ mb$.

The interaction rate at the CDF detector during the 1988-89 Tevatron collider run was about five orders of magnitude higher than the data acquisition system could record. To select the interesting events from this large rate, a four level trigger system was used[23], each level using progressively stricter event selection requirements. Trigger Levels 0 through 2 use programmable fast electronic modules, using as input prompt signals from the detector. Trigger Level 3 is based on a set of computers running filter algorithms on the full data stream read out from the detector.

The lowest trigger is the Level 0 trigger, which requires that the BBC counters on both ends of the detector have a coincident signal. The BBC signal must be between 13.5 ns and 27.5 ns after the expected $\bar{p}$-p interaction time[24]. This trigger is also referred to as the Minimum Bias trigger, and data taken with only this level of processing was used later in this analysis.

The Level 1 trigger selects for a variety of interesting event signatures, any one of which is sufficient to keep the event for further processing. The Level 1 trigger of interest to this analysis is the Level 1 central muon high P_T trigger[25], which uses the time difference of the signal from alternating layers of the CMU tower. This time difference can be related to the angle the muon traversed the CMU, thus the time difference can be used to measure muon P_T,

$$P_T^{\mu} = \frac{154}{\Delta t} \text{ GeV/c}$$

where Δt is in ns. Two triggering thresholds were used, $P_T \geq 3$ GeV/c and $P_T \geq 5$ GeV/c. Multiple scattering of the muon smears this relationship; however, since the data used in this analysis requires $P_T^{\mu} > 20$ GeV/c the smearing does not affect the trigger efficiency for this data set.

The Central Fast Tracker[26] (CFT) is a hardware tracking processor which uses prompt timing information from the 4392 axial sense wires of the CTC to find two-dimensional tracks. The CFT uses a list of pre-calculated hit patterns to quickly sort tracks into 8 P_T bins over the range 2.5 GeV/c to 15 GeV/c, with a momentum resolution of $\frac{\delta P_T}{P_T^2} = 3.5\%$. The CFT trigger threshold for the inclusive muon data set was 9 GeV/c. At and above this threshold, the CFT is 98% efficient.

The Level 2 muon trigger used in this analysis requires a CFT track with $P_T \geq 9$ GeV/c in the central tracking chamber to match to the Level 1 muon tower to within 15 degrees in ϕ. A lookup table was used to search the list of the CFT tracks for matches to a muon tower. If a match was found, further processing was done to match the CFT track to the hits in the CMU system.

The Level 3 trigger is simply a streamlined version of the full event reconstruction. More complete CTC tracking is done, and a match of better than 10 cm is required between the extrapolated 2-dimensional CTC track and the muon stub, unless the wire ambiguity in the CMU could not be resolved by charge division, in which case the extrapolated track was required to match to either of the wires to within 10 cm.

4.2 Muon Event Selection

The muon W and Z samples were obtained from a common central muon sample by requiring at least one "Gold Muon". A Gold Muon has the following properties:

- The event vertex be within $|Z_{\mathrm{vertex}}| < 60.0\ cm$ of nominal $Z = 0.0$.
- A reconstructed central muon with a $P_T \geq 20\ GeV/c$, and in a good fiducial region of the central muon system.
- A match of the extrapolated CTC track to the reconstructed muon "stub" in the muon chambers to better than 2 cm in the $r - \phi$ plane.

- There must be less than 6 GeV of energy deposited in the hadronic calorimeter, and less than 2 GeV of electromagnetic energy deposited in the calorimeter in the calorimeter towers traversed by the muon. Note that the energy deposited in the hadronic calorimeter is in fact EM energy due to ionization along the muon path, and is not due to hadronic interactions of the muon.

- Isolation $I \equiv (\Sigma_{0.4}E_T - E_T^\mu)/P_T^\mu \leq 0.10$, where E_T^μ is the transverse energy deposited in the calorimeter towers traversed by the muon. P_T^μ is the transverse momentum of the muon track, and $\Sigma_{0.4}E_T$ is the sum of the transverse calorimeter energy in a cone of $\Delta R = \sqrt{\Delta\eta^2 + \Delta\phi^2} = 0.4$ centered on the muon track.

- Cosmic rays were removed from the sample by using the central tracking chamber information to veto those events that were inconsistent with tracks coming from the event vertex.[27]

A total of 2011 events pass these requirements.

Muon W candidates were obtained from the common central muon sample by additionally requiring $\not{E}_T > 20\ GeV$. The W candidates must not be simultaneously consistent with being an muon Z candidate, as defined below. A total of 1436 events pass the muon W requirements.

Muon Z candidates were obtained from the common central muon sample by additionally requiring a second "Silver Muon", defined as a minimum ionizing track passing the following selection criteria:

- There must be less than 6 GeV of energy in the hadronic calorimeter tower and less than 2 GeV of energy in the EM calorimeter in the muon tower.

- $|\eta| < 1.0$

- $P_T \geq 20\ GeV/c$
- Opposite charge sign to the first muon.
- The invariant mass of the dimuon pair lies between $65 < M_{\mu\mu} < 115\ GeV/c^2$.

A total of 106 events pass the muon Z requirements.

4.3 Photon Selection

A common photon selection was imposed on the inclusive muon sample to form the $(W \rightarrow \mu\nu_\mu) + \gamma$ and $(Z \rightarrow \mu^+\mu^-) + \gamma$ sub-datasets. Photon candidates were selected from electro-magnetic energy clusters found in the central calorimeter. The algorithm used to form electro-magnetic energy clusters uses several parameters to control the formation of electro-magnetic energy clusters, among these are the "seed" energy, and the "sum" energy. The seed energy is the minimum energy in a tower needed to initiate an attempt to form a cluster. The sum parameter is the minimum transverse-energy sum over all the towers of the cluster for the cluster candidate to be kept. The details of the formation of the EM cluster are listed in Appendix A.

The CDF default electro-magnetic clustering algorithm uses a seed calorimeter tower threshold of $E_T > 3.0$ GeV, and a sum E_T threshold of 5 GeV. The clustering algorithm is inefficient at the 5 GeV threshold because the energies used in the list of seed and over-threshold towers are not corrected for position dependent energy response within each tower and tower to tower energy scale variations. Figure 4.1 shows that the default clustering becomes fully efficient at about 6 GeV E_T for the central region of the calorimeter. This effect has been studied using Monte Carlo (MC) generated photons generated with a flat energy spectrum from $0.5 < E_T < 15\ GeV$ in the central calorimeters.

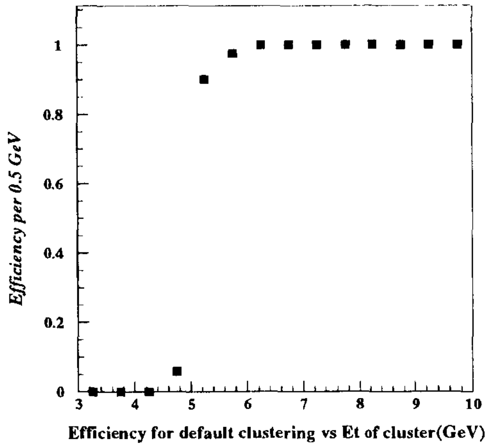

Figure 4.1: EM cluster formation efficiency, for the default clustering parameters (seed = 3.0 GeV and sum = 5.0 GeV)

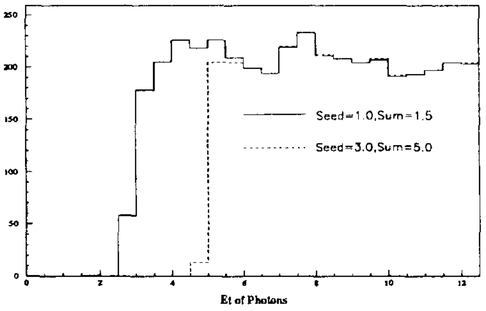

Figure 4.2: EM clusters found from QFL simulated photons

All data sets (inclusive muon, Jet-20, and all Monte Carlo data sets) were reclustered using a seed tower of 1.0 GeV and a sum E_T of 1.5 GeV. The E_T of the cluster is then adjusted for the position dependent response, and the energy scale corrections. Only those EM clusters with $E_T > 5$ GeV are used in the analysis. Figure 4.2 shows that with these values of the clustering parameters the re-clustered EM objects are fully efficient at the threshold.

4.3.0.1 Fiducial Region

The ϕ region between adjacent calorimeter wedges are not instrumented, and near the ϕ wedge boundries the calorimeter resolution is degraded Therefor the photon candidates were required to be in a fiducial region of the calorimeter. The fiducial region in the central calorimeter is defined by:

- The Z position of the cluster as determined from the shower position in the CES must be $|Z_{cluster}| > 9$ cm in order to stay away from the edge of the 90 degree crack in the central calorimeter.

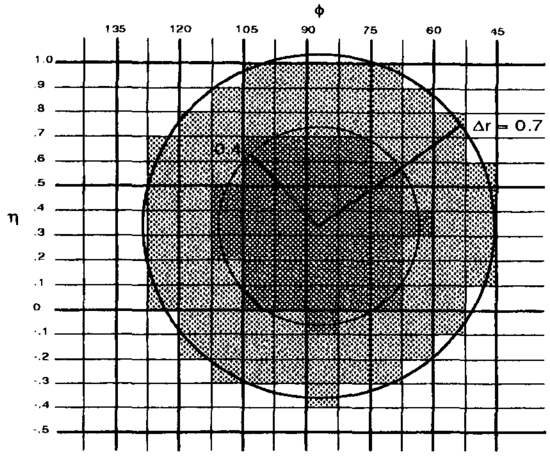

Figure 4.3: Schematic of a typical calorimeter isolation "cone" of $\Delta R = 0.4$ and $\Delta R = 0.7$ in the central calorimeter.

- The cluster must be within ±21 cm of the center of the ±24.24 cm wide wedge, in the $r - \phi$ view.
- Calorimeter tower 9 and tower 7 of the chimney module are non-fiducial regions.

4.3.0.2 Calorimeter Isolation

The photon candidate is required to be isolated in the calorimeter. The E_T deposited in the calorimeter in a cone of $\Delta R = 0.4$ centered around the EM cluster (ET4) is required to be less than $E_T < 2.0$ GeV/c. Each tower the calorimeter is included in the sum if the distance from the centroid of the EM cluster to the weighted centroid of the tower is less than 0.4. Figure 4.3 shows a typical map of the towers included in calorimeter isolation cones of $\Delta R = 0.4$ and $\Delta R = 0.7$.

4.3.0.3 Track Isolation

In order to reduce the background due to soft jets that fragment to a π^0 and soft charged tracks, the sum P_T of all 3 dimensional tracks in a cone of $\Delta R = 0.4$ (PT4) must be less than 2

GeV/c. The opening angle is measured at the primary event vertex. Tracks that have a vertex $|Z_{vtx} - Z_0| > 10\ cm$ from the primary event vertex are not included in this sum.

4.3.0.4 N3D

In order to remove electrons from this photon sample, a requirement was made that no charged particles impact the EM cluster (N3D=0 cut). Each track formed from CTC and VTPC information that has 3-dimensional information is traced out to the EM calorimeter. If the track passes through any of the towers in the EM cluster, the cluster is rejected. Tracks originating from every event vertex are included, not just those tracks from the primary event vertex.

4.3.0.5 Had/EM

The hadronic energy fraction (Had/EM) of the photon candidate must be less than $0.055 + 0.00045E$ where E is the total energy of the cluster. This sliding cut takes into account leakage of energy from the EM calorimeter into the hadronic calorimeter that is directly behind it, in order to maintain a constant efficiency for this cut, independent of the energy of the cluster.

4.3.0.6 Lateral Shower Profile

The lateral shower profile (LSHR) of the EM cluster in the CEM is defined as

$$\mathrm{LSHR} = 0.14 \times \Sigma \frac{E_i^{Adj} - E_i^{Prob}}{\sqrt{0.14^2 \times E + (\Delta E_i^{Prob})^2}}$$

where E_i^{Adj} is the measured energy in the tower adjacent to the seed tower; E_i^{Prob} is the expected energy in that tower calculated from the seed energy of the cluster, the impact position calculated from the CES chambers, and the event vertex, using a shower profile parameterization obtained from test beam data; E is the EM energy of the cluster; and ΔE_i^{Prob} is the error in E_i^{Prob} associated with a 1 cm error in the impact position measurement[28, Section 4.2]. For our photon selection, LSHR < 0.5.

4.3.0.7 CES χ^2_{strip} and χ^2_{wire}

The CES is used to determine if the primary shower profile is consistent with a single EM particle. Overlapping photons from, for instance, a high E_T $\pi^0 \rightarrow \gamma\gamma$ can decay in such a way that the photon showers overlap the calorimeter, thus merging the shower shapes into something that looks like a single EM particle shower. The shape of the CES shower is fitted to the shower profile found from a testbeam setup where electrons were directed into a section of the CES. The shower profile asymmetry and width dependence on the Z impact position, as well as the energy dependence of the CES response are taken into account in the fit. A cut on the chi-square of the fit in both the strip and wire views of less than 20 was made.

4.3.0.8 CES 2^{nd} Cluster

The CES is used to identify EM clusters that are not consistent with single particle showers. The strip and wire views of the CES are searched for clusters with $E_{CES} > 1$ GeV. If a second cluster with E_{CES} above this threshold is found in either the strip or wire chambers, the photon candidate fails the selection.

4.3.0.9 $\Delta R_{\mu\gamma}$ Separation

The bremsstrahlung radiation from the leptons in $W\gamma$ and $Z\gamma$ is sharply peaked at low opening angle with respect to the leptons, see Figure 2.4. To suppress the bremsstrahlung radiation

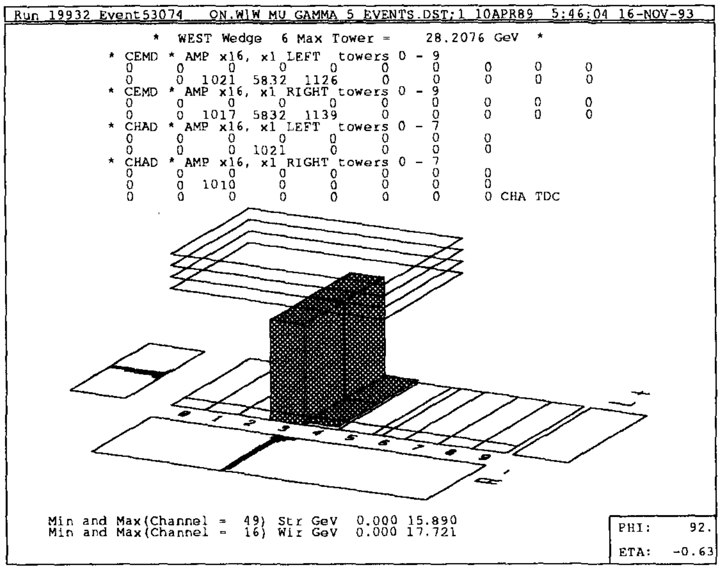

```
Run 19932 Event53074    ON.W1W MU GAMMA 5 EVENTS.DST;1 10APR89   5:46:04 16-NOV-93
                *  WEST Wedge  6 Max Tower =    28.2076 GeV  *
          * CEMD * AMP x16, x1 LEFT  towers 0 - 9
            0     0     0     0     0     0     0     0     0     0
            0     0  1021  5832  1126     0     0     0     0     0
          * CEMD * AMP x16, x1 RIGHT towers 0 - 9
            0     0     0     0     0     0     0     0     0     0
            0     0  1017  5832  1139     0     0     0     0     0
          * CHAD * AMP x16, x1 LEFT  towers 0 - 7
            0     0     0     0     0     0     0     0
            0     0     0  1021     0     0     0     0
          * CHAD * AMP x16, x1 RIGHT towers 0 - 7
            0     0     0     0     0     0     0     0
            0     0  1010     0     0     0     0     0
            0     0     0     0     0     0     0     0 CHA TDC

      Min and Max(Channel =  49) Str GeV  0.000 15.890
      Min and Max(Channel =  16) Wir GeV  0.000 17.721
                                                          PHI:     92.
                                                          ETA:   -0.63
```

Figure 4.4: An example of a typical photon shower in the CES

from the muon, the photon candidates were required to be $\Delta R_{\mu\gamma} = \sqrt{\Delta\eta_{\mu\gamma}^2 + \Delta\phi_{\mu\gamma}^2} > 0.7$ from the muon or muons in the event.

4.3.0.10 Removal of Mis-reconstructed Z's

Finally each of the W candidate events was filtered to remove those events that had a 2^{nd} high P_T track that was consistent with the event being a Z where one of the muons was not reconstructed, resulting in the event being falsely identified as a W event. Section 6.2.1 discusses this background and the cuts used to remove it in greater detail.

4.4 $W\gamma$ and $Z\gamma$ Events Found in the Inclusive Muon Sample

A total of 5 $W\gamma$ and 2 $Z\gamma$ events pass the photon selection cuts. The number of events in the inclusive muon W and Z samples that pass each of the selection requirements is tabulated in Table 4.4. This table also lists the effects of these photon selection cuts on the QCD jet background data sample (See Section 6). Two kinematic quantities often used in $W\gamma$ analysis

	$W_\mu\gamma$	$Z_\mu\gamma$	Jet-20^{QCD}_{bkg}
Inclusive W/Z or Jet-20 Data Samples	1436	106	11726
Pass FidCEM, $E_T^\gamma > 5.0$ GeV, $\Delta R_{\ell\gamma} > 0.7$ Cuts	54	7	266
Pass $ET4 < 2.0$ GeV Cut	18	3	107
Pass $PT4 < 2.0$ GeV Cut	14	2	64
Pass $N3D = 0$ Cut	13	2	57
Pass Had/EM Cut	13	2	55
Pass $L_{shr} < 0.5$ Cut	10	2	42
Pass $\chi^2_{strip} + \chi^2_{wire}$ Cut	8	2	32
Pass no 2^{nd} $CES > 1$ GeV Cut	7	2	20
Pass no 2^{nd} Isolated Track Cut ($W\gamma$ only)	5	–	–

Table 4.1: Summary of muon $W\gamma$, $Z\gamma$ Candidates and Jet-20 QCD Background Passing Successive Photon Cuts. The first row of the first two columns are the number of inclusive W/Z events; The last column in the first row lists the initial number of central, "Extra" jets passing the jet selection criteria. The entries in the other rows are the number of $W/Z/Jet-20$ events with fiducial CEM clusters remaining after the application of successive photon cuts.

are the transverse mass, and the cluster transverse mass. The transverse mass is defined as: $M_T = \sqrt{2|\vec{P_{T\mu}}||\not{E}_T|[1-cos(\Delta\phi_{\not{E}_T-\mu})]}$. The cluster transverse mass (also known as the minimum invariant mass) of the $W+\gamma$ system is defined as: $M_{CT}^W \equiv \sqrt{\left[\left(M_{\ell\gamma}^2 + |\vec{\mathbf{P}}_T^\gamma + \vec{\mathbf{P}}_T^\ell|^2\right)^{\frac{1}{2}} + |\vec{\mathbf{P}}_T^{\bar{\nu}_\ell}|\right]^2 - |\vec{\mathbf{P}}_T^\gamma + \vec{\mathbf{P}}_T^\ell + \vec{\mathbf{P}}_T^{\bar{\nu}_\ell}|^2}$ where $M_{\ell\gamma}$ is the invariant mass of the lepton-photon system.

Figures 4.5-4.8 summarize some of the kinematic properties of muon $W\gamma$ and $Z\gamma$ candidate event samples, overlaid with both the Monte Carlo expectations for the signal in each channel, and with the expected background in each channel. Table 4.3 lists some of the kinematic properties of the muon $W\gamma$ and $Z\gamma$ samples.

Table 4.2: Kinematic Properties of Muon $W\gamma$ Candidates.

	Run # Event #	E_T^γ (GeV)	Q_W (e)	M_T^W (GeV)	M_{CT}^W (GeV)	$\Delta R_{\mu\gamma}$
1	18435 – 606	7.02	−1	50.5	60.5	0.93
2	19177 – 8534	14.71	−1	76.2	94.0	1.44
3	19391 – 43073	20.01	+1	45.0	63.4	1.06
4	19629 – 39980	5.22	+1	79.6	85.4	3.15
5	19932 – 53074	23.58	−1	70.3	106.4	2.22

Table 4.3: Kinematic Properties of Muon $Z\gamma$ Candidates.

	Run # Event #	E_T^γ (GeV)	$M_{\mu^+\mu^-}$ (GeV)	$M_{Z\gamma}$ (GeV)	$\Delta R_{\mu\gamma}$
1	20361 – 6869	6.40	78.5	84.8	0.71
2	20389 – 23545	7.12	84.0	91.3	1.27

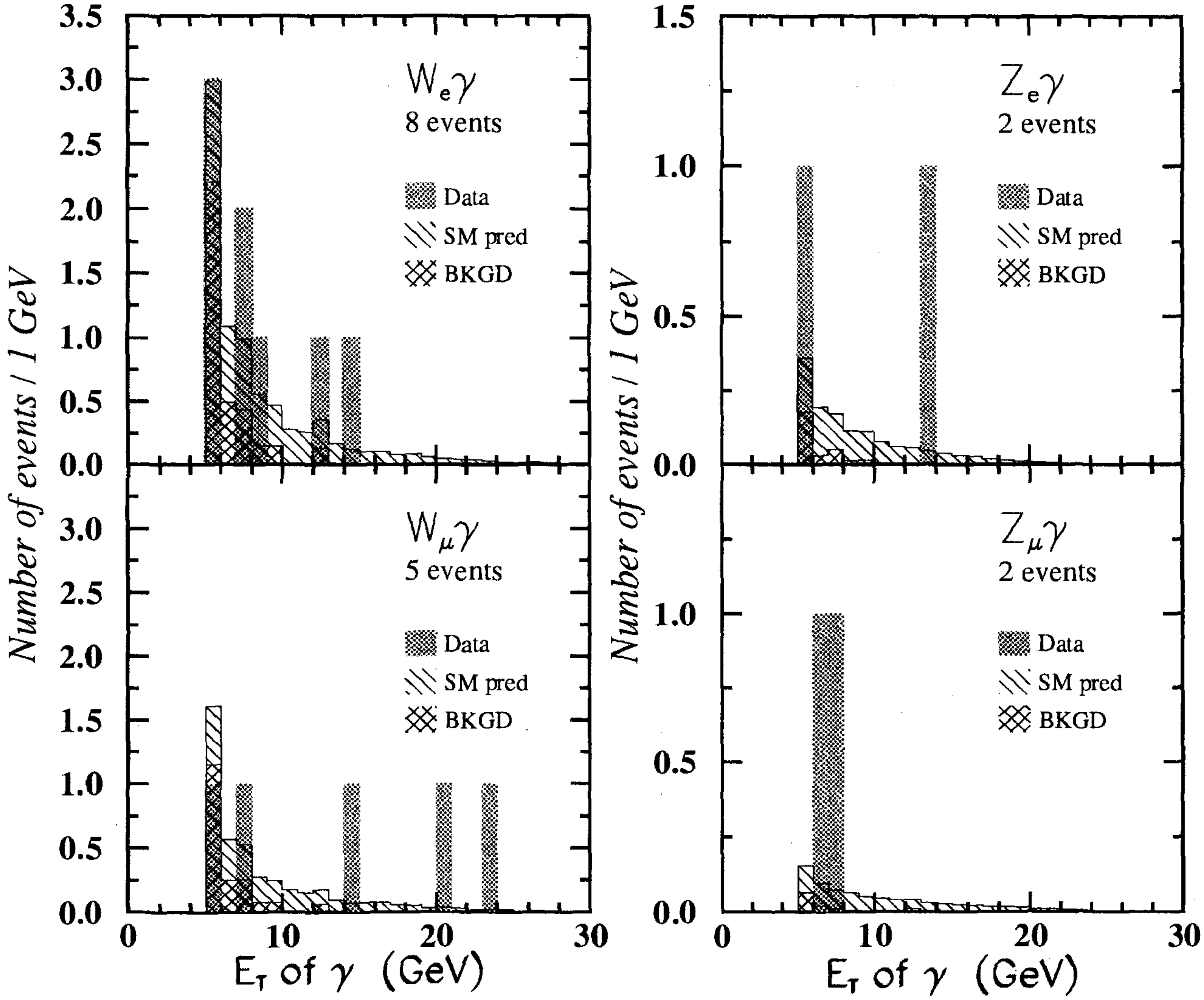

Figure 4.5: E_T of γ, with the data sample, Standard Model predicted signal, and background.

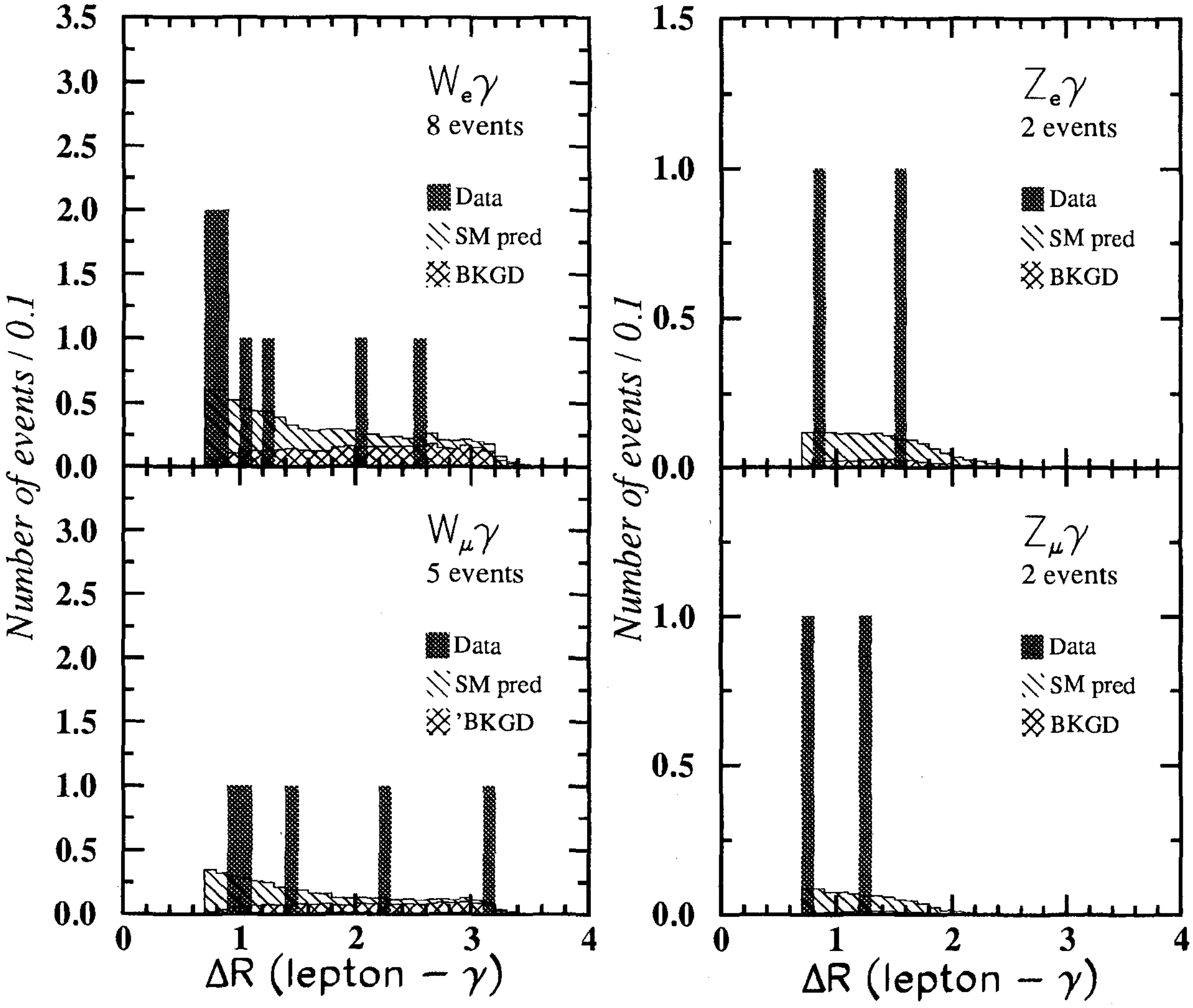

Figure 4.6: $\Delta R_{\ell\gamma}$, with the data sample, Standard Model predicted signal, and background.

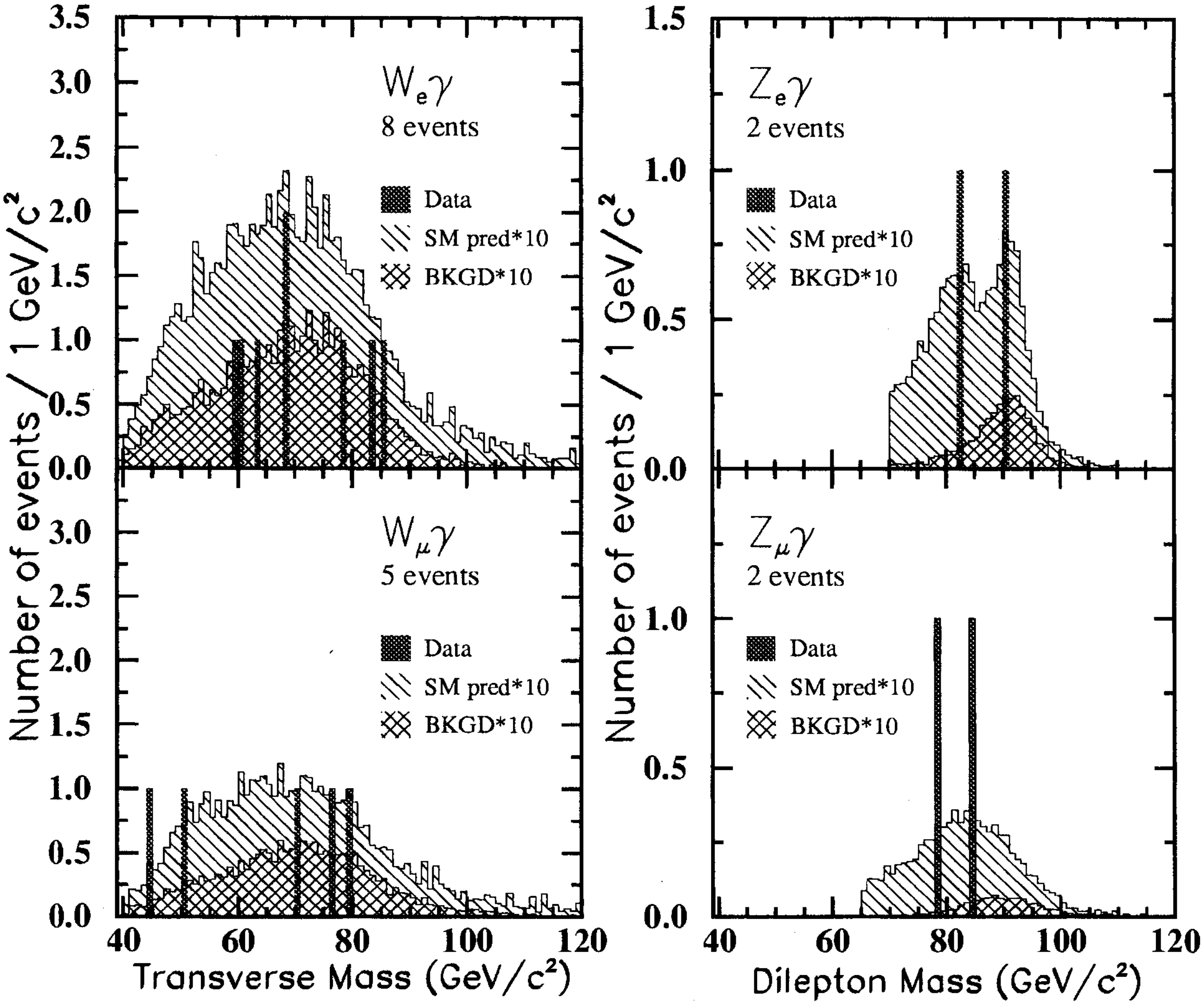

Figure 4.7: Transverse Mass and Di-lepton mass for the W and Z channels respectively with the data sample, Standard Model predicted signal, and background.

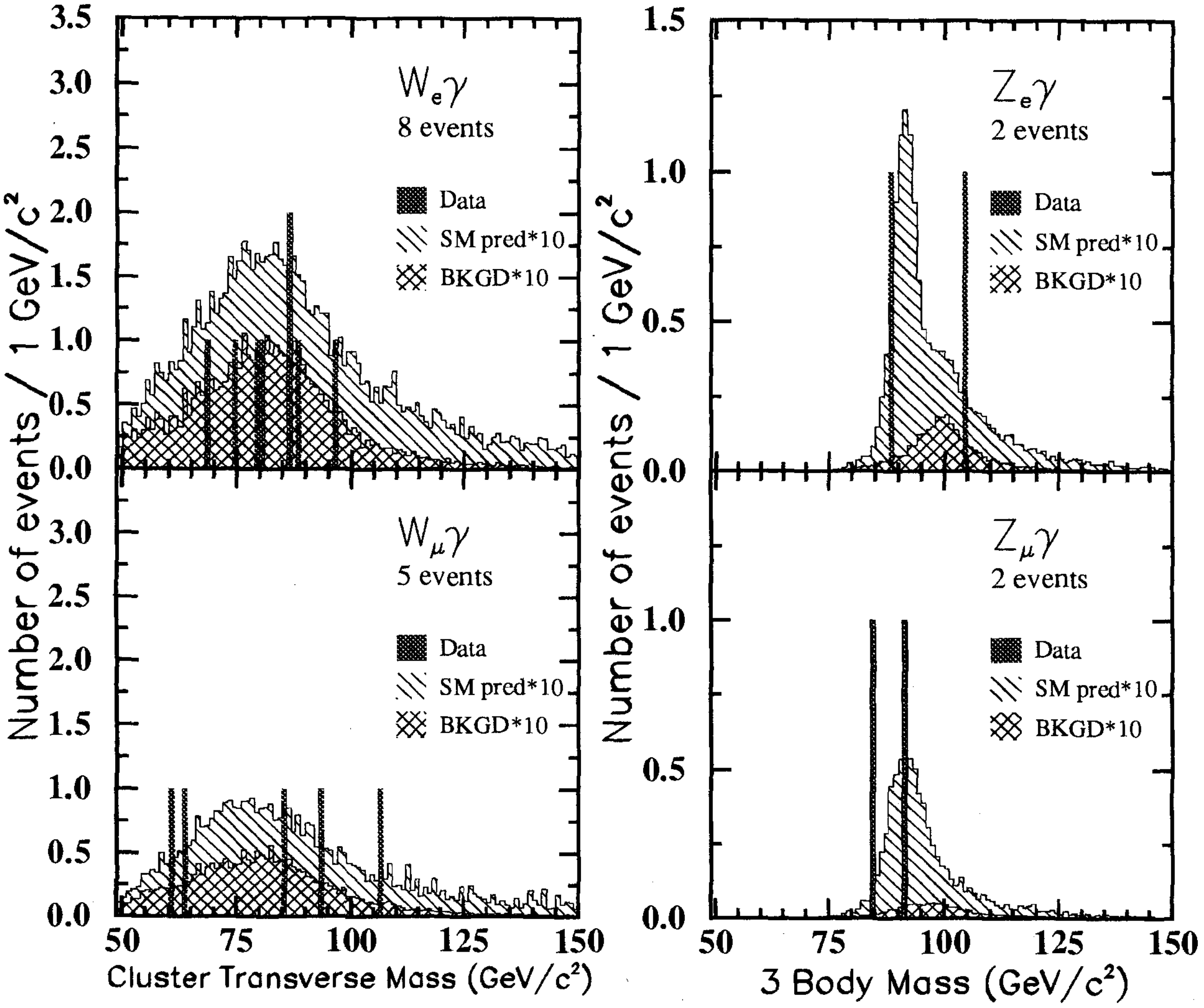

Figure 4.8: Cluster transverse mass and 3 body mass for the W and Z channels respectively, with the data sample, Standard Model predicted signal, and background.

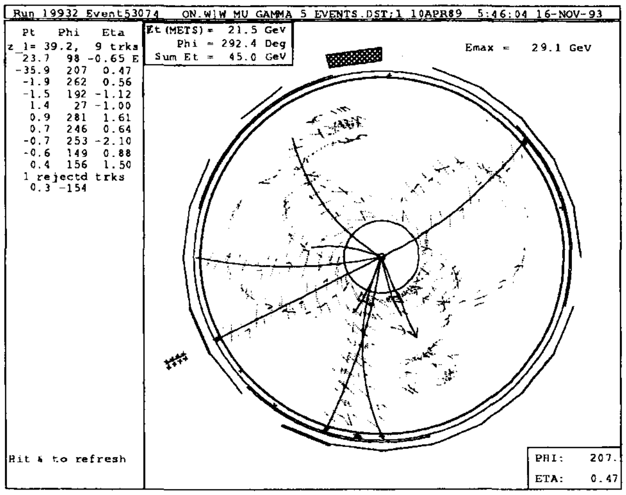

```
Run 19932 Event53074   ON.W|W MU GAMMA 5 EVENTS.DST;1 10APR89  5:46:04 16-NOV-93
  Pt    Phi    Eta     Ɇt(METS) =  21.5 GeV
z_1= 39.2,  9 trks          Phi = 292.4 Deg
 23.7   98 -0.65 E      Sum Et =  45.0 GeV
-35.9  207  0.47
 -1.9  262  0.56
 -1.5  192 -1.12
  1.4   27 -1.00
  0.9  281  1.61
  0.7  246  0.64
 -0.7  253 -2.10
 -0.6  149  0.88
  0.4  156  1.50
 1 rejectd trks
  0.3 -154
```

Figure 4.9: A CTC detector view of one of the $W\gamma$ events.

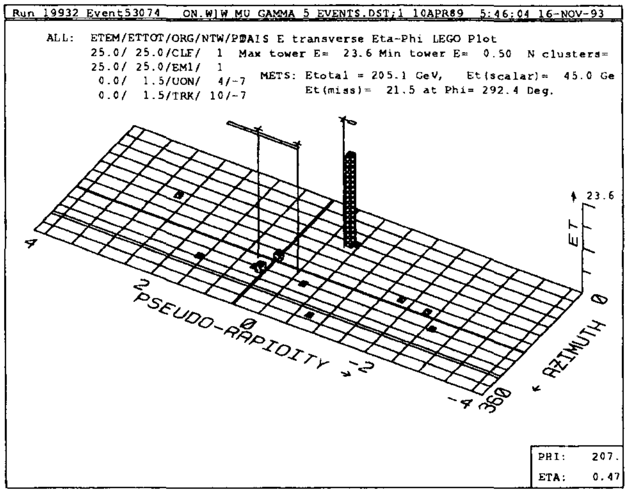

```
Run 19932 Event53074   ON.W|W MU GAMMA 5 EVENTS.DST;1 10APR89  5:46:04 16-NOV-93
  ALL:  ETEM/ETTOT/ORG/NTW/PDAIS E transverse Eta-Phi LEGO Plot
        25.0/ 25.0/CLF/  1  Max tower E=  23.6 Min tower E=  0.50  N clusters=
        25.0/ 25.0/EM1/  1
         0.0/  1.5/UON/  4/-7  METS: Etotal = 205.1 GeV,   Et(scalar)=  45.0 Ge
         0.0/  1.5/TRK/ 10/-7        Et(miss)=  21.5 at Phi= 292.4 Deg.
```

Figure 4.10: A lego plot of the calorimeter for one of the $W\gamma$ events.

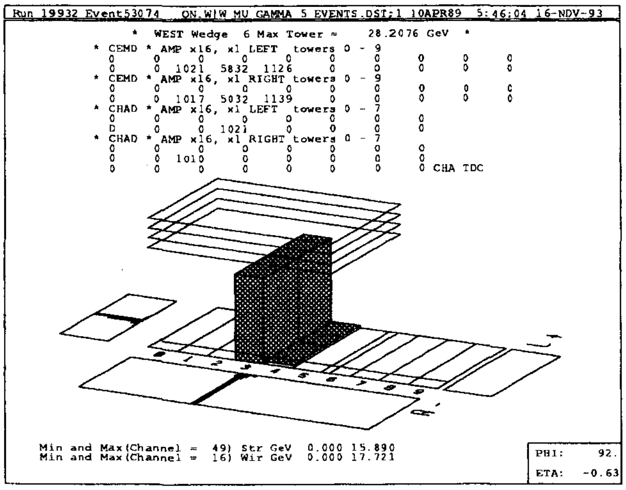

```
Run 19932 Event53074   ON.W|W MU GAMMA 5 EVENTS.DST;1 10APR89  5:46:04 16-NOV-93
          *  WEST Wedge  6 Max Tower =    28.2076 GeV  *
    * CEMD * AMP x16, x1 LEFT  towers 0 - 9
      0    0    0    0    0    0    0    0    0    0
      0    0 1021 5832 1126    0    0    0    0    0
    * CEMD * AMP x16, x1 RIGHT towers 0 - 9
      0    0    0    0    0    0    0    0    0    0
      0    0 1017 5032 1139    0    0    0    0    0
    * CHAD * AMP x16, x1 LEFT  towers 0 - 7
      0    0    0    0    0    0    0    0
      D    0    0 1021    0    0    0    0
    * CHAD * AMP x16, x1 RIGHT towers 0 - 7
      0    0    0    0    0    0    0    0
      0    0 1010    0    0    0    0    0
      0    0    0    0    0    0    0    0 CHA TDC

Min and Max(Channel =  49) Str GeV  0.000 15.890
Min and Max(Channel =  16) Wir GeV  0.000 17.721
```

Figure 4.11: A view of the CES detector showing the photon shower for one of the $W\gamma$ events.

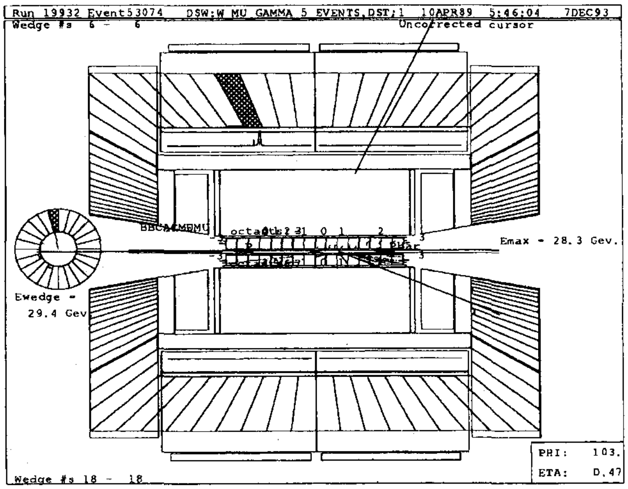

```
Run 19932 Event53074   DSW:W MU GAMMA 5 EVENTS.DST;1  10APR89  5:46:04   7DEC93
Wedge #s  6 -   6                                  Uncorrected cursor
```

Figure 4.12: A side view of detector showing the CTC tracks and calorimeter towers for one of the $W\gamma$ events.

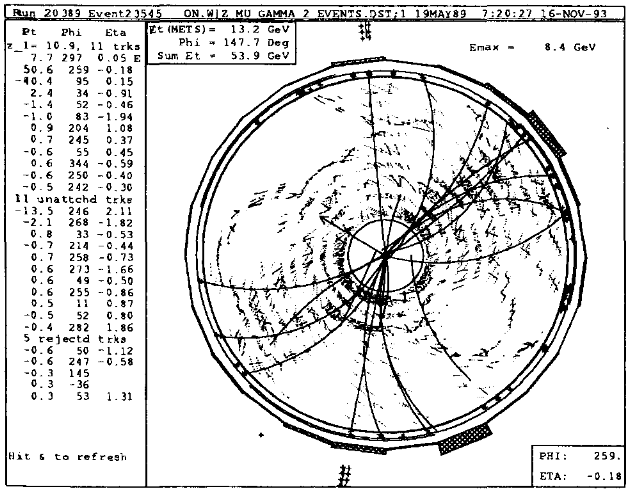

```
Run 20389 Event23545   ON.W|Z MU GAMMA 2 EVENTS.DST;1 19MAY89  7:20:27 16-NOV-93
 Pt    Phi    Eta
z_1= 10.9, 11 trks
   7.7 297  0.05 E
  50.6  259 -0.18
 -40.4   95  0.15
   2.4   34 -0.91
  -1.4   52 -0.46
  -1.0   83 -1.94
   0.9  204  1.08
   0.7  245  0.37
  -0.6   55  0.45
   0.6  344 -0.59
  -0.6  250 -0.40
  -0.5  242 -0.30
11 unattchd trks
 -13.5  246  2.11
  -2.1  268 -1.82
   0.8   33 -0.53
  -0.7  214 -0.44
   0.7  258 -0.73
   0.6  273 -1.66
   0.6   49 -0.50
   0.6  255 -0.86
   0.5   11  0.87
  -0.5   52  0.80
  -0.4  282  1.86
 5 rejectd trks
  -0.6   50 -1.12
  -0.6  247 -0.58
  -0.3  145
   0.3  -36
   0.3   53  1.31

Hit 6 to refresh
```

```
Et(METS)=  13.2 GeV
   Phi = 147.7 Deg
Sum Et =  53.9 GeV
```

Figure 4.13: A CTC detector view of one of the $Z\gamma$ events.

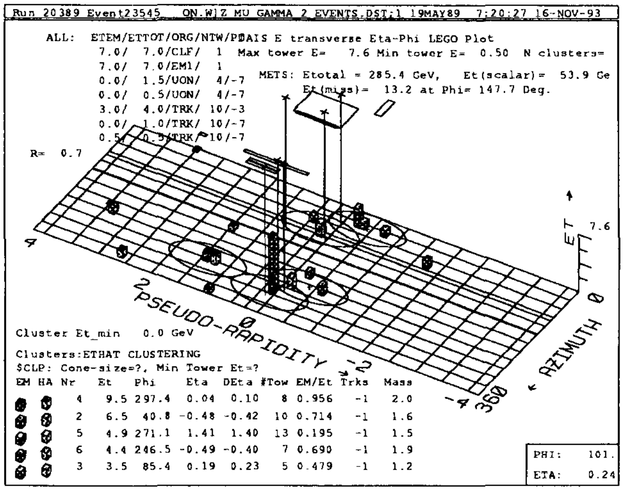

```
Run 20389 Event23545   ON.W|Z MU GAMMA 2 EVENTS.DST;1 19MAY89  7:20:27 16-NOV-93
   ALL:  ETEM/ETTOT/ORG/NTW/PDAIS E transverse Eta-Phi LEGO Plot
          7.0/  7.0/CLF/  1  Max tower E=   7.6 Min tower E=  0.50  N clusters=
          7.0/  7.0/EM1/  1
          0.0/  1.5/UON/  4/-7   METS: Etotal = 285.4 GeV,   Et(scalar)=  53.9 Ge
          0.0/  0.5/UON/  4/-7          Et(miss)=  13.2 at Phi= 147.7 Deg.
          3.0/  4.0/TRK/ 10/-3
          0.0/  1.0/TRK/ 10/-7
          0.5/  0.5/TRK/ 10/-7
  R=  0.7

Cluster Et_min    0.0 GeV
Clusters:ETHAT CLUSTERING
$CLP: Cone-size=?, Min Tower Et=?
EM HA Nr    Et   Phi     Eta   DEta #Tow EM/Et Trks   Mass
        4   9.5 297.4   0.04   0.10   8 0.956  -1    2.0
        2   6.5  40.8  -0.48  -0.42  10 0.714  -1    1.6
        5   4.9 271.1   1.41   1.40  13 0.195  -1    1.5
        6   4.4 246.5  -0.49  -0.40   7 0.690  -1    1.9
        3   3.5  85.4   0.19   0.23   5 0.479  -1    1.2
```

Figure 4.14: A lego plot of the calorimeter for one of the $Z\gamma$ events.

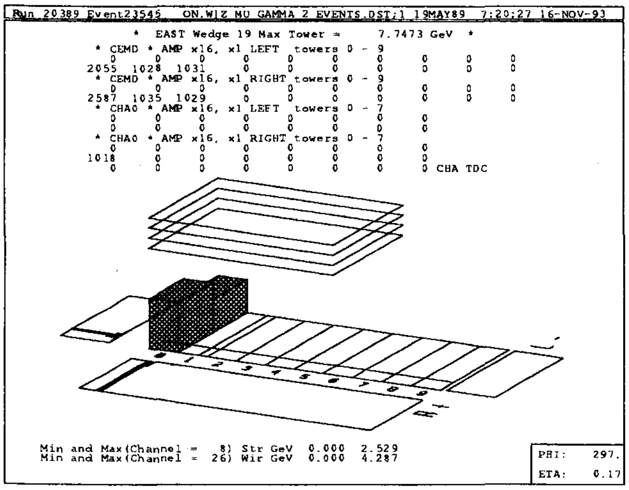

```
Run 20389 Event23545   ON.W|Z MU GAMMA 2 EVENTS.DST;1 19MAY89  7:20;27 16-NOV-93
           *  EAST Wedge 19 Max Tower =      7.7473 GeV  *
       * CEMD * AMP x16, x1 LEFT  towers 0 - 9
         0     0     0     0     0     0     0     0     0     0
      2055  1028  1031     0     0     0     0     0     0     0
       * CEMD * AMP x16, x1 RIGHT towers 0 - 9
         0     0     0     0     0     0     0     0     0     0
      2587  1035  1029     0     0     0     0     0     0     0
       * CHA0 * AMP x16, x1 LEFT  towers 0 - 7
         0     0     0     0     0     0     0     0
         0     0     0     0     0     0     0     0
       * CHA0 * AMP x16, x1 RIGHT towers 0 - 7
         0     0     0     0     0     0     0     0
      1018     0     0     0     0     0     0     0
         0     0     0     0     0     0     0     0 CHA TDC

   Min and Max(Channel =   8) Str GeV  0.000  2.529
   Min and Max(Channel =  26) Wir GeV  0.000  4.287
```

Figure 4.15: A view of the CES detector showing the photon shower for one of the $Z\gamma$ events.

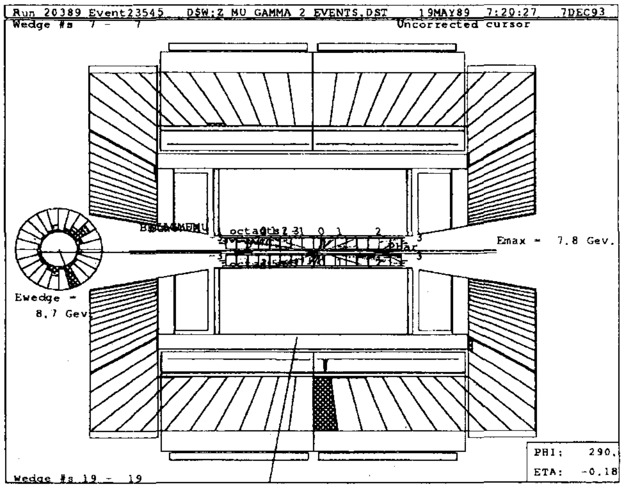

```
Run 20389 Event23545   DSW:Z MU GAMMA 2 EVENTS.DST    19MAY89  7:20:27   7DEC93
Wedge #s  7 -  7                                Uncorrected cursor
```

Figure 4.16: A side view of detector showing the CTC tracks and calorimeter towers for one of the $Z\gamma$ events.

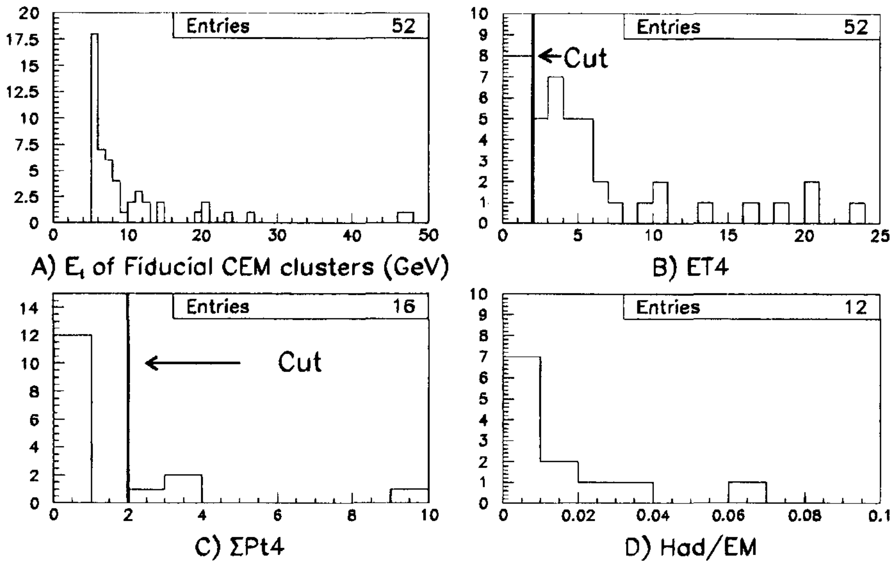

A) E_t of Fiducial CEM clusters (GeV)

B) ET4

C) ΣPt4

D) Had/EM

Figure 4.17: Photon variables for the $W\gamma$ data set. Each plot is for listed variable before the cut is made (See Table 4.4). The high P_T 2^{nd} track cut to remove mis-identified Z's has been made *before* Plot (A). (A) E_T of CEM Fiducial clusters, passing $\Delta R_{\mu\gamma} > 0.7$, (B) Calorimeter Isolation, (C) Tracking isolation (D) Had/EM distribution, (the cut is not indicated because it is a function of E_γ).

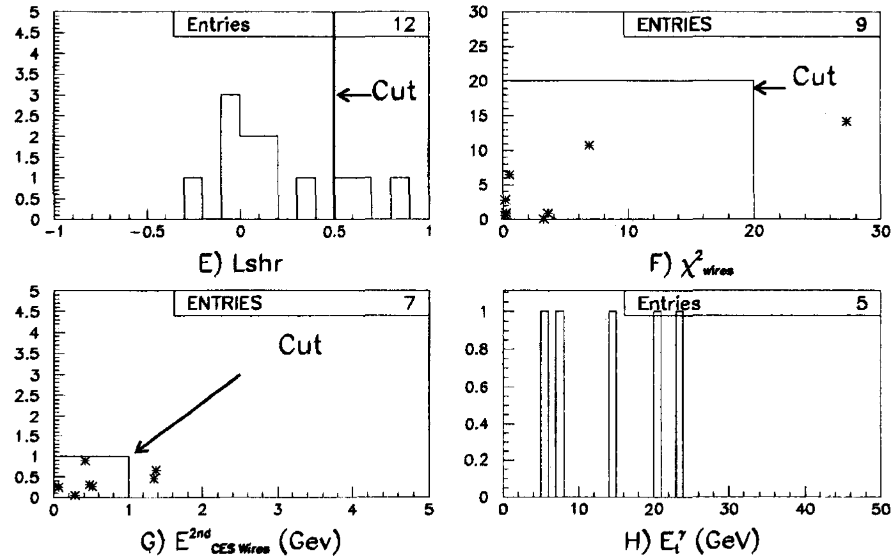

E) Lshr

F) χ^2_{wires}

G) $E^{2nd}_{CES\,Wires}$ (Gev)

H) E_t^γ (GeV)

Figure 4.18: Photon variables for the $W\gamma$ data set. Each plot is for listed variable before the cut is made (See Table 4.4). (E) *Lshr* (F) A scatterplot of CES χ^2_{strip}vs.χ^2_{wires} (G) A scatterplot of CES E_{strip}vs.E_{wires} (H) E_T^γ after all cuts have been made.

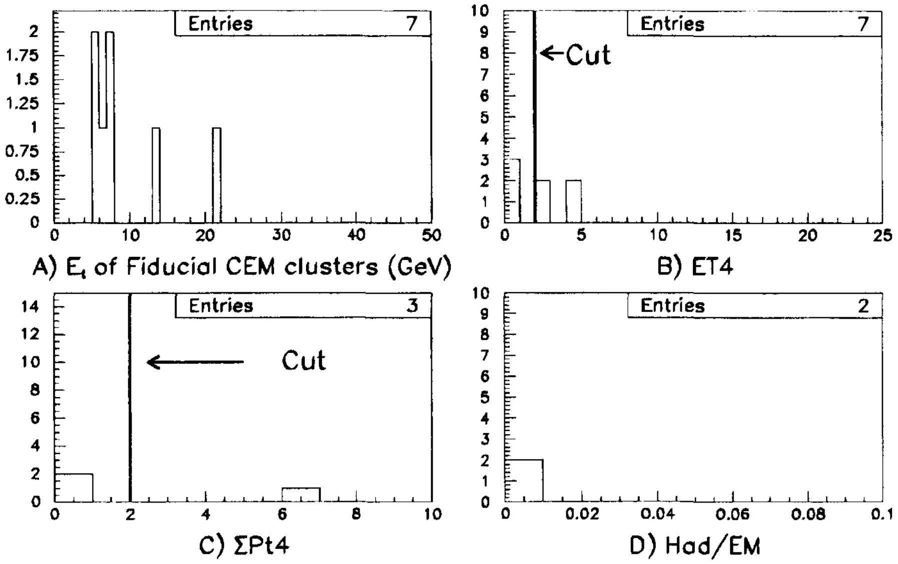

Figure 4.19: Photon variables for the $Z\gamma$ data set. Each plot is for listed variable before the cut is made (See Table 4.4). (A) E_T of CEM Fiducial clusters, passing $\Delta R_{\mu\gamma} > 0.7$, (B) Calorimeter Isolation, (C) Tracking isolation (D) Had/EM distribution, (the cut is not indicated because it is a function of E_γ).

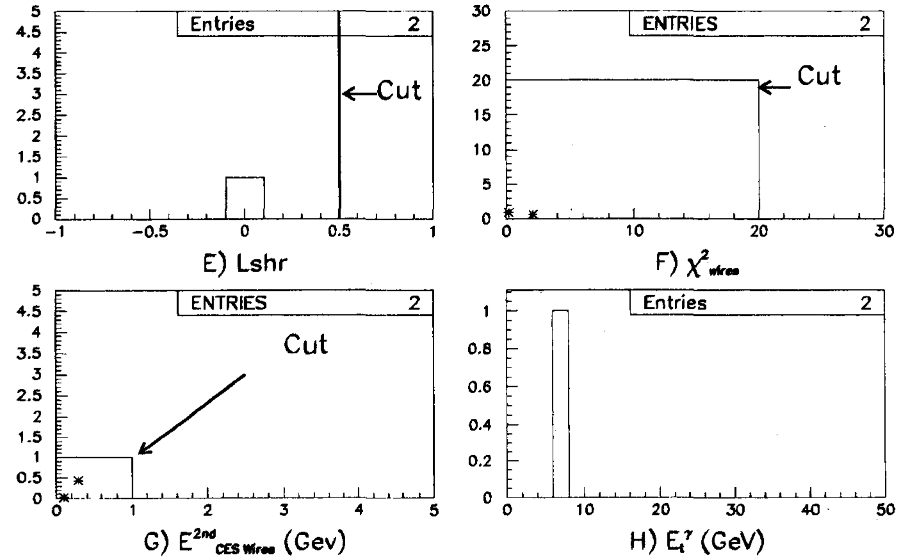

Figure 4.20: Photon variables for the $Z\gamma$ data set. Each plot is for listed variable before the cut is made (See Table 4.4). (E) Lshr (F) A scatterplot of CES χ^2_{strip}vs.χ^2_{wires} (G) A scatterplot of CES E_{strip}vs.E_{wires} (H) E_T^γ after all cuts have been made.

Chapter 5

Determination of Efficiencies and Acceptances

The number of events found in the experimental result, or predicted by the theory, is related to the cross section × branching ratio by:

$$\sigma \cdot B(V_{\mu} + \gamma) \;=\; \frac{\mathcal{N}_{signal}^{V\gamma}}{\int \mathcal{L}_{\mu} dt \cdot \left(A_{V_{\gamma}}^{\mu} \cdot \epsilon_{V_{\gamma}}^{\mu}\right)} \;=\; \frac{\mathcal{N}_{observed}^{V\gamma} - \Sigma \mathcal{N}_{background}^{V\gamma}}{\int \mathcal{L}_{\mu} dt \cdot \left(A_{V_{\gamma}}^{\mu} \cdot \epsilon_{V_{\gamma}}^{\mu}\right)} \tag{5.1}$$

where $V = W$ or Z; $\mathcal{N}_{signal}^{V\gamma} \;=\; \mathcal{N}_{observed}^{V\gamma} - \Sigma \mathcal{N}_{background}^{V\gamma}$ is the number of signal $W\gamma$ or $Z\gamma$ events; $\mathcal{N}_{observed}^{V\gamma}$ is the number of observed $W\gamma$ or $Z\gamma$ events, and $\Sigma \mathcal{N}_{background}^{V\gamma}$ is the number of background events expected in each of the data samples. The integrated luminosity factor is $\int \mathcal{L}_{\mu} dt$. The product term $\left(A_{V_{\gamma}}^{\mu} \cdot \epsilon_{V_{\gamma}}^{\mu}\right)$ is the overall acceptance × efficiency factor for selecting muon $W\gamma$ and $Z\gamma$ events, and is a product of a number of acceptances × efficiency factors.

For $W\gamma$:

$$A^{\mu}_{W\gamma} \cdot \epsilon^{\mu}_{W\gamma} = \epsilon_{zvx} \cdot A^{\mu}_{M^T_W} \cdot \left(A^{\mu}_{W} \cdot T^{\mu} \cdot \epsilon^{\mu}_{cent_T} \cdot \epsilon^{\mu}_{Wcos}\right) \cdot \left(f^{\gamma_\mu}_{Wcem} \cdot A^{\gamma_\mu}_{Wcem} \cdot \epsilon^{\gamma}_{cem}\right) \tag{5.2}$$

For $Z\gamma$:

$$\begin{aligned} A^{\mu}_{Z\gamma} \cdot \epsilon^{\mu}_{Z\gamma} &= \frac{1}{f^{\mu}_{DY}} \cdot \epsilon_{zvx} \cdot A^{\mu}_{M_Z} \cdot \left(A^{\mu}_{Z} \cdot T^{\mu} \cdot \epsilon^{\mu}_{cent_T} \cdot \epsilon^{\mu}_{Zcos}\right) \\ &\quad \times \Big[\left\{ f^{\mu}_{Zgg} \cdot (2 - T^{\mu}) \cdot \left(2\epsilon^{\mu}_{cent_{L_1}} - \epsilon^{\mu}_{cent_T}\right)\right\} \cdot \left(f^{\gamma_\mu}_{Zgg} \cdot A^{\gamma_\mu}_{Zgg} \cdot \epsilon^{\gamma}_{cem}\right) \\ &\quad + \left(f^{\mu}_{Zgs} \cdot \epsilon^{\mu}_{cent_{L_2}}\right) \cdot \left(f^{\gamma_\mu}_{Zgs} \cdot A^{\gamma_\mu}_{Zgs} \cdot \epsilon^{\gamma}_{cem}\right)\Big] \\ &= \frac{1}{f^{\mu}_{DY}} \cdot \epsilon_{zvx} \cdot A^{\mu}_{M_Z} \cdot \left(T^{\mu} \cdot \epsilon^{\mu}_{cent_T} \cdot \epsilon^{\mu}_{Zcos}\right) \\ &\quad \times \Big[\left\{ A^{\mu}_{Zgg} \cdot (2 - T^{\mu}) \cdot \left(2\epsilon^{\mu}_{cent_{L_1}} - \epsilon^{\mu}_{cent_T}\right)\right\} \cdot \left(f^{\gamma_\mu}_{Zgg} \cdot A^{\gamma_\mu}_{Zgg} \cdot \epsilon^{\gamma}_{cem}\right) \\ &\quad + \left(A^{\mu}_{Zgs} \cdot \epsilon^{\mu}_{cent_{L_2}}\right) \cdot \left(f^{\gamma_\mu}_{Zgs} \cdot A^{\gamma_\mu}_{Zgs} \cdot \epsilon^{\gamma}_{cem}\right)\Big] \end{aligned} \tag{5.3}$$

The subscripts gg refer to a Z where both muons are "Gold", while the subscript gs is a Z with one "Gold" and one "Silver" muon. The factor f^{μ}_{DY} (< 1) explicitly corrects for the removal of the Drell-Yan $DY + \gamma$ contribution to events in the $Z + \gamma$ data within the $Z \rightarrow \mu^+\mu^-$ mass window, as well as the loss of $Z + \gamma$ events outside the $Z \rightarrow \mu^+\mu^-$ mass window. The factor ϵ_{zvx} is the efficiency of the $|z_{\text{vertex}}| < 60$ cm cut, and is common to both data samples. The factor $A^{\mu}_{M^T_W}$ is the acceptance of the transverse mass $M^T_W > 40$ GeV/c^2 cut for $W\gamma$ events passing all other cuts; $A^{\mu}_{M_Z}$ is the acceptance of the Z mass-window cut for $Z\gamma$ events passing all other cuts. The acceptance factor $A^{\mu}_{W} = A^{\mu}_{W\ P_T} \cdot A^{\mu}_{W fid\ cmu} \cdot A^{\bar{\nu}_\mu}_{W\ \not{E}_T}$ is the overall kinematic × geometrical acceptance for $W \rightarrow \mu\,\bar{\nu}_\mu$ in muon $W\gamma$ events, where $A^{\mu}_{W\ P_T}$ is the kinematical acceptance for central fiducial muons passing the $P^{\mu}_T > 20$ GeV cut, $A^{\mu}_{W fid\ cmu}$

is the geometrical acceptance for fiducial central muons and $A^{\bar{\nu}_\mu}_{W\ \not{E}_T}$ is the kinematic acceptance for the $\not{E}_T > 20\ GeV$ cut.

The overall kinematic × geometrical acceptance factor for Z decays is $A^\mu_Z = A^\mu_{Zgg} + A^\mu_{Zgs}$, where the factors A^μ_{Zgg}, A^μ_{Zgs} are the overall kinematical × geometrical acceptances for the classes of Gold-Gold and Gold-Silver dimuons from Z decay, respectively. The overall kinematic × geometrical acceptance factors for the two classes are products of individual kinematic × geometrical acceptance factors:

$$A^\mu_{Zgx} = \left(A^{\mu_1}_{Zg\ P_T} \cdot A^{\mu_1}_{Zg\ fid\ cmu}\right) \cdot \left(A^{\mu_2}_{Zx\ P_T} \cdot A^{\mu_2}_{Zx\ fid}\right) \tag{5.4}$$

where $gx = gg$ or gs, and $A^{\mu_1}_{Zg\ P_T}$ is the kinematic acceptance for the commonly-selected "Gold" muon passing the $P^\mu_T > 20\ GeV/c$ cut and $A^{\mu_1}_{Zg\ fid\ cmu}$ is the geometrical fiducial acceptance associated with the central muon system. The factor $A^{\mu_2}_{Zx\ P_T}$ is the kinematic acceptance for the second muon passing the $P^\mu_T > 20\ GeV/c$ cut and $A^{\mu_2}_{Zx\ fid}$ is the geometrical acceptance for either the fiducial acceptance ($x = g$), or the allowed non-fiducial acceptance ($x = s$). The corresponding acceptance fractions f^μ_{Zgg} and f^μ_{Zgs} are given by $f^\mu_{Zgg} = A^\mu_{Zgg}/A^\mu_Z$ and $f^\mu_{Zgs} = A^\mu_{Zgs}/A^e_Z$, respectively.

The overall W/Z muon trigger efficiency for the common "Gold" central muon selection is $T^\mu = \epsilon^\mu_{L1} \cdot \epsilon^\mu_{L2} \cdot \epsilon^\mu_{L3}$, where the ϵ^μ_{Li}, $i = 1 - 3$ are the individual level-1 - level-3 muon trigger efficiencies, respectively.

The overall "Gold" central fiducial muon selection efficiency, common for both W and Z boson decay is given by:

$$\epsilon^\mu_{cent_T} = \epsilon^{cmu}_{iso} \cdot \epsilon^{cmu}_{mi} \cdot \epsilon^{cmu}_{stub} \cdot \epsilon^{cmu}_{trk} \cdot \epsilon^{cmu}_{\Delta x} \tag{5.5}$$

where the individual efficiencies for the common central muon selection are the isolation $I < 0.1$ cut, ϵ_{iso}^{cmu}; the minimum ionizing cut, ϵ_{mi}^{cmu}; the CMU stub-finding efficiency, ϵ_{stub}^{cmu}; the CTC re-tracking efficiency for the $P_T^{\mu} > 20\ GeV/c$ cut, ϵ_{trk}^{cmu}; and the CTC-CMU $\Delta r - \phi < 1.5\ cm$ track-stub matching cut, $\epsilon_{\Delta x}^{cem}$.

The overall "Silver" central fiducial and non-fiducial muon selection efficiencies for Z boson decay are respectively given by:

$$\epsilon_{cent_{L_1}}^{\mu} = \epsilon_{mi}^{cmu} \cdot \epsilon_{stub}^{cmu} \cdot \epsilon_{trk}^{cmu} \tag{5.6}$$

$$\epsilon_{cent_{L_2}}^{\mu} = \epsilon_{mi}^{cmu} \cdot \epsilon_{trk}^{cmu} \tag{5.7}$$

The factors $\epsilon_{W,Z\ cos}^{\mu}$ account for a small over-efficiency in the removal of cosmic ray background from the $W\gamma$ and $Z\gamma$ data samples, respectively.

For central photons in $W\gamma$ events, the factor $f_{Wcem}^{\gamma\mu}$ is defined as the fraction of all photons that are central ($|\eta_\gamma| < 1.1$), which are produced in $W\gamma$ events where the W decay leptons pass the W selection requirements and the photon has already satisfied the $E_T^{\gamma} > 5.0\ GeV$ and $\Delta R_{\mu\gamma} > 0.7$ requirements. The photon acceptance factor for $W\gamma$ is

$$\begin{aligned} A_{Wcem}^{\gamma\mu} &= A_{W\ E_T^{\gamma}}^{\gamma\mu} \cdot A_{W fid\ cem}^{\gamma\mu} \cdot A_{W\ \Delta R_{\mu\gamma}}^{\gamma\mu} = 1 \cdot A_{W fid\ cem}^{\gamma\mu} \cdot 1 \\ &= A_{W fid\ cem}^{\gamma\mu} \end{aligned} \tag{5.8}$$

while for $Z\gamma$ it is

$$A_{Zgx}^{\gamma\mu} = A_{Zgx\ E_T^{\gamma}}^{\gamma\mu} \cdot A_{Zgx\ fid\ cem}^{\gamma\mu} \cdot A_{Zgx\ \Delta R_{\mu\gamma}}^{\gamma\mu} = 1 \cdot A_{Zgx\ fid\ cem}^{\gamma\mu} \cdot 1$$

$$= A^{\gamma\mu}_{Zgx\ fid\ cem} \tag{5.9}$$

where $gx = gg$, or gs for $Z\gamma$.

The portion of the total production cross section × branching ratio of interest is that with photons above $E_T^{\gamma} > 5.0\ GeV$ and muon-photon angular separation $\Delta R_{\mu\gamma} > 0.7$. Thus for both $W\gamma$ and $Z\gamma$ the kinematic acceptance factor $A^{\gamma\mu}_{W\ E_T^{\gamma}} \equiv 1$ and $A^{\gamma\mu}_{Z\ E_T^{\gamma}} \equiv 1$, and the lepton-photon angular separation acceptance factor for central photons is $A^{\gamma\mu}_{W\ \Delta R_{\mu\gamma}} \equiv 1$ and $A^{\gamma\mu}_{Z\ \Delta R_{\mu\gamma}} \equiv 1$, since by definition of the $\sigma \cdot BR(W + \gamma)$ and $\sigma \cdot BR(Z + \gamma)$ cross sections, all central photons with W/Z bosons must have $E_T^{\gamma} > 5.0\ GeV$ and $\Delta R_{\mu\gamma} > 0.7$. The factor $A^{\gamma\mu}_{Wfid\ cem}$ is the geometrical acceptance for photons which are in the central ($|\eta_{\gamma}| < 1.1$) region for $W\gamma$ events with W decay muon passing the W selection requirements and central photons already satisfying the $E_T^{\gamma} > 5.0\ GeV$ and $\Delta R_{\mu\gamma} > 0.7$ requirements. Similarly, $A^{\gamma\mu}_{Zfid\ cem}$ is the geometrical acceptance for photons which are in the central ($|\eta_{\gamma}| < 1.1$) region for $Z\gamma$ events with Z decay muons passing the Z selection requirements for both cases of "Gold-Gold" and "Gold-Silver" muon pairs, and central photons already satisfying the $E_T^{\gamma} > 5.0\ GeV$ and $\Delta R_{\mu\gamma} > 0.7$ requirements. The product terms $f^{\gamma\mu}_{Wcem} \cdot A^{\gamma\mu}_{Wcem}$ and $f^{\gamma\mu}_{Zcem} \cdot A^{\gamma\mu}_{Zcem}$ are therefore the acceptance factor for central fiducial photons from $W\gamma/Z\gamma$ events that have already satisfied the W/Z selection and $E_T^{\gamma} > 5.0\ GeV$ and $\Delta R_{\mu\gamma} > 0.7$ requirements.

The central fiducial photon selection efficiency, common to both $W\gamma$ and $Z\gamma$ data sets, is given by

$$\begin{aligned}\epsilon^{\gamma}_{cem} &= \epsilon^{\gamma}_{ET4} \cdot \epsilon^{\gamma}_{PT4} \cdot \epsilon^{\gamma}_{N3D} \cdot \\ &\quad \epsilon^{\gamma}_{Had/EM} \cdot \epsilon^{\gamma}_{Lshr} \cdot \epsilon^{\gamma}_{\chi^2_{stp}+\chi^2_{wir}} \cdot \epsilon^{\gamma}_{no\ 2^{nd}\ CES} \cdot \mathcal{P}^{\gamma}_{\overline{conv}} \cdot \mathcal{S}^{cem}_{e\rightarrow\gamma}\end{aligned} \tag{5.10}$$

where the sequential efficiencies are:

- $\epsilon^{\gamma}_{cem} \equiv$ calorimeter isolation cut efficiency, $ET4 < 2.0\ GeV$.
- $\epsilon^{\gamma}_{PT4} \equiv$ tracking isolation efficiency, $PT4 < 2.0\ GeV$.
- $\epsilon^{\gamma}_{N3D} \equiv$ efficiency of; No 3-dimensional track passing through the cluster, $N3D = 0$.
- $\epsilon^{\gamma}_{Had/EM} \equiv$ the Had/EM cut efficiency.
- $\epsilon^{\gamma}_{Lshr} \equiv$ the $L_{shr} < 0.5$ cut efficiency.
- $\epsilon^{\gamma}_{\chi^2_{stp}+\chi^2_{wir}} \equiv$ CES $\chi^2_{strip} < 20$ and $\chi^2_{wire} < 20$ cut efficiency.
- $\epsilon^{\gamma}_{no\ 2^{nd}\ CES} \equiv$ $E^{ces}_{2^{nd}} > 1\ GeV$ cut efficiency.

The term $\mathcal{P}^{\gamma}_{\overline{conv}}$ is the photon survival probability for a photon to traverse the material of the inner central detector without converting to an e^+e^- pair. The factor $\mathcal{S}^{cem}_{e\to\gamma}$ is a small correction to account for differences in EM shower development for electrons *vs.* photons, since electron test beam data was used to determine some of the individual photon efficiencies, as discussed in greater detail below.

5.1 Muon Trigger and Event Selection Efficiencies

Since the starting point for this analysis was the same inclusive data set as was used in the determination of the muon W and Z $\sigma \cdot B$ cross sections [4] and the W/Z cross section ratios [5], the muon efficiencies found in those analyses are used in this analysis. The muon trigger efficiencies[29] and muon selection efficiencies[30] were determined using a combination of J/ψ events, cosmic ray studies, and the $2^{'nd}$ leg of muon Z's. The results of these studies are summarized in Table 5.1.

Table 5.1: Individual Muon Efficiencies for $W\gamma$ and $Z\gamma$ Data Samples. The statistical uncertainty associated with each quantity is given.

f^{μ}_{DY}	$97.0 \pm 0.2\%$	$65 < M^{\mu}_{Z} < 115$ GeV/c^2
ϵ_{zvx}	$95.4 \pm 0.1\%$	$\lvert z_{vtx} \rvert < 60$ cm
ϵ^{cmu}_{iso}	$98.0 \pm 1.0\%$	Muon Isolation Cut ($\Delta R = 0.4$)
ϵ^{cmu}_{mi}	$98.7^{+0.3}_{-0.4}\%$	Minimum Ionizing Energy Cut
ϵ^{cmu}_{trk}	$98.7 \pm 1.0\%$	CTC Re-Tracking
ϵ^{cmu}_{stub}	$98.6^{+1.2}_{-3.3}\%$	CMU Stub Finding
$\epsilon^{cmu}_{\Delta x}$	$96.0 \pm 1.0\%$	$\Delta z < 2.0$ cm Track Match
ϵ^{μ}_{Wcos}	$99.7 \pm 0.2\%$	Cosmic Ray Filter
ϵ^{μ}_{Zcos}	$99.7 \pm 0.2\%$	Cosmic Ray Filter
ϵ^{μ}_{L1}	$93.4 \pm 0.4\%$	Level-1 Central Muon Trigger
ϵ^{μ}_{L2}	$97.2^{+1.5}_{-2.7}\%$	Level-2 Central Muon Trigger
ϵ^{μ}_{L3}	$100.0^{+0.0}_{-2.8}\%$	Level-3 Central Muon Trigger

5.2 Determination of Photon Efficiencies

The overall efficiency for central photons was determined from the product of the efficiencies for the cuts described in the previous section. The Table 5.4 summarize these results.

5.2.0.11 Calorimeter Isolation Efficiency

The efficiency for each isolation cut in the central calorimeter ($|\eta| < 1.1$) is determined by measuring the fraction of the time that the measured value in a "random cone" in various data sets passes the cut. A "random cone" is produced by selecting a random direction in ϕ and η from a flat distribution, and then forming all the quantities of a cluster, i.e. $ET4$, PT4 and N3D, etc.

The efficiency of the $ET4$ cut was determined by measuring random cones in the W/Z events that were more than $\Delta R = 0.7$ away from the W/Z decay muons. As a cross check, the efficiencies for random cones in BAUR/QFL/ISAJET (See Section 5.3) Monte Carlo simulated $W\gamma$ and $Z\gamma$ events were determined. The efficiency found by throwing random cones in a QCD

Table 5.2: CEM Photon Efficiency Determination – Isolation Variables. The statistical uncertainty associated with each quantity is given.

Data Sample	ϵ^{γ}_{ET4}	$\epsilon^{\gamma}_{ET4} \cdot \epsilon^{\gamma}_{PT4}$	$\epsilon^{\gamma}_{ET4} \cdot \epsilon^{\gamma}_{PT4} \cdot \epsilon^{\gamma}_{N3D}$
W_e Random Cones	$95.5 \pm 0.5\%$	$93.4 \pm 0.6\%$	$89.2 \pm 0.7\%$
W_μ Random Cones	$95.9 \pm 0.4\%$	$93.1 \pm 0.6\%$	$88.6 \pm 0.7\%$
Z_e Random Cones	$95.8 \pm 0.6\%$	$93.6 \pm 0.7\%$	$89.1 \pm 0.9\%$
Z_μ Random Cones	$94.5 \pm 1.2\%$	$91.1 \pm 1.4\%$	$87.3 \pm 1.6\%$
QFL e $W\gamma$ MC	$98.9 \pm 0.6\%$	$96.4 \pm 1.0\%$	$90.2 \pm 1.5\%$
QFL μ $W\gamma$ MC	$99.3 \pm 0.7\%$	$96.6 \pm 1.2\%$	$93.3 \pm 1.6\%$
QFL e $Z\gamma$ MC	$97.9 \pm 1.2\%$	$97.0 \pm 1.3\%$	$91.9 \pm 2.0\%$
QFL μ $Z\gamma$ MC	$98.3 \pm 0.7\%$	$94.8 \pm 1.1\%$	$91.9 \pm 1.4\%$
MinBias Random Cones	$98.6 \pm 0.2\%$	$97.7 \pm 0.2\%$	$92.8 \pm 0.2\%$
Jet-20a Random Cones	$99.1 \pm 0.1\%$	$97.6 \pm 0.1\%$	$92.7 \pm 0.2\%$
Jet-20b Random Cones	$92.7 \pm 0.2\%$	$89.3 \pm 0.3\%$	$84.2 \pm 0.3\%$

jet data sample[1] (the Jet-20 data sample is used as the QCD jet data sample) and the efficiency found by throwing random cones in the Minimum Bias events were used to bracket the extrema of the allowable range for these efficiencies.

5.2.0.12 PT4 and N3D Isolation Efficiencies

The efficiency for the summed P_T in a cone of $\Delta R = 0.4$, after the $ET4$ cut for central photons, and the efficiency for the "No 3D CTC Track" pointing at the CEM cluster (N3D=0) after the $ET4$ and PT4 cuts, were also determined from these same data samples, and in the same way as the $ET4$ efficiency was measured.

5.2.0.13 Other Photon Selection Efficiencies

The photon efficiencies for $Had/EM < 0.055 + 0.00045 * E$, LSHR < 0.5, $\chi^2_{\rm strip} < 20.0$ and $\chi^2_{\rm wire} < 20.0$ and the no 2^{nd} CES strip/wire cluster $E_{CES\ 2^{nd}} > 1\ GeV$ cuts were determined from $5 - 50\ GeV$ CEM electron test beam data. The QFL Baur muon $W\gamma/Z\gamma$ Monte Carlo

---

[1] See Appendix B for a description of the Jet-20 data sample selection criteria.

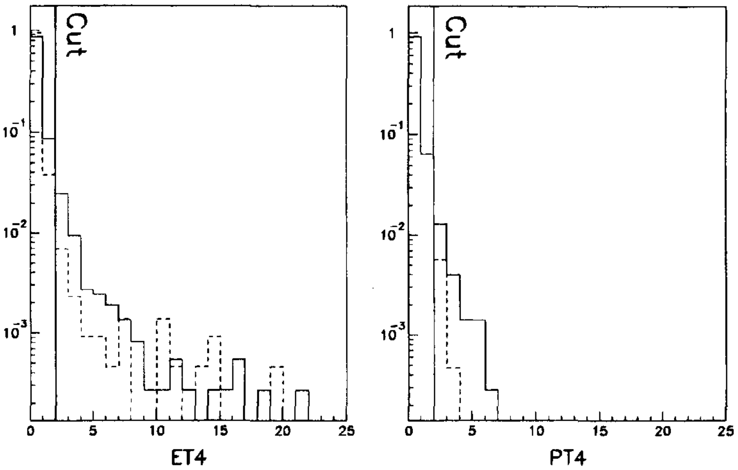

Figure 5.1: $ET4$ and PT4 distribution for W/Z (solid lines) and Baur/QFL/Isajet Monte Carlo (dashed lines) random cones, with the respective cuts indicated.

simulated data, and the QFL photon and electron Monte Carlo simulations over a range of $5 < E_T < 15$ GeV, were used as cross checks of the CEM test beam results.

Table 5.3: CEM Photon Efficiency Determination – EM Shower Variables. The statistical uncertainty associated with each quantity is given.

Data Sample	$\epsilon^{\gamma}_{Had/EM}$	ϵ^{γ}_{Lshr}	$\epsilon^{\gamma}_{\chi^2_{stp}+\chi^2_{wir}}$	$\epsilon^{\gamma}_{no\ 2^{nd}\ CES}$
5 GeV e TB	$98.9 \pm 0.2\%$	$99.9 \pm 0.1\%$	$97.3 \pm 0.3\%$	$98.0 \pm 0.1\%$
10 GeV e TB	$99.6 \pm 0.1\%$	$98.8 \pm 0.4\%$	$96.2 \pm 0.4\%$	$97.9 \pm 0.1\%$
18 GeV e TB	$99.1 \pm 0.9\%$	$100.0^{+0.0}_{-1.7}\%$	$98.2 \pm 1.8\%$	$98.2 \pm 1.6\%$
30 GeV e TB	$98.9 \pm 0.9\%$	$100.0^{+0.0}_{-1.1}\%$	$99.2 \pm 0.7\%$	$98.2 \pm 2.0\%$
50 GeV e TB	$98.0 \pm 0.3\%$	$99.9 \pm 0.1\%$	$99.2 \pm 0.2\%$	$97.6 \pm 1.4\%$
QFL e $W\gamma$ MC	$99.3 \pm 0.6\%$	$99.7 \pm 0.3\%$	$98.4 \pm 0.5\%$	$94.6 \pm 1.2\%$
QFL μ $W\gamma$ MC	$99.7 \pm 0.3\%$	$100.0^{+0.0}_{-0.4}\%$	$97.5 \pm 1.1\%$	$95.0 \pm 1.6\%$
QFL e $Z\gamma$ MC	$99.2 \pm 0.8\%$	$100.0^{+0.0}_{-0.5}\%$	$95.4 \pm 1.6\%$	$95.0 \pm 2.4\%$
QFL μ $Z\gamma$ MC	$99.4 \pm 0.5\%$	$100.0^{+0.0}_{-0.2}\%$	$97.7 \pm 0.8\%$	$95.2 \pm 1.2\%$
QFL γ MC $5 - 15$ GeV	$99.7 \pm 0.1\%$	$99.8 \pm 0.1\%$	$97.4 \pm 0.3\%$	$96.8 \pm 0.3\%$
QFL e MC $5 - 15$ GeV	$99.9 \pm 0.1\%$	$99.9 \pm 0.1\%$	$97.9 \pm 0.2\%$	$95.8 \pm 0.3\%$

5.2.0.14 Comments on the Photon Efficiency Measurements

It can be seen that the photon efficiencies obtained from random cones thrown in the muon inclusive W/Z data samples are in good agreement with one another.

Table 5.4: Overall CEM Photon Efficiency Determination. The statistical and systematic uncertainties associated with each quantity are given.

ϵ^{γ}_{ET4}	$95.7 \pm 0.3 \pm 0.5\%$	Calorimeter Isolation
ϵ^{γ}_{PT4}	$97.4 \pm 0.4 \pm 0.8\%$	Tracking Isolation
ϵ^{γ}_{N3D}	$95.3 \pm 0.5 \pm 0.7\%$	No track @ EM Cluster
$\epsilon^{\gamma}_{Had/EM}$	$99.2 \pm 0.1 \pm 0.8\%$	Had/EM Cut
ϵ^{γ}_{Lshr}	$99.9 \pm 0.1 \pm 0.3\%$	Lateral Shower Cut
$\epsilon^{\gamma}_{\chi^2_{stp}+\chi^2_{wir}}$	$98.4 \pm 0.1 \pm 0.9\%$	CES strip/wire χ^2 Cut
$\epsilon^{\gamma}_{no\ 2^{nd}\ CES}$	$97.9 \pm 0.7 \pm 1.0\%$	No 2^{nd} CES Clusters
$\mathcal{P}^{\gamma}_{conv}$	$96.5 \pm 0.2 \pm 1.0\%$	Photon Survival
$\mathcal{S}^{cem}_{e \rightarrow \gamma}$	$100.3 \pm 0.6 \pm 1.0\%$	e *vs.* γ Shower Development
ϵ^{γ}_{cem}	$82.0 \pm 1.5 \pm 2.1\%$	Overall Photon Efficiency

Two studies with random cones thrown in the Jet-20 data sample were done. In the first study (Jet-20a), random cones of $\Delta R = 0.4$ thrown in Jet-20 events passing the above criteria were required to be more than $\Delta R = 1.1$ away from *all* jets in the event, in order to stay clear of the default $\Delta R = 0.7$ jet-cone clustering radius in use by the jet clustering algorithm. In the second study (Jet-20b), random cones of $\Delta R = 0.4$ thrown in Jet-20 events passing the above criteria were required to be more than $\Delta R = 1.1$ away from the two leading jets in the event.

The results from the Jet-20a random cone study (central cones thrown avoiding all jets in Jet-20 events) are systematically higher in efficiency by approximately 5% than that for the inclusive W/Z data samples, because the cones in the W/Z events were not required to avoid jets, while the Jet-20a cones were required to avoid all jets.

The results from the Jet-20b random cone study (central cones thrown avoiding only the two leading/trigger jets) are systematically lower in efficiency by approximately 5% than that for the inclusive W_{μ} data samples. The average number of Jets with $E_T > 5.0$ in a Jet-20 event that passes the Jet 20-b selection cuts is 1.7, while in the muon W data sets the average number of jets/event is 0.9. Thus we expect the efficiency found from Jet-20b measurement to be slightly less than from the inclusive muon W data sample.

The results obtained from random cones thrown in the Minimum Bias data have systematically somewhat higher photon efficiency than that obtained from the inclusive W/Z data samples, as anticipated. The W/Z events will have a jet recoiling from the W/Z to balance the P_T, some fraction of the random cones will overlap part or all of these jets. The Minimum Bias data set contains on average, per event, many fewer jets than the W/Z data set.

From CEM energy scale studies associated with the CDF determination of the W and Z boson masses [31, 32], the photon survival probability factor $\mathcal{P}^{\gamma}_{\overline{conv}}$ is known from the average amount of material in the inner central detector, $< \Delta T > = 4.6 \pm 0.3\%$ of a radiation length, χ^e_o ($3.6 \pm 0.2\%$ of a conversion length, χ^{γ}_o). The Baur/ISAJET/QFL $W\gamma$ and $Z\gamma$ Monte Carlo simulations provide a cross-check on $\mathcal{P}^{\gamma}_{\overline{conv}}$ by determining the fraction of $W\gamma/Z\gamma$ Monte Carlo events where the photon, had it not converted to an e^+e^- pair, would have passed all photon cuts. These two methods agree quite well, the difference between the two methods is used to define the systematic uncertainty associated with $\mathcal{P}^{\gamma}_{\overline{conv}}$. Another cross-check on $\mathcal{P}^{\gamma}_{\overline{conv}}$ was to explicitly search for isolated $\gamma \to e^+e^-$ conversion pairs with $\eta_{\gamma \to e^+e^-} < 1.1$ in each of the four data samples. No $W + (\gamma \to e^+e^-)$ or $Z + (\gamma \to e^+e^-)$ candidates were found. The photon *vs.* electron shower development correction factor $\mathcal{S}^{cem}_{e \to \gamma}$ was determined from comparing QFL photon *vs.* electron Monte Carlo simulations, and is the ratio of QFL photon to electron efficiency factor products given in the last two rows of Table 5.3.

Table 5.4 summarizes the individual CEM photon efficiencies, the photon survival probability factor, the correction factor for photon *vs.* electron EM shower development, and the overall CEM photon efficiency for the common photon selection cuts associated with the $W\gamma$ and $Z\gamma$

data samples. The statistical and systematic uncertainties associated with each quantity are also given in this table. The overall fiducial CEM photon *selection* efficiency is

$$\epsilon^{\gamma}_{cem\ sel} = 84.7 \pm 1.4\ (stat) \pm 1.8\ (syst)\%$$

The overall fiducial CEM photon efficiency, including the photon survival probability, $\mathcal{P}^{\gamma}_{\overline{conv}}$ and $e \rightarrow \gamma$ EM shower development correction factor, $\mathcal{S}^{cem}_{e \rightarrow \gamma}$ is

$$\epsilon^{\gamma}_{cem\ sel} = 82.0 \pm 1.5\ (stat) \pm 2.1\ (syst)\%$$

5.3 The $W\gamma$ and $Z\gamma$ Monte Carlo Programs

The Monte Carlo event generator used to determine the geometric and kinematic acceptances for the muons and photons, and to obtain the predictions for the number of expected $W\gamma$ and $Z\gamma$ events in the $\int \mathcal{L}_{\mu} dt = 3.54 \pm 0.24\ \mathrm{pb}^{-1}$ of muon data, was the Baur $W\gamma$ and the Baur $Z\gamma$ Monte Carlo. These same Monte Carlo's were used to determine the contribution of $W \rightarrow \tau \rightarrow \mu$ and $Z \rightarrow \tau^{+}\tau^{-} \rightarrow \mu$ to the background to the $W\gamma$ and $Z\gamma$ samples.

The Baur $W\gamma$ and $Z\gamma$ Monte Carlo programs generate weighted events using the helicity-amplitude formalism, adding together the contributions of the Feynman graphs of Figures 2.1 and 2.2 respectively. The kinematic phase space calculation is done using the VEGAS adaptive multi-dimensional integration code[33]. The Baur $W\gamma$ and $Z\gamma$ Monte Carlo programs used the most up to date structure functions (CERN PDFLIB structure functions (V3.10) [34]), and include all parton-parton luminosities and CKM[35] matrix elements. The HMRS-B structure functions were the "nominal" structure functions used in the determination of the CDF electron and muon W and Z cross sections [4] and the CDF electron and muon W/Z cross section ratios [5].

The cross section output from the Baur Monte Carlo programs includes a $K-$factor of $1 + \frac{8\pi}{9}\alpha_s(M_V^2) \simeq 1.35$, in order to account for higher order QCD processes such as $q + \bar{q} \rightarrow g + V + \gamma$ and $q + g \rightarrow q + V + \gamma$ [36]. Several other (3-graph) $W\gamma$ and $Z\gamma$ Monte Carlo event generators, such as ISAJET [37], VVJET [36], PAPAGENO [38], PYTHIA [39] and the CDF radiative W and Z decay Monte Carlo event generator, WZRAD [40] were compared, where possible, to the Standard Model results associated with the Baur $W\gamma$ and $Z\gamma$ Monte Carlo. We have also studied the systematic uncertainties associated with the Baur $W\gamma$ and $Z\gamma$ Monte Carlo results, varying the shape of the $P_T(V_\ell + \gamma)$ distribution, using several different structure function (SF) choices and studying the SF Q^2-scale dependence.

Large samples ($> 500,000$ events) of $W\gamma$ and $Z\gamma$ Baur Monte Carlo events were generated with minimal kinematic restrictions on the decay products, in order to obtain as much as possible the "total" $W\gamma$ and $Z\gamma$ cross sections. Typically $\sim$ $50K$ events pass all event selection cuts after detector simulation. The minimal kinematic restrictions were also used in order to minimize potential biasing of results from "feed-down" effects due to finite detector resolution and smearing effects. The kinematic cuts used at the Baur Monte Carlo event generator level for $W\gamma$ were $P_T^\gamma > 1.0\ GeV$, $\Delta R_{\mu-\gamma} > 0.3$, and $|\eta_\gamma| < 6.0$. There were no cuts made on P_T^μ, $\not{E}_T$, or muon/neutrino pseudo-rapidity. For $Z\gamma$, the cuts used at the event generator level were lepton $P_T^\mu > 1.0\ GeV$, $\Delta R_{\mu-\gamma} > 0.3$, $|\eta_\mu| < 6.0$, and the same photon kinematic cuts as for $W\gamma$.

The Monte Carlo event generator produces 4-vector information for each of the particles, and does not include any W or Z P_T, or event vertex information, these effects were included by post-generator processing of the Monte Carlo data sets.

Uncertainties on all derived quantities are obtained from use of additional Monte Carlo simulation of numerical results and their uncertainties.

5.4 Detector and Event Simulation used for Acceptance Determination

The geometric and kinematic acceptances for both the μ's and the γ's were determined by passing $W\gamma/Z\gamma$ events generated by the Baur Monte Carlo through detailed detector simulations. These detector simulations were extensions of the fast Monte Carlo detector simulation programs that were used for the electron and muon W and Z cross sections and W/Z cross section ratio analyses[41].

The Baur Monte Carlo event generator was run with loose kinematic cuts so that a large portion of the events produced were outside of the kinematic region of interest to this measurement. This was done to avoid any potential biasing of results that could have resulted had the kinematic cuts on the event generator been too close to the actual cuts used in this analysis. The finite resolution of the detector along with the "feed down" effect caused by the sharply falling E_T and $\Delta R_{\mu\gamma}$ spectra can introduce systematic biases if the generator kinematic cuts are too close to the analysis cuts. Since by definition the portion of $\sigma \cdot B(V_\mu + \gamma)$ of interest is that with $E_T^\gamma > 5.0$ GeV and $\Delta R_{\mu\gamma} > 0.7$, we need to find the production cross sections × decay branching ratios passing these photon cuts $\sigma \cdot B(V_\mu + \gamma)_{cuts}$ from the *generated* cross sections × decay branching ratios, $\sigma \cdot B(V_\mu + \gamma)_{gen}$.

Using[42]:

$$\mathcal{N}_{MC\ signal}^{V_\mu+\gamma} = \sigma \cdot B(V_\mu + \gamma)_{cuts} \cdot \int \mathcal{L}_\mu dt \cdot \left(A_{V_\gamma}^{\mu} \cdot \epsilon_{V_\gamma}^{\mu}\right) \tag{5.11}$$

and

$$\mathcal{N}_{MC\ signal}^{V_\mu+\gamma} = \sigma \cdot B(V_\mu + \gamma)_{gen} \cdot \int \mathcal{L}_\mu dt \cdot \left(A_{V_\gamma}^{\prime\mu} \cdot \epsilon_{V_\gamma}^{\mu}\right) \tag{5.12}$$

where the factor $A_{V_\gamma}^{\prime\mu}$ is the overall kinematic × geometrical acceptance factor for $V_\mu + \gamma$ events ($V = W$ or Z) for the *generated* $V_\mu + \gamma$ events to pass the $E_T^\gamma > 5.0\ GeV$ and $\Delta R_{\mu\gamma} > 0.7$ cuts. We obtain the general relation:

$$\sigma \cdot B(V_\mu + \gamma)_{cuts} = \sigma \cdot B(V_\mu + \gamma)_{gen} \cdot \left[\frac{A_{V_\gamma}^{\prime\mu} \cdot \epsilon_{V_\gamma}^{\mu}}{A_{V_\gamma}^{\mu} \cdot \epsilon_{V_\gamma}^{\mu}}\right] \tag{5.13}$$

For $W\gamma$:

$$\begin{aligned} \sigma \cdot B(W_\mu + \gamma)_{cuts} &= \sigma \cdot B(W_\mu + \gamma)_{gen} \cdot \left[\frac{A_{W\gamma}^{\prime\mu} \cdot \epsilon_{W\gamma}^{\mu}}{A_{W\gamma}^{\mu} \cdot \epsilon_{W\gamma}^{\mu}}\right] \\ &= \sigma \cdot B(W_\mu + \gamma)_{gen} \cdot \left[\frac{f_{W cem}^{\prime\gamma_\mu} \cdot A_{W cem}^{\prime\gamma_\mu}}{f_{W cem}^{\gamma_\mu} \cdot A_{W cem}^{\gamma_\mu}}\right] \end{aligned} \tag{5.14}$$

and:

$$\mathcal{N}_{MC\ signal}^{W_\mu\gamma} = \sigma \cdot B(W_\mu + \gamma)_{cuts} \cdot \int \mathcal{L}_\mu dt \cdot \left(A_{W\gamma}^{\mu} \cdot \epsilon_{W\gamma}^{\mu}\right) \tag{5.15}$$

For $Z\gamma$:

$$\sigma \cdot B(Z_\mu + \gamma)_{cuts} = \sigma \cdot B(Z_\mu + \gamma)_{gen} \cdot \left[\frac{A_{Z\gamma}^{\prime\mu} \cdot \epsilon_{Z\gamma}^{\mu}}{A_{Z\gamma}^{\mu} \cdot \epsilon_{Z\gamma}^{\mu}}\right] \tag{5.16}$$

where

$$A_{Z\gamma}^{\prime\mu} \cdot \epsilon_{Z\gamma}^{\mu} = \left\{A_{Zgg}^{\mu} \cdot (2 - T^\mu) \cdot \left(2\epsilon_{cent_{L_1}}^{\mu} - \epsilon_{cent_T}^{\mu}\right)\right\} \cdot \left(f_{Zgg}^{\prime\gamma_\mu} \cdot A_{Zgg}^{\prime\gamma_\mu}\right)$$

$$+ \left(A^{\mu}_{Zgs} \cdot \epsilon^{\mu}_{cent_{L_2}}\right) \cdot \left(f'^{\gamma\mu}_{Zgs} \cdot A'^{\gamma\mu}_{Zgs}\right) \tag{5.17}$$

and $A^{\mu}_{Z\gamma} \cdot \epsilon^{\mu}_{Z\gamma}$ is given by equation (5.3). The Baur Monte Carlo prediction for the number of muon $Z\gamma$ events is given by:

$$\mathcal{N}^{Z_\mu\gamma}_{MC\ signal} = \sigma \cdot B(Z_\mu + \gamma)_{cuts} \cdot \int \mathcal{L}_\mu dt \cdot \left(A^{\mu}_{Z\gamma} \cdot \epsilon^{\mu}_{Z\gamma}\right) \tag{5.18}$$

5.4.1 Details of the Fast Detector Monte Carlo

The $W\gamma$ and $Z\gamma$ events generated by the Baur Monte Carlo generator were given a random P_T boost, according to use of a "nominal" P_T distribution, based on CDF measurements of the W and Z boson P_T distributions[43].

The $Z-$vertex for the event is obtained from a gaussian distribution, of $\sigma_Z = 30\ cm$. The x-y vertex was not smeared, and was assigned to the nominal beam spot position, i.e. $x = 0, y = 0$, because the beam size $\sigma_x \simeq \sigma_y \simeq 50\mu m$. Photon energies in the central region were smeared by $\delta E_\gamma / E_\gamma = 13.5\% / \sqrt{E^\gamma_T} \oplus 2\%$. Track curvatures are smeared such that the Muon P_T's resolution is, $\delta P_T / P_T = 0.0021 P_T$

For the W's, and the Z's that have one good muon, and one muon that was not seen, the $\not{E}_T$ is modeled since it is one of the kinematic properties used to select the W-muon sample. The W P_T is balanced by recoiling jets, but only part of the jet energy is observed in the calorimeter. Some of the charged particles, those with $P_T < 400$ MeV/c that make up a jet will spiral in the magnetic field and never reach the calorimeter. Also, charged particles with $P_T < 800$ MeV/c will bend enough in the magnetic field that they will impact the calorimeter at a sufficiently large angle to defeat the projective design of the CEM and CHA calorimeter towers. In order

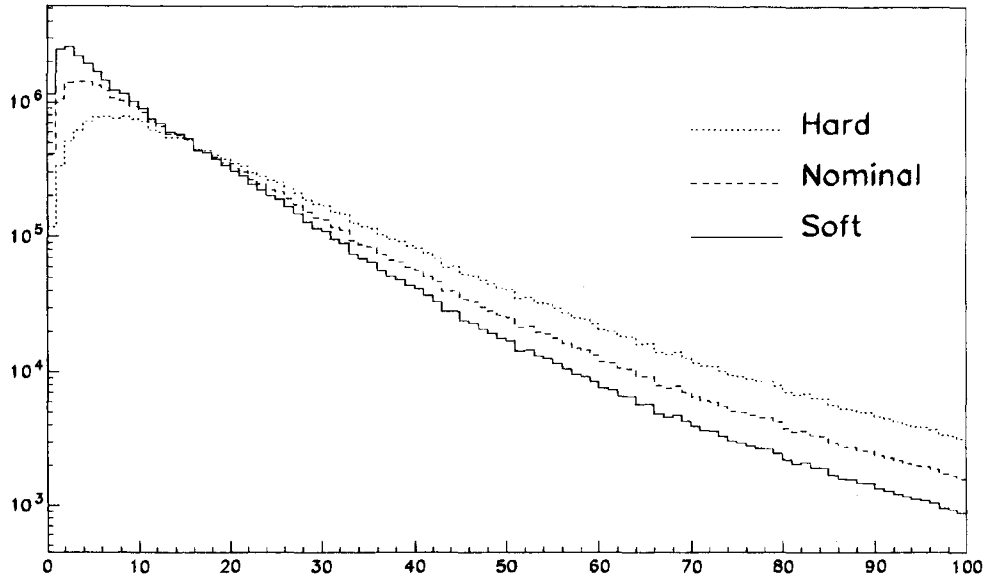

Figure 5.2: The "soft", "nominal" and "hard" W and Z P_T distributions used in the Fast Monte Carlo

to model this, the jet recoiling from the $W\gamma$ P_T is degraded a jet resolution parameterization. This degraded E_T^{jet} is then smeared with $\sigma = 0.85^{+0.3}_{-0.2}\sqrt{E_T^{jet}}$ to model the jet energy resolution of the calorimeter.

To help identify W events the neutrino is reconstructed by looking for missing transverse energy in the calorimeter, and invoking momentum conservation i.e. $E_T^{\nu} = -\Sigma \vec{E}_T^{cal} \equiv \not{E}_T$. In addition to the energy deposited by the muon, and that from the degraded recoil jet, the underlying event also contributes some E_T. An underlying event E_T is chosen from the distribution show in Figure 5.3, and smeared in the x and y direction[31]. The muon deposits on average 3 GeV in the calorimeter. Since in the real data analysis the energy deposited by the muon in the calorimeter is subtracted out, the same is done in this Monte Carlo. The sum of these contributions, with the smeared photon E_T, then gives us the calculated neutrino P_T.

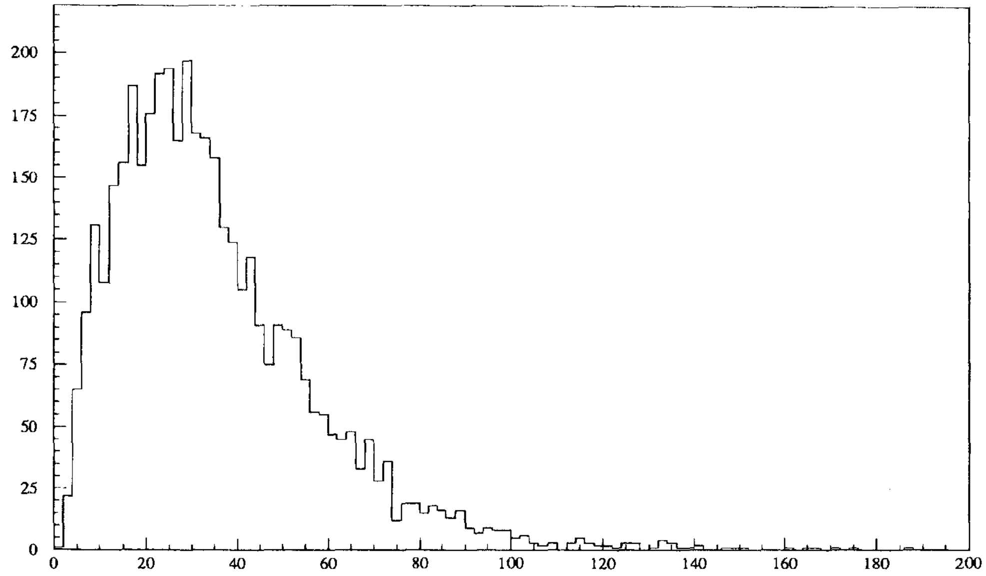

Figure 5.3: The underlying event E_T distribution used in the fast Monte Carlo to model the $\not\!\!E_T$ smearing.

The smeared muons and photons from Baur $W\gamma$ and $Z\gamma$ Monte Carlo events are propagated from the event vertex through the solenoidal magnetic field to the calorimeter. Muons are further propagated outwards to the muon chambers through the return magnetic field.

The W acceptance is fairly straight forwardly determined:

- The smeared muon passes through a fiducial region of the CMU system
- The muon has $P_T^{\mu} \geq 20\ GeV/c$
- The event has a measured $\not\!\!E_T \geq 20\ GeV$
- $|Z_{vertex}| \leq 60$ cm

then the event is accepted.

The Z acceptance is more complicated because there are 2 muons to be accounted for. The most restrictive class of these events is one where both muons from the Z decay pass through the fiducial CMU region. Even if one of the muons fails to fire the Level 2 high P_T muon trigger, there is still a chance than the second muon will fire the Level 2 trigger.

If only one muon passes though the fiducial CMU region, and the other muon is at low ,enough $|\eta|$ that it leaves a track in the CTC, there is only one muon that has a chance to fire the Level 2 muon trigger. If one of the muons passes through the CMU fiducial region, and the other is not observed, then this class of events can be mis-identified as a W event. The unseen muon carries off P_T, and since it is a minimum ionizing particle, it will not deposit much of its energy in the calorimeter. Thus, it can fake a neutrino, and the event may pass the $\not{E}_T$ requirement for W events. This will be further examined when backgrounds are discussed.

If both muons from the Z are detected, then a cut on the invariant mass of the pair is made, requiring $65 \leq M_{\mu\mu} \leq 115$.

The photon acceptance is quite simply determined, each smeared photon that is produced by the Baur Monte Carlo is propagated to the CEM, and if:

- the photon is in a fiducial region of the CEM,
- the photon has a smeared $E_T > 5\ GeV$,
- the ΔR separation between the smeared muon(s) and the smeared photon is > 0.7,

then the photon is accepted.

5.5 The QFL Monte Carlo

A second method of determining the predicted number of $W\gamma$ and $Z\gamma$ events was used as a cross check of the fast Monte Carlo. A more detailed, full detector simulation of $W\gamma$ and $Z\gamma$ Monte Carlo data including the QCD fragmentation of the underlying event and associated jets,

Table 5.5: Photon Fractions and Acceptances for $\mu\ \sigma \cdot B(W+\gamma)_{cuts}$ and $\sigma \cdot B(W+\gamma)_{gen}$ The statistical uncertainty associated with each quantity is given.

$W\gamma$	Cuts	Generated
$f^{\gamma\mu}_{Wcem}$	$50.9 \pm 0.5\%$	$46.8 \pm 0.1\%$
$A^{\gamma\mu}_{Wcem}$	$75.7 \pm 0.3\%$	$13.1 \pm 0.2\%$

Table 5.6: Photon Fractions and Acceptances for $\mu\ \sigma \cdot B(Z+\gamma)_{cuts}$ and $\mu\ \sigma \cdot B(Z+\gamma)_{gen}$. The statistical uncertainty associated with each quantity is given.

$Z\gamma$	Cuts	Generated
$f^{\gamma\mu}_{Zgg}$	$72.6 \pm 0.7\%$	$75.5 \pm 0.3\%$
$f^{\gamma\mu}_{Zgs}$	$68.4 \pm 0.5\%$	$71.5 \pm 0.2\%$
$A^{\gamma\mu}_{Zgg}$	$74.8 \pm 0.5\%$	$18.7 \pm 0.3\%$
$A^{\gamma\mu}_{Zgs}$	$75.7 \pm 0.4\%$	$19.4 \pm 0.2\%$

Table 5.7: Overall Acceptances × Efficiency Factors for $\mu\ W\gamma/Z\gamma$.

Acceptance × Efficiency Factor	Muon
$A^{\mu}_{W\gamma} \cdot \epsilon^{\mu}_{W\gamma}$	$3.7 \pm 0.2\%$
$A^{\mu}_{Z\gamma} \cdot \epsilon^{\mu}_{Z\gamma}$	$4.0 \pm 0.2\%$

using the ISAJET[37] generator and the "QFL" CDF detector simulation was used. The same output from the Baur $W\gamma$ and $Z\gamma$ Monte Carlo event generator as was used in the fast Monte Carlo was used as input to this detector simulation. First, however, the distributions were unweighted according to the procedure described in CDF-1665[44]. This unweighted Monte Carlo data set is then passed through QFL detector simulation and then through the offline event reconstruction. The QFL muon $W\gamma$ and $Z\gamma$ events are then passed through the same analysis as the CDF inclusive muon W and Z data samples.

5.5.1 Predictions of $\mathcal{N}^{W_\mu\gamma}_{MC\ signal}$ and $\mathcal{N}^{Z_\mu\gamma}_{MC\ signal}$

Predictions of $\mathcal{N}^{W_\mu\gamma}_{MC\ signal}$ and $\mathcal{N}^{Z_\mu\gamma}_{MC\ signal}$ are listed in Table 5.8. For the $Z\gamma$ case the contribution from Drell-Yan (DY) + $Z\gamma$ are explicitly listed. These results were also obtained with

Table 5.8: Predicted Number of SM Signal Events for Muon $W\gamma$ & $Z\gamma$. The statistical uncertainty associated with each quantity is given.

	Muon
Baur Fast $W\gamma$ MC	2.54 ± 0.24
Baur QFL $W\gamma$ MC	2.41 ± 0.32
Baur Fast $Z\gamma$ MC	0.67 ± 0.07
Baur Fast $Z + DY\gamma$ MC	0.68 ± 0.06
Baur QFL $Z\gamma$ MC	0.68 ± 0.11

the use of the Baur $Z\gamma$ Monte Carlo program and fast detector simulation programs. The DY contribution can be seen to be small, but we explicitly correct for it in the F_{DY} term, as shown in Table 5.1.

Chapter 6

Determination of Photon Backgrounds

The most significant photon background in the $W\gamma$ and $Z\gamma$ samples is due to a combination of QCD jets that are mis-identified as photons, and prompt isolated photons due to initial/final-state radiation (quark QED bremsstrahlung). Strictly speaking, this initial/final-state radiation is *not a background* since these processes are included in the theory calculations for the $W\gamma/Z\gamma$ signal. The "K-factor" of 1.35 included in the Baur $W\gamma/Z\gamma$ event generator is included to adjust for the contributions of final-state radiation from higher order QCD processes such as $q + g \rightarrow q + W/Z + \gamma$.

6.1 QCD Photon Background

In order to arrive at an estimate of the QCD jet background, we would like to have a pure sample of jets that had the same composition and kinematics as the jets in the inclusive W and Z samples. The Jet-20 sample is used as an independent source of jets for this background determination. The Jet-20 sample was formed using a trigger operating concurrently with the muon-trigger, which accepted 1 out of 300 events that had at least one jet with $E_T \geq 20\ GeV$. The high E_T trigger jets in this data sample have significant trigger biases associated with calorimeter energy response at the trigger threshold, and as such can't be used as part of the background jet sample. We therefore further select Jet-20 events that had at least one central jet, with another jet in the central or plug region that has $E_T^J > 15\ GeV$, and that these two "Selection jets" have a pair mass of $M_{JJ} > 40\ GeV$.

Then all the additional, non-leading central ($|\eta| < 1.1$) jets, known as "Extra jets" are used for QCD jet background studies. These are the same requirements made on the Jet-20 samples used to determine photon efficiencies, see Section 5.2 and Appendix B for further details. Most of the Jet-20 data are di-jet type events, so constraining the two-jet invariant mass distribution of the leading two jets to approximately that of the W or Z mass gives us a set of "Extra jets" (jets that are not either of the two Selection jets used to select the event) that are similar to the jets in W+jets and Z+jets data. These Extra jets are required to be central ($|\eta_j| < 1.1$), to have $\Delta R > 1.4$ from either of the Selection jets, and $E_T^{Jet} > 5.0$ GeV. The separation between the Selection jets and the Extra jets of $\Delta R > 1.4$ is used in order to prevent the jet clustering cones, each $\Delta R = 0.7$, from overlapping. These selection requirements give a sample which has approximately the same $\sqrt{\hat{s}}$ as that for the inclusive muon W and Z data samples. A total of 11726 Extra jets passed these cuts.

The Jet-20 Extra jet sample is used to find the probability that a Jet will fragment into something that is (mis-)identified as a photon, by applying the same photon event selection criteria to the Jet-20 data as was used for the inclusive W/Z data samples. This fragmentation probability as a function of E_T can then be applied to the jets in the W and Z samples, to

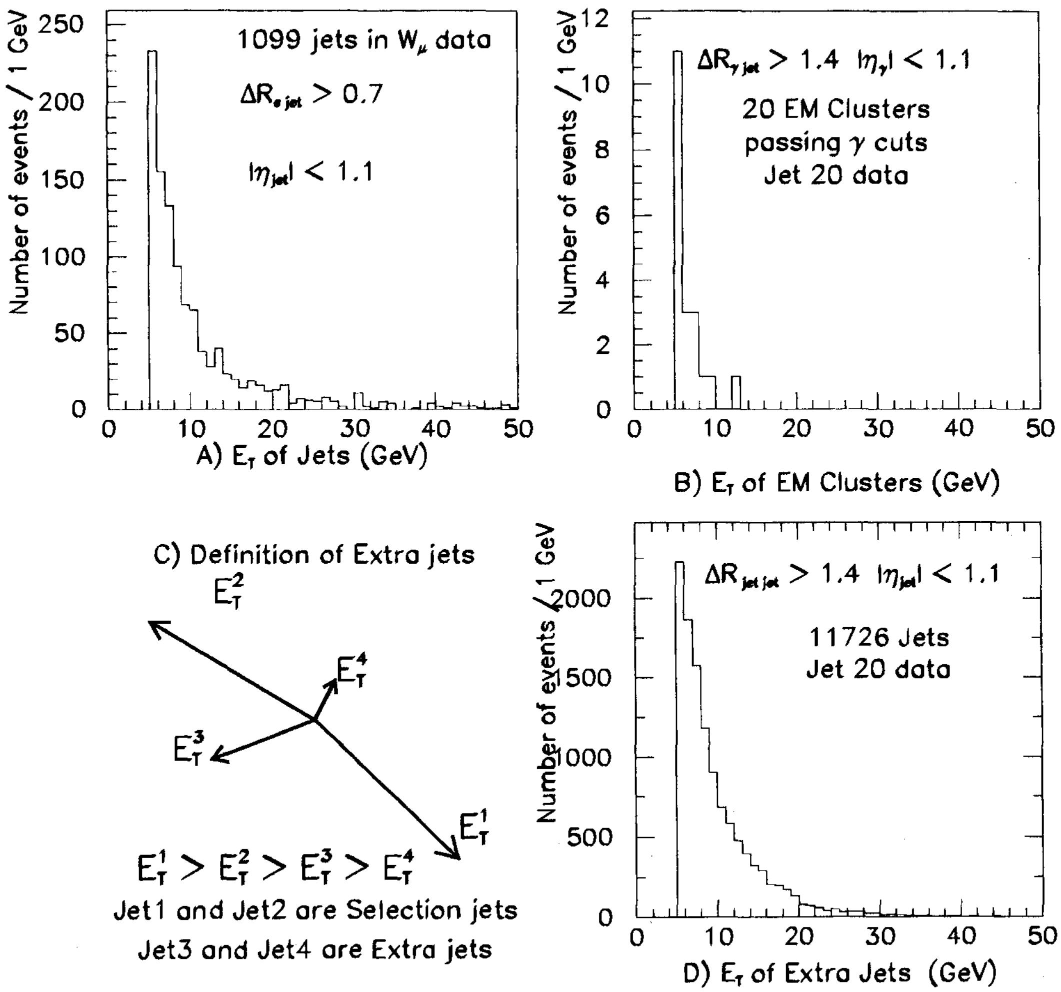

Figure 6.1: Inclusive QCD jet background for the muon $W\gamma$ data sample. A) Jet E_T for jets in the inclusive muon W data sample B) E_T of central fiducial EM clusters in the Jet-20 sample, passing all photon cuts C) Vector diagram illustrating "Selection jets" and "Extra jets" in the Jet-20 inclusive data sample. D) "Extra jets" E_T in the Jet-20 inclusive data sample.

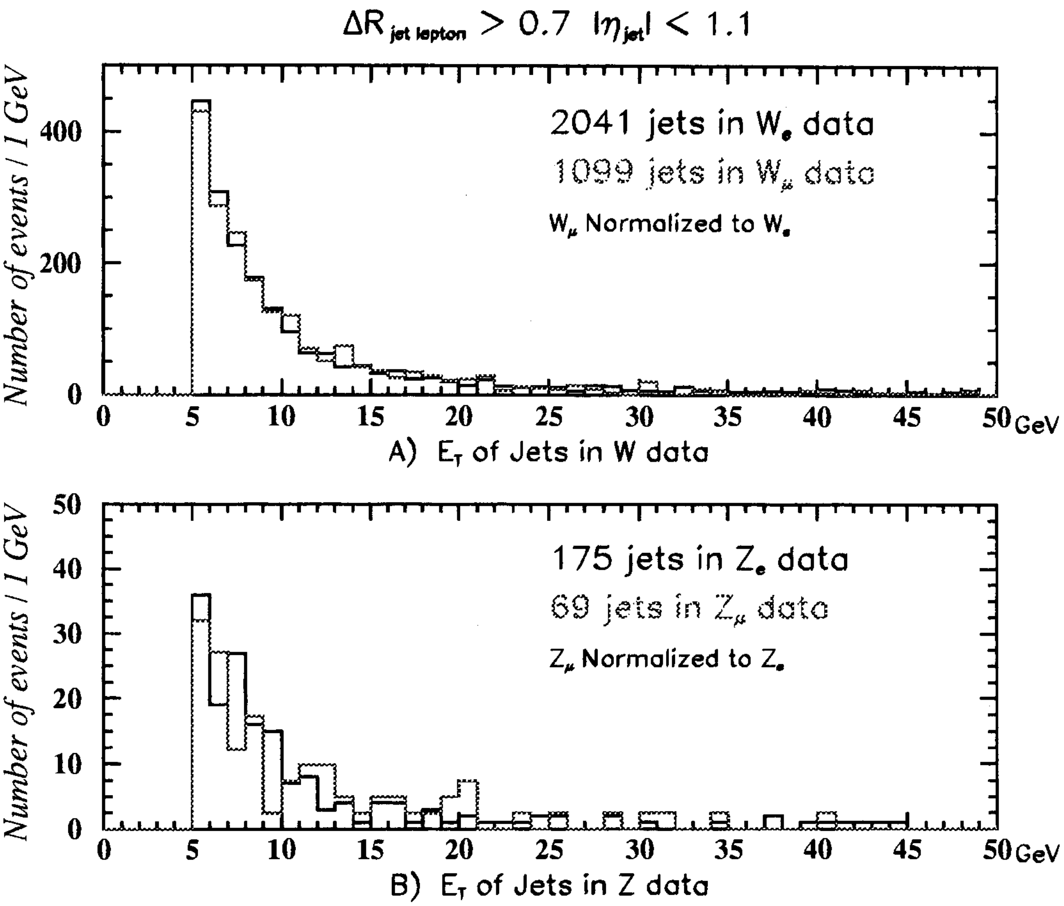

Figure 6.2: (A) Central jet E_T^{Jet} for inclusive W electron data sample, with central jet E_T^{Jet} for the inclusive W muon data sample overlaid on the plot. (B) central jet E_T^{Jet} for inclusive Z electron data sample, with central jet E_T^{Jet} for the inclusive Z muon data sample overlaid on the plot. In both cases, the muon sample distribution have been normalized to the electron sample distribution.

arrive at an estimate of the QCD background in the W/Z samples. Figure 6.2 shows that the shape of the central jet E_T spectra for each of the muon vs. electron W (and Z) data samples are in good agreement.

By using the *inclusive* W/Z+Jets data samples, the *inclusive* QCD jet background for each of the channels will automatically be taken into account. For example, the inclusive $W+$ QCD jet background for the $W\gamma$ data samples consists of a contribution from "direct" W+Jet background, with *additional* QCD jet background contributions from mis-identified Z+Jet events, where one of the Z decay muons is not detected, but the event satisfies the $W\gamma$

event selection criteria, and $(W \rightarrow \tau\ \bar{\nu}_\tau)$+Jet events, where $\tau \rightarrow \mu\ \bar{\nu}_\mu\ \nu_\tau$, again satisfying the $W\gamma$ event selection criteria.

Obviously the assumption is made that the QCD jet mis-identification probability distributions are the same in both the Jet-20 Extra jet data sample and the inclusive W/Z data samples, for the E_T range of interest, i.e.

$$\mathcal{P}^{Jet\ 20}_{Jet \rightarrow \text{``}\gamma\text{''}}(E_T) \ = \ \mathcal{P}^{W_\ell/Z_\ell}_{Jet \rightarrow \text{``}\gamma\text{''}}(E_T) \tag{6.1}$$

This assumption was tested by comparing the QCD jet mis-identification probability measured from the Jet-20 with that found from the combined $e + \mu$ inclusive W data samples. We have *assumed* that the $W\gamma$ signal is the Standard Model prediction, and subtracted it from the numerator of Equation (6.3). For each E_T bin;

$$\mathcal{P}^{Jet-20}_{Jet \rightarrow \text{``}\gamma\text{''}}(i) \ \equiv \ \left[\frac{N_i^{\text{``}\gamma\text{''}\ Jet-20}}{N_i^{Extra\ jet\ \ Jet-20}}\right] \tag{6.2}$$

$$\mathcal{P}^{W_e/W_\mu}_{Jet \rightarrow \text{``}\gamma\text{''}}(i) \ \equiv \ \left[\frac{N_i^{\text{``}\gamma\text{''}\ V_\ell} - N_i^{SM\ signal\ V_\ell}}{N_i^{Extra\ jet\ \ V_\ell}}\right] \tag{6.3}$$

The Jet-20 data sample has 20 events that pass all photon cuts (See Table 4.4). The combined $\mu + e$ W data sample has 13 events, with 7.1 ± 0.7 events predicted by the SM. Table 6.5 summarizes these results. If instead of assuming the SM prediction for the $W\gamma$ signal, we subtract the non-SM prediction at our experimental 95% CL upper limits on $\Delta\kappa$ and λ, within the range $5 \ < \ E_T \ < \ 15\ GeV$, the fractional change in the combined $e + \mu$ QCD jet mis-identification probability distribution in this E_T range is $\sim \pm 25\%$, which is well within the statistical uncertainties.

Table 6.1: QCD Jet Mis-Identification Probability – Loose Photon Cuts, and with All Photon Cuts. The statistical uncertainty associated with each quantity is given.

E_T Range (GeV)	$\mathcal{P}^{J20}_{Jet\rightarrow``\gamma"}$ Loose	$\mathcal{P}^{W_{e+\mu}}_{Jet\rightarrow``\gamma"}$ Loose	$\mathcal{P}^{J20}_{Jet\rightarrow``\gamma"}$ All-cuts	$\mathcal{P}^{W_{e+\mu}}_{Jet\rightarrow``\gamma"}$ All-cuts
5 – 6	$1.35 \pm 0.27\%$	$0.97 \pm 0.53\%$	$0.49 \pm 0.15\%$	$0.41 \pm 0.29\%$
6 – 8	$0.76 \pm 0.16\%$	$0.97 \pm 0.48\%$	$0.17 \pm 0.07\%$	$0.15 \pm 0.21\%$
8 – 11	$0.18 \pm 0.10\%$	$0.19 \pm 0.40\%$	$0.07 \pm 0.05\%$	$-0.10 \pm 0.16\%$
11 – 15	$0.17 \pm 0.13\%$	$1.04 \pm 0.87\%$	$0.06 \pm 0.06\%$	$0.58 \pm 0.53\%$
$>$ 15	$0.00^{+0.07}_{-0.00}\ \%$	$0.07 \pm 0.21\%$	$0.00^{+0.08}_{-0.00}\ \%$	$0.09 \pm 0.21\%$
$>$ 5	$0.55 \pm 0.07\%$	$0.57 \pm 0.11\%$	$0.17 \pm 0.04\%$	$0.19 \pm 0.11\%$

If the comparison is repeated using loose photon cuts, i.e. require only isolated fiducial CEM electromagnetic clusters by imposing only the $ET4 < 2\ GeV$ and PT4 $<$ 2 GeV cuts, 64 events are found from the Jet-20 data sample, and 26 events from the combined $e + \mu$ W data sample. The expected SM $W\gamma$ signal passing these cuts is 8.8 ± 0.8 events. Thus any deviation of the $W\gamma$ signal from the SM value has $\sim \frac{1}{3}$ as much effect on the result as in the previous comparison. Table 6.1 summarizes these results. The agreement between the two QCD Jet mis-identification probability distributions is reasonably good. Thus we expect that the QCD jet mis-identification probability is similar to the jet mis-identification probability in the inclusive W/Z data sample, i.e. Equation 6.1 holds.

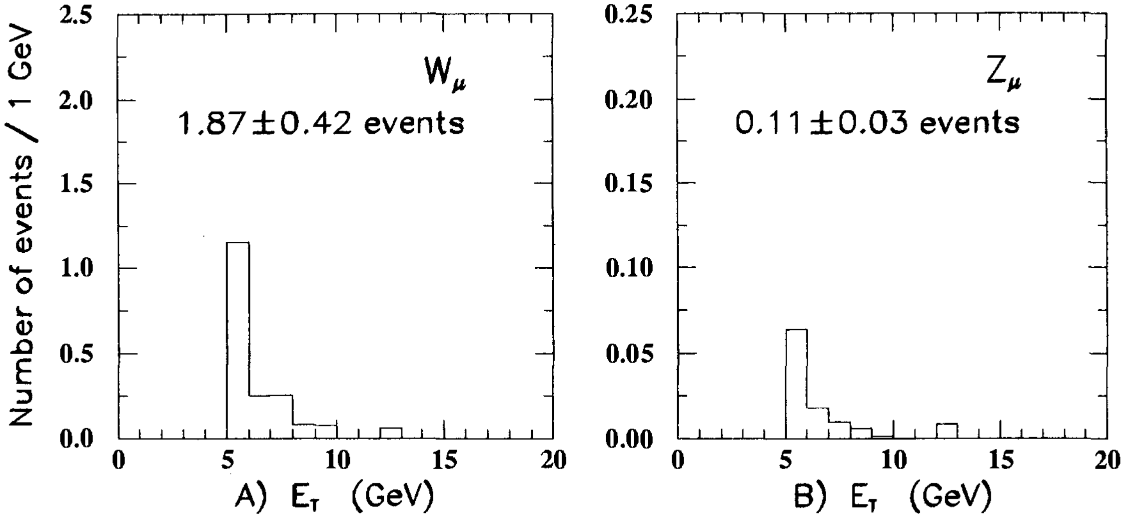

Figure 6.3: The predicted inclusive QCD photon backgrounds in the muon W and Z channel.

The predicted number of QCD-background events in the $W\gamma$ and $Z\gamma$ samples (See Figure 6.3) is then calculated by applying the QCD jet mis-identification probability as a function of E_T (the third column of Table 6.1) to the E_T spectrum of jets in the $W\gamma/Z\gamma$ that are central, $E_T > 5\ GeV$, and have $\Delta R_{\mu j} > 0.7$, see Figure 6.2. There are 1099 jets in the muon W, and 69 jets in the muon Z samples that satisfy these requirements.

$$N^{Jet\ W_\mu}_{Bkgnd} = \sum_i N_i^{Jet\ W_\mu}(\Delta R_{\mu-J} > 0.7) \times \left(\frac{N_i^{\text{``}\gamma\text{''}-J20}(\Delta R_{Selection\ Jet-EM\ clst} > 1.4)}{N_i^{Extra\ jet\ J20}(\Delta R_{Selection\ Jet-Extra\ jet} > 1.4)} \right)$$

$$N^{Jet\ Z_\mu}_{Bkgnd} = \sum_i N_i^{Jet\ Z_\mu}(\Delta R_{\mu-J} > 0.7) \times \left(\frac{N_i^{\text{``}\gamma\text{''}\ J20}(\Delta R_{Selection\ Jet-EM\ clst} > 1.4)}{N_i^{Extra\ jet\ J20}(\Delta R_{Selection\ Jet-Extra\ jet} > 1.4)} \right)$$

Figure 6.3 shows the predicted inclusive QCD photon background in each of the muon data samples as a function of E_T. Note that the QCD jet background distribution is sharply peaked at the $E_T^\gamma > 5$ GeV threshold for both of the data samples.

Table 6.2: Predicted Number of Inclusive QCD Jet Background Events for Muon $W\gamma$ & $Z\gamma$. The statistical uncertainty associated with each quantity is given.

Channel	Standard Method Corrected Jets	Summed Method Corrected Jets	Standard Method Uncorrected Jets	Summed Method Uncorrected Jets
$e\ W\gamma$:	3.57 ± 0.81	3.48 ± 0.87	2.92 ± 0.67	3.42 ± 0.85
$\mu\ W\gamma$:	1.87 ± 0.42	1.87 ± 0.46	1.48 ± 0.34	1.86 ± 0.46
$e\ Z\gamma$:	0.30 ± 0.07	0.30 ± 0.07	0.28 ± 0.07	0.30 ± 0.07
$\mu\ Z\gamma$:	0.11 ± 0.03	0.12 ± 0.03	0.07 ± 0.02	0.12 ± 0.03

The E_T bins intervals of Table 6.1 are used, and the above method using corrected jet energies as our standard inclusive QCD jet background determination. The systematic uncertainties associated with the choice of binning and the use of corrected vs. uncorrected jet energies have also been investigated. In addition to our standard method, we also calculate the predicted background using only one bin, $E_T > 5.0\ GeV$, and also repeat the calculations using un-corrected jets. The two choices of binning and the two choices of (un-)corrected jets yields 4 background measurements which are listed in Table 6.2.

An independent cross check on the level of direct QCD jet background in the $W\gamma$ and $Z\gamma$ samples was obtained from Monte Carlo simulations of inclusive W/Z+Jets using the VECBOS W/Z+n Jets ($n = 0 - 2$) Monte Carlo event generator with the HERWIG Monte Carlo to generate the underlying event and to fragment the jets recoiling against the W/Z boson, and using the QFL Monte Carlo for CDF detector simulation. These simulated events were passed through the same set of $W\gamma/Z\gamma$ event selection cuts to get Monte Carlo predictions for the level of direct QCD jet background in each of the data samples.

Figure 6.4 shows the VECBOS/HERWIG/QFL Monte Carlo predictions for the E_T spectrum of the $V + nJets$ QCD background in our data samples.

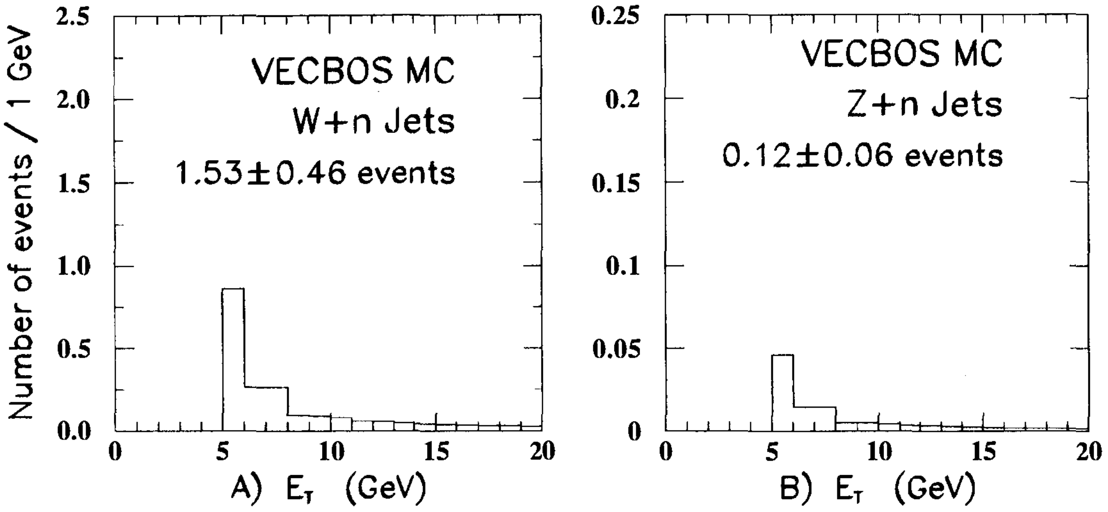

Figure 6.4: The VECBOS/HERWIG/QFL Monte Carlo background prediction for muon channel W + n Jets and Z + n Jets. Plot A) is the muon W $E_T^{background}$ and B) is the muon Z $E_T^{background}$.

The inclusive and Monte Carol derived direct QCD jet background obtained via these two methods are summarized in Table 6.3. The uncertainties quoted in this table are statistical only, the systematic uncertainties associated with the QCD jet background are discussed below in Section 7.1.

6.2 Other Sources of Background in the $W\gamma$ and $Z\gamma$ Data Samples

Inclusive Z + Jet and $Z\gamma$ contribute to $W\gamma$ background in the muon channel, when one of the leptons from the $Z-$decay is not detected, resulting in the Z being mis-identified as a W. The process $(W \rightarrow \tau\nu_\tau) + \gamma$ and $(W \rightarrow \tau\nu_\tau)$ + Jet also contributes to the background in the muon $W\gamma$ data samples when the τ decays to a muon.

6.2.1 $Z\gamma$ Backgrounds to the $W\gamma$ Signal

For $W\gamma$ candidate events, contamination from one-legged $Z\gamma$ and $Z + Jet \rightarrow$ "$Z + \gamma$" events is suppressed by making the following requirements:

If there exists a track in the event, other than the one associated with the muon that is reconstructed, then if the track satisfies

- track $P_T > 10\ GeV/c$,
- the track extrapolates to a minimum ionizing cluster,
- the pair mass of this track with the track associated with the reconstructed muon is $65 < M_{\mu\ Track} < 115$,

the event is rejected as a one-legged $Z\gamma$ candidate. From studies using QFL $W\gamma$ Monte Carlo simulated data for muons, no signal events, $0^{+0.41}_{-0.00}$ in $3.54 \pm 0.24\ \ \mathrm{pb}^{-1}$ are lost by these 2^{nd} track-type cuts. After making these cuts, (0.36 ± 0.06) $Z\gamma$ and (0.04 ± 0.01) $Z+$ Jet background events are expected to remain in the $W\gamma$ data sample. Since the inclusive $Z+$ Jet event sample was used in the inclusive QCD background determination, the $Z+$ Jet background is already accounted for. Two 1-legged $Z\gamma$ candidates were found in the muon $W\gamma$ sample, while from the Fast Monte Carlo $\simeq 0.7$ events are expected without imposing the 2^{nd} leg cut. These results are summarized in the Table 6.4.

6.2.2 τ Backgrounds

In any of the signal processes as well as the background processes, the W or Z boson can decay to tau(s) which then decays to a muon, rather than decaying directly to muon(s). The combination of an additional tau branching ratio factor, $B(\tau \rightarrow \ell\ \bar{\nu}_\ell\ \nu_\tau) \ \simeq\ 17.8\%$, and the softer muon E_T and $\not{E}_T$ spectrum due to the 3 body decay, these tau background processes will be greatly suppressed.

The backgrounds from $(W \rightarrow \tau\nu_\tau) + \gamma$ and $(W \rightarrow \tau\nu_\tau) + \mathrm{Jet}$ were found by forcing the W generated by the Baur Monte Carlo to decay like $W \rightarrow \nu_\tau(\tau \rightarrow \mu\nu_\mu\nu_\tau)$. The same procedure used to determine the $W\gamma$ Monte Carlo signal was used here to find the tau background contribution. The tau decay contribution to the $W\gamma$ background was found to be small, and is tabulated in Table 6.4. The background to $Z\gamma$ from $(Z \rightarrow \tau\tau) + \gamma$ where both $\tau \rightarrow \mu\nu_\mu\nu_\tau$ was found to be extremely small, ($<<$ 0.1event), so it was neglected. Likewise the background to $W\gamma$ from the same process where one of the taus decays to a muon that is not reconstructed is very small. The $Z \rightarrow \tau\tau + Jet$ QCD backgrounds to both $Z\gamma$ and $W\gamma$ are also very small, and are neglected.

6.3 Summary of Backgrounds in the $W\gamma$ and $Z\gamma$ Samples

The inclusive QCD jet backgrounds for each of the data samples are summarized in Table 6.3 and the non-QCD backgrounds are listed in Table 6.4. The observed number of events, the total background, the experimentally determined number of signal events, and the Standard Model predicted number of signal events in each of the data samples are summarized in Table 6.5.

Table 6.3: QCD Jet Backgrounds for μ $W\gamma$ and $Z\gamma$. The statistical uncertainty associated with each quantity is given.

QCD Background	Muon
$W\gamma$: Inclusive $W + Jets$ Data	1.87 ± 0.42
$W\gamma$: VECBOS $W + nJets$ MC	1.53 ± 0.46
$W\gamma$: $Z + Jet \to$ "W" + "γ"	0.04 ± 0.01
$W\gamma$: $W^{\tau\to\ell} + Jet \to W^{\tau\to\ell}$ + "γ"	0.04 ± 0.01
$W\gamma$: VECBOS + $(Z + Jet)$ + $(W^{\tau\to\ell} + Jet)$	1.61 ± 0.46
$Z\gamma$: Inclusive $Z + Jets$ Data	0.11 ± 0.03
$Z\gamma$: VECBOS $Z + nJets$ MC	0.12 ± 0.06

Table 6.4: Non-QCD Backgrounds to Muon $W\gamma$. The statistical uncertainty associated with each quantity is given.

Background Process	Muon
$Z + \gamma \to$ "W" $+ \gamma$	0.36 ± 0.06
$W^{\tau\to\ell} + \gamma$	0.06 ± 0.01

Table 6.5: Summary of $W\gamma$ and $Z\gamma$ Results. The number of: observed events $N_{observed}$; predicted total background events $\Sigma N_{background}$; signal events $N_{signal} = N_{observed} - \Sigma N_{background}$ and predicted SM signal events, N_{pred}^{SM} for each channel.

Channel	$N_{observed}$	$\Sigma N_{background}$ $(stat + syst)$	N_{signal} $(stat + syst)$	N_{pred}^{SM} $(stat)$
e $W\gamma$	8	$3.8 \pm 0.8 \pm 1.1$	$4.2 \pm 2.9 \pm 1.1$	4.6 ± 0.4
μ $W\gamma$	5	$2.3 \pm 0.4 \pm 0.6$	$2.7 \pm 2.3 \pm 0.6$	2.5 ± 0.2
e $Z\gamma$	2	$0.3 \pm 0.1 \pm 0.1$	$1.7 \pm 1.4 \pm 0.1$	1.2 ± 0.1
μ $Z\gamma$	2	$0.1 \pm 0.1 \pm 0.1$	$1.9 \pm 1.4 \pm 0.1$	0.7 ± 0.1

Chapter 7

Systematic Uncertainties

In addition to the systematic uncertainty associated with the QCD background measurement, there are also systematic effects due to the $P_T(V_\mu + \gamma)$ distribution used in the Baur Monte Carlos, the Structure Function (SF) choice, and the Q^2 scale dependence for the nominal Structure Function (HMRS-B). The systematic effect of varying the CEM energy scale and CEM energy resolution was also investigated. The systematic uncertainties associated with each of the afore mentioned variables and their effects on the determination of $\sigma \cdot BR(V_\mu + \gamma)$ was studied. The overall systematic uncertainties on the cross sections are small in comparison to the statistical uncertainties.

7.1 QCD Background

The systematic uncertainties associated with the QCD background measurement listed in the Tables 6.3, 6.4, 6.5 are defined as the quadratic sum of:

- The maximum difference between the four methods (two E_T binning $\otimes$ two (un-)corrected Jet energies) used to determine the inclusive QCD jet backgrounds,

- The difference between the inclusive QCD jet background as determined from the Jet-20 data set, and the sum of the "direct" QCD jet background as determined from the VECBOS/HERWIG/QFL $W/Z + jets$ Monte Carlo simulations, and the "indirect" QCD jet background, i.e. for $W\gamma$ the "indirect" QCD backgrounds are due to $Z+$ Jet and tau channel $W+$ Jet, while for $Z\gamma$ the "indirect" QCD background would be tau channel $Z+$ Jet, which is very small and has been neglected.

The systematic uncertainties associated with the background measurement are kept separate from the other systematic uncertainties, as the uncertainty due to the background measurement is not correlated with systematic effects due to the use of the Baur Monte Carlo for both the experimental (determination of kinematic and geometric acceptances) and Monte Carlo prediction of cross sections.

7.2 P_T of $(W/Z + \gamma)$

Since we do not have a experimental measurement of the diboson $P_T(V + \gamma)$ spectrum, and no theoretical predictions for these distributions in the region $P_T(V + \gamma) <\sim 10\ GeV/c$, we use the measured CDF $P_T(W/Z)$ distributions [43] as an approximation. The measured $d\sigma/dP_T(W/Z)$ distributions are in good agreement with theoretical predictions [45] for inclusive W/Z. The shape of the $P_T(W/Z + \gamma)$ distributions are expected to be very similar to $P_T(W/Z)$ for the $W\gamma/Z\gamma$ event selection used in this analysis. The systematic effects of varying the shape of the assumed $P_T(V + \gamma)$ distribution on the W/Z/photon acceptances, Monte Carlo predicted cross sections, Monte Carlo expected number of events and the experimental cross section results were studied.

For both $W\gamma$ and $Z\gamma$ the $P_T(W/Z + \gamma)$ distributions used in the Monte Carlo event were varied by $\pm 1\sigma$ on the fit to the $d\sigma/dP_T(W/Z)$ distribution. The fast Monte Carlo was run to obtain all kinematic and geometrical acceptances, to obtain $\sigma \cdot BR(V_\ell + \gamma)_{cuts}$. These acceptances found for each of the three $P_T(W/Z + \gamma)$ distribution were then used in conjunction with the event and photon selection efficiencies to obtain $\sigma \cdot BR(V_\ell + \gamma)_{exp}$ for each channel.

7.3 Structure Function (Q^2 scale)

The systematic uncertainties associated with the Q^2-scale dependence of the nominal Structure Function choice (HMRS-B) used in the Monte Carlo, were studied by varying the Q^2-scale in the range $\frac{1}{4}M^2_{V+\gamma} < Q^2 < 4M^2_{V+\gamma}$, for each of the decay channels. Correlations between Q^2-scale dependence and the diboson $P_T(V_\ell + \gamma)$ distribution are neglected, even though they are in principle correlated with each other due to four-momentum conservation in the $V_\ell + \gamma$ production process. Ignoring the correlations between the Q^2-scale and the diboson $P_T(V_\ell + \gamma)$ distribution conservatively over-estimates the systematic uncertainty associated with these effects.

7.4 Structure Function Choice

The systematic uncertainties associated with the choice of structure functions for each of the decay channels was investigated using five different structure function (SF) choices (DFLM-260 [46], MRS-B [47], HMRS-B [48], MRS-S0 [49] and MT-B1 [50]). The Baur $W\gamma$ and $Z\gamma$ Monte Carlo events were analyzed using the fast Monte Carlo detector simulation programs to obtain Monte Carlo $\sigma \cdot B(V_\mu + \gamma)_{cuts}$ and kinematic/geometrical acceptance results.

7.5 CEM Energy Scale and Energy Resolution

The CEM calorimeter was calibrated using inclusive electrons in Energy/Track-momentum (E/P) studies for the low energy region ($> 5\ GeV$). The high energy region, $\sim\leq 40\ GeV$ was calibrated using W decay electrons. The error on these energy scale calibrations is about $\sim$ 1.0% for the low energy region, and 0.24% for the high energy region [31]. This level of uncertainty has a negligible impact on the observed or predicted number of $W\gamma/Z\gamma$ events, and the Monte Carlo predicted and experimental cross sections.

Similarly, the effect of $\pm 1\sigma$ variations of the stochastic and constant terms associated with the CEM calorimeter energy resolution,

$$\delta E/E \;=\; (13.5 \pm 1.5)\%/\sqrt{E_T} \;\oplus\; (2.0 \pm 0.3)\% \quad (E \text{ in GeV}) \tag{7.1}$$

also have negligible impact on the observed or predicted number of $W\gamma/Z\gamma$ events and the Monte Carlo predicted and experimental cross sections for $E_T^{\gamma} > 5.0$ GeV.

7.6 Correlations Between the Systematic Uncertainties

The systematic uncertainties associated with varying the $P_T(V_\mu + \gamma)$ distributions, the Q^2 scale dependence, and the SF choice for the Monte Carlo and the experiment are correlated because the fast Monte Carlo is used to determine the geometric and kinematic acceptance factors, which are then used in determining the experimental $\sigma \cdot BR(V_\mu + \gamma)$. When simply quoting experimental and Monte Carlo $\sigma \cdot BR(V_\mu + \gamma)$ results, the respective contributions from QCD background subtraction, $P_T(V_\mu + \gamma)$, Q^2 scale dependence, and SF choice are included in the overall uncertainty.

Table 7.1: Summary of $P_T \oplus Q^2 \oplus SF$ Systematic Uncertainties. The $+1\sigma$ and -1σ quadrature sum of systematic uncertainties associated with variations of the $P_T(V+\gamma)$ distribution, Q^2-scale dependence and structure function choice for the Monte Carlo $\sigma \cdot B(V\gamma)$ prediction (only), experimental $\sigma \cdot B(V\gamma)$ results (only), and the correlated Monte Carlo – experiment $\sigma \cdot B(V\gamma)$ difference are given.

Channel	$\Delta\sigma \cdot B(V\gamma)_{MC}$ (pb)	$\Delta\sigma \cdot B(V\gamma)_{Expt}$ (pb)	$\Delta\sigma \cdot B(V\gamma)_{MC-Expt}$ (pb)
$e\ W\gamma$	$^{+4.1}_{-1.2}$	$^{+1.5}_{-1.0}$	$^{+2.9}_{-0.5}$
$\mu\ W\gamma$	$^{+3.3}_{-0.9}$	$^{+2.2}_{-0.8}$	$^{+2.5}_{-1.3}$
$e+\mu\ W\gamma$	$^{+3.3}_{-0.9}$	$^{+1.7}_{-0.9}$	$^{+2.3}_{-1.3}$
$e\ Z\gamma$	$^{+0.5}_{-0.2}$	$^{+0.3}_{-0.7}$	$^{+0.7}_{-0.4}$
$\mu\ Z\gamma$	$^{+0.7}_{-0.2}$	$^{+0.6}_{-0.5}$	$^{+0.7}_{-0.4}$
$e+\mu\ Z\gamma$	$^{+0.7}_{-0.2}$	$^{+0.5}_{-0.2}$	$^{+0.5}_{-0.3}$

However, due to the correlations between the experimental and Monte Carlo systematic uncertainties, the *difference* in systematic uncertainties must be used in determining limits on the $\Delta\kappa$ and λ parameters for $W\gamma$ or limits on the $h_{i0}^{Z,\gamma}$ parameters for $Z\gamma$.

When determining $\Delta\kappa$ and λ limits, systematic uncertainties arising from the compositeness scale and form factor power of the anomalous parameters of the W (Λ_W, $n_{\kappa,\lambda}^{W}$) and the Z (Λ_Z, $n^{Z}_{h_{i0}^{Z,\gamma}}$) need to be taken into account. Systematic effects due to these parameters are discussed in Sections 2.2 and 2.4.

Chapter 8

Determination of $\sigma \cdot BR(W+\gamma)$, $\sigma \cdot BR(Z+\gamma)$ and Cross Section Ratios in the Muon Channel

8.1 Methodology for Determination of $\sigma \cdot BR(W+\gamma)$ and $\sigma \cdot BR(Z+\gamma)$

The experimental results for the $\sigma \cdot BR(W+\gamma)$ and $\sigma \cdot BR(Z+\gamma)$ were determined with the use of the cross section Equation 5.1 and a Monte Carlo simulation program to determine the statistical, systematic and combined errors. We Monte Carlo simulate 10^6 CDF "experiments", Poisson-fluctuating the number of observed events, Gaussian fluctuating the integrated luminosities, acceptances and efficiencies (See Tables 5.4, 5.1). The individual backgrounds for each channel (See Tables 6.2-6.5) were Gaussian fluctuated and subtracted from the observed number of events for each of the Monte Carlo "experiments", and the result was entered into

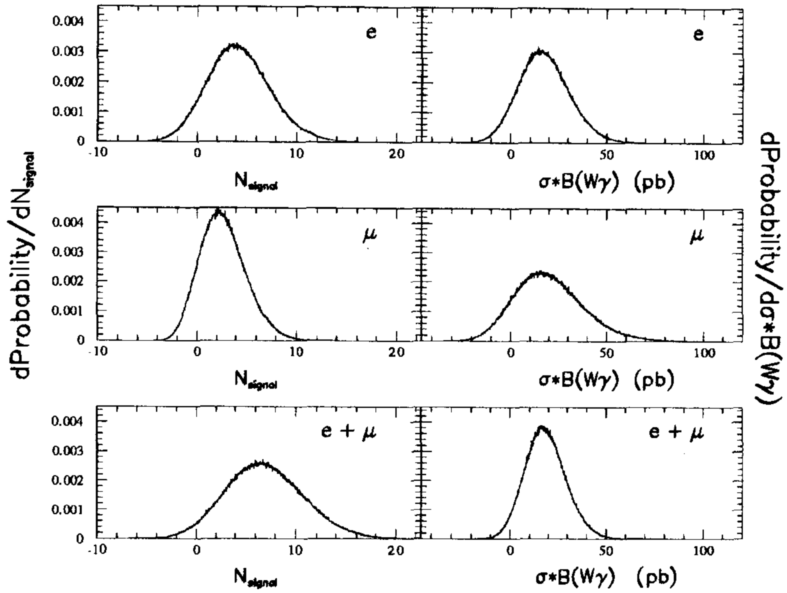

Figure 8.1: Electron and muon and combined $e + \mu$ $N_{signal}^{W+\gamma}$ and $\sigma \cdot B(W + \gamma)$ probability distributions.

a finely binned histogram. The experimental cross section was extracted from this histogram, along with the mean and double sided uncertainties and the single sided confidence upper limit on $\sigma \cdot BR$, using the method of a bounded physical region [51].

8.2 Combining Electron and Muon Channel Results

The muon channel analysis for $W\gamma$ and $Z\gamma$ was done in parallel with the electron channel $W\gamma$ and $Z\gamma$ analyses performed by D. Benjamin and M. Roach[52] respectively, in a collaborative effort. Given the small event sample size available for studying these di-boson production processes, these measurements will have large statistical uncertainties. By combining the individual muon and electron $W\gamma$ and $Z\gamma$ cross section results the statistical uncertainty on the measurement of the cross sections is reduced.

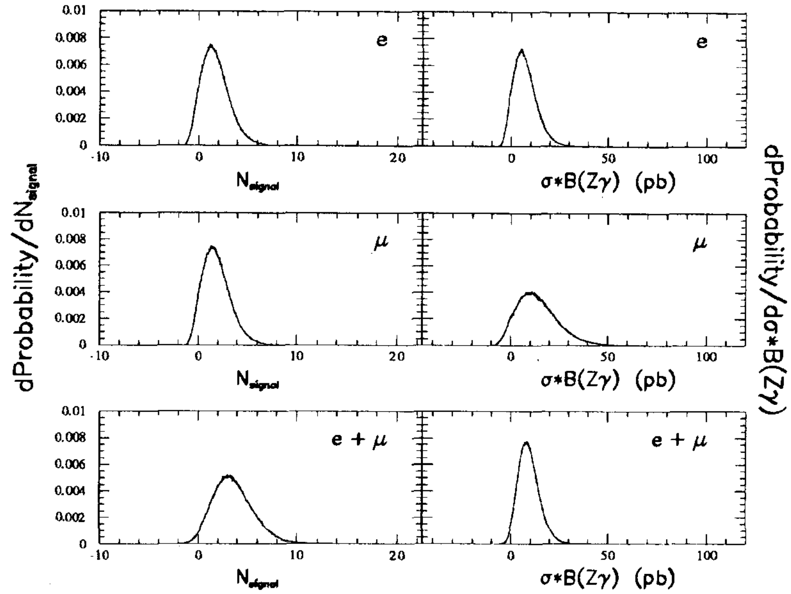

Figure 8.2: Electron and muon and combined $e+\mu$ $N_{signal}^{Z+\gamma}$ and $\sigma \cdot B(Z+\gamma)$ probability distributions.

In order to combine the individual $\sigma \cdot B(V_\ell + \gamma)$ production cross sections × decay branching ratios for $\ell = \mu, e$ and $V = W, Z$ the assumption is made that lepton universality holds: $\sigma \cdot B = \sigma \cdot B_e = \sigma \cdot B_\mu$). Then, the combined $e+\mu$ production × decay branching ratio for $V+\gamma$ is given by:

$$\sigma \cdot B(V+\gamma)_{e+\mu} = \frac{N_{signal}^{e} + N_{signal}^{\mu}}{\int \mathcal{L}_e dt \cdot \left(A_{V\gamma}^{e} \cdot \epsilon_{V\gamma}^{e}\right) + \int \mathcal{L}_\mu dt \cdot \left(A_{V\gamma}^{\mu} \cdot \epsilon_{V\gamma}^{\mu}\right)} \tag{8.1}$$

The determinations of limits on the anomalous couplings for $W\gamma$ and $Z\gamma$ from the combined $e+\mu$ measurement was done in the same fashion as for the individual μ channel $W\gamma$ and $Z\gamma$ limits. This method of combining $e+\mu$ cross sections has been extensively cross-checked with test distributions and also with analytic methods. These cross checks yield extremely consistent results for the combined cross section, as well as $\pm 1\sigma$ statistical and systematic uncertainties.

Figures 8.1 and 8.2 show the e, μ and $e + \mu$ combined $W\gamma$ and $Z\gamma$ $\sigma \cdot B$ probability distributions, respectively. Due in large part to small-number Poisson statistics, these $\sigma \cdot B$ probability distributions have a small high-side tail extending out from their otherwise nearly Gaussian shape. The narrowing of the $\sigma \cdot B$ probability distribution for the $e + \mu$ combined cross sections relative to the individual e and μ channel $\sigma \cdot B$ probability distributions is readily apparent.

8.3 Absolute Cross Section results

The measured and SM predicted muon $W\gamma$ and $Z\gamma$ absolute cross sections, including all systematic uncertainties, are:

$$\begin{aligned}
\sigma \cdot B(W\gamma)_\mu &= 19.4^{+18.3}_{-17.9} \quad (stat + syst)\ \mathrm{pb} \\
\sigma \cdot B(W\gamma)_{SM} &= 19.2^{+3.3}_{-0.9} \quad (stat + syst)\ \mathrm{pb} \\
\sigma \cdot B(Z\gamma)_\mu &= 13.6^{+10.3}_{-10.1} \quad (stat + syst)\ \mathrm{pb} \\
\sigma \cdot B(Z\gamma)_{SM} &= 4.7^{+0.7}_{-0.2} \quad (stat + syst)\ \mathrm{pb}
\end{aligned}$$

Because of correlations between the Monte Carlo predicted $\sigma \cdot B(V_\mu + \gamma)_{cuts}$ and the experimental $\sigma \cdot B(V_\mu + \gamma)_{expt}$, the results listed in this section must *not* be used in determining limits on the anomalous parameters of $W\gamma$ ($\Delta\kappa$ and λ) or $Z\gamma$ ($h_{i0}^{Z,\gamma}$).

The electron channel results, including all systematic uncertainties, are[52]:

$$\begin{aligned}
\sigma \cdot B(W\gamma)_e &= 17.0^{+13.6}_{-13.4} \quad (stat + syst)\ \mathrm{pb} \\
\sigma \cdot B(W\gamma)_{SM} &= 18.8^{+3.3}_{-0.9} \quad (stat + syst)\ \mathrm{pb} \\
\sigma \cdot B(Z\gamma)_e &= 6.8^{+5.7}_{-5.7} \quad (stat + syst)\ \mathrm{pb} \\
\sigma \cdot B(Z\gamma)_{SM} &= 4.7^{+0.7}_{-0.2} \quad (stat + syst)\ \mathrm{pb}
\end{aligned}$$

The combined $\mu + e$ absolute cross sections, including all systematic uncertainties, are[52]:

$$\begin{aligned}
\sigma \cdot B(W\gamma)_{\mu+e} &= 17.9^{+11.0}_{-10.7} \quad (stat + syst)\ \mathrm{pb} \\
\sigma \cdot B(W\gamma)_{SM} &= 19.2^{+3.3}_{-0.9} \quad (stat + syst)\ \mathrm{pb} \\
\sigma \cdot B(Z\gamma)_{\mu+e} &= 9.2^{+5.2}_{-5.1} \quad (stat + syst)\ \mathrm{pb} \\
\sigma \cdot B(Z\gamma)_{SM} &= 4.7^{+0.7}_{-0.2} \quad (stat + syst)\ \mathrm{pb}
\end{aligned}$$

8.4 Cross Section Ratio Results

The cross section ratios of W/Z are interesting as many of the common systematic errors cancel in the ratio. The inclusive W/Z cross sections ratios in the e, μ channels and combined $e + \mu$ channel, measured from 1988-89 data have been published by CDF previously [5],

$$\mathcal{R}(W/Z)_\ell \equiv \sigma \cdot B(W_\ell)/\sigma \cdot B(Z_\ell)$$

We define three additional cross section ratios:

$$\begin{aligned}
\mathcal{R}(W\gamma/W)_\ell &\equiv \sigma \cdot B(W_\ell + \gamma)/\sigma \cdot B(W_\ell) \\
\mathcal{R}(Z\gamma/Z)_\ell &\equiv \sigma \cdot B(Z_\ell + \gamma)/\sigma \cdot B(Z_\ell) \\
\mathcal{R}(W\gamma/Z\gamma)_\ell &\equiv \sigma \cdot B(W_\ell + \gamma)/\sigma \cdot B(Z_\ell + \gamma)
\end{aligned}$$

The uncertainty on the experimental measurement of the ratio of the cross sections is smaller than the uncertainty on the respective cross sections because many experimental and theoretical uncertainties cancel in the ratio [5]. Our cross section ratio results, along with the previous CDF result, are summarized below, and are shown in Figure 8.3.

The muon channel absolute cross section results for $W\gamma$ and $Z\gamma$ are:

Cross Section Ratio	$\mathcal{R}_{Experiment}$	$\mathcal{R}_{\mathrm{SM}Predicted}$
$\mathcal{R}(W\gamma/W)_\mu$	$0.9^{+0.8}_{-0.8}\%$	$0.92 \pm 0.02\%$
$\mathcal{R}(Z\gamma/Z)_\mu$	$6.0^{+4.6}_{-4.4}\%$	$2.42 \pm 0.04\%$
$\mathcal{R}(W\gamma/Z\gamma)_\mu$	$1.4^{+1.8}_{-1.3}$	4.00 ± 0.07
$\mathcal{R}(W/Z)_\mu$	$9.8^{+1.2}_{-1.2}$	10.69 ± 0.22

The electron channel absolute cross section results for $W\gamma$ and $Z\gamma$ are:

Cross Section Ratio	$\mathcal{R}_{Experiment}$	$\mathcal{R}_{\mathrm{SM}Predicted}$
$\mathcal{R}(W\gamma/W)_e$	$0.8^{+0.6}_{-0.6}\%$	$0.92 \pm 0.02\%$
$\mathcal{R}(Z\gamma/Z)_e$	$3.3^{+2.7}_{-2.7}\%$	$2.42 \pm 0.04\%$
$\mathcal{R}(W\gamma/Z\gamma)_e$	$2.5^{+2.7}_{-2.4}$	4.00 ± 0.07
$\mathcal{R}(W/Z)_e$	$10.2^{+0.9}_{-0.9}$	10.69 ± 0.22

The combined $\mu + e$ absolute cross section results for $W\gamma$ and $Z\gamma$ are:

Cross Section Ratio	$\mathcal{R}_{Experiment}$	$\mathcal{R}_{\mathrm{SM}Predicted}$
$\mathcal{R}(W\gamma/W)_{\mu+e}$	$0.8^{+0.5}_{-0.5}\%$	$0.92 \pm 0.02\%$
$\mathcal{R}(Z\gamma/Z)_{\mu+e}$	$4.3^{+2.5}_{-2.4}\%$	$2.42 \pm 0.04\%$
$\mathcal{R}(W\gamma/Z\gamma)_{\mu+e}$	$1.9^{+2.0}_{-1.3}$	4.00 ± 0.07
$\mathcal{R}(W/Z)_{\mu+e}$	$10.0^{+0.7}_{-0.7}$	10.69 ± 0.22

Note that the cross section ratio $\mathcal{R}(Z\gamma/Z)_{\mu}$ is significantly higher than the SM prediction, while the cross section ratio $\mathcal{R}(W\gamma/Z\gamma)_{\mu}$ is significantly lower than the SM prediction, because the measured $\sigma \cdot B(Z_{\mu} + \gamma)$ obtained with our very limited statistics is substantially higher than the SM predicted value.

The cross section ratios $\mathcal{R}(W\gamma/W)\mu$ and $\mathcal{R}(W\gamma/Z)$ are sensitive to the SM destructive interference between the Feynman amplitudes for the $W\gamma$ process [53]. The Figure 8.3 shows both the SM predicted values for these ratios, as well as the predicted value of the cross section ratios if the cross section term in the numerator or the denominator of the ratios includes only photons due to final-state bremsstrahlung.

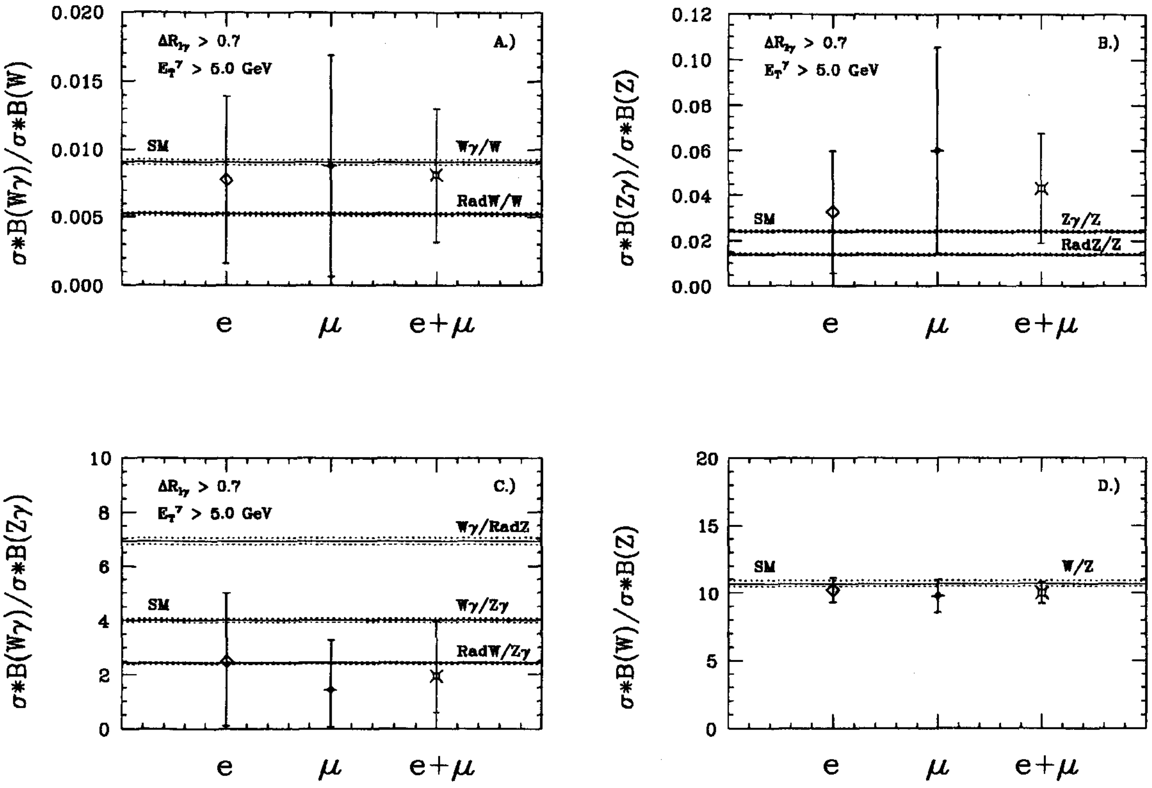

Figure 8.3: W/Z cross section ratios for e, μ and combined $e + \mu$ channels. For each plot, appropriately labeled horizontal lines indicate the Standard Model and "Radiative only" cross section ratios predictions, with their $\pm 1\sigma$ theoretical uncertainties indicated by the adjacent dotted lines. (A) Cross section ratio $\mathcal{R}(W\gamma/W)_\ell = \sigma \cdot B(W\gamma)/\sigma \cdot B(W)$. (B) Cross section ratio $\mathcal{R}(Z\gamma/Z)_\ell = \sigma \cdot B(Z\gamma)/\sigma \cdot B(Z)$. (C) Cross section ratios $\mathcal{R}(W\gamma/Z\gamma)_\ell = \sigma \cdot B(W\gamma)/\sigma \cdot B(Z\gamma)$. (D) Cross section ratios $\mathcal{R}(W/Z)_\ell = \sigma \cdot B(W)/\sigma \cdot B(Z)$.

Chapter 9

Determination of Limits on Anomalous Couplings for $W\gamma$ and $Z\gamma$

For $W\gamma$, if any of the anomalous couplings deviate from their Standard model values, $\sigma \cdot BR(W+\gamma)$ may either increase or (very slightly decrease)[1] from the SM value. Also, the E_T^γ and η_γ distributions will be different from those predicted by the SM, as shown in Figures 2.3 and 2.4, and summarized in Table 9.1. For most values of the anomalous parameters, an excess of high-E_T photons from $W\gamma$ is expected, and a similar effect is seen in the case of $Z\gamma$. These cross sections are approximately quadratically dependent on the values of the anomalous couplings. Experimentally, the limits on the anomalous $WW\gamma$ and $ZZ\gamma/Z\gamma\gamma$ couplings are determined by the absence of an excess of high-E_T photons in $W\gamma$ or $Z\gamma$ events.

When considering limits on the anomalous couplings for $W\gamma$, we restrict ourselves to considering the two parameters, κ and λ, as there already exist strict indirect experimental limits on $\tilde{\kappa}$ and $\tilde{\lambda}$ from experimental limits on the neutron electric dipole moment, of $d_n < 12\times 10^{-26}\ e-\mathrm{cm}$

---

[1] For example, for $W\gamma$ $\Delta\kappa = 0.33$, $\lambda = -0.09$ $\sigma \cdot BR(W+\gamma)$ is $\simeq 0.16\%$ less than the SM predicted value, and is the global minimum of $\sigma \cdot B(\Delta\kappa, \lambda)_W$ at our CM energy.

@ 95% CL[54]. These limits are $|\tilde{\kappa}|,\ |\tilde{\lambda}| < \mathcal{O}(10^{-3})$, unless extreme cancellation between these two parameters occurs [6, 55]. However, due to the nature of the $WW\gamma$ vertex function, our direct experimental limits on $\tilde{\kappa}$ and $\tilde{\lambda}$ are within $\leq 10\%$ of the direct experimental limits obtained for $\Delta\kappa$ and λ, respectively.

For $Z\gamma$, we consider only two sets of anomalous couplings for each of $ZZ\gamma$ and $Z\gamma\gamma$. Since there is no interference between the anomalous $\mathcal{CP}$−conserving couplings $h^V_{30,40}$ and the $\mathcal{CP}$−violating couplings $h^V_{10,20}$ ($V = Z,\ \gamma$), and only weak interference between the anomalous $ZZ\gamma$ couplings and the anomalous $Z\gamma\gamma$ couplings [10], we choose to independently examine the following sets of anomalous parameters:

(1) $ZZ\gamma$: h^Z_{30} and h^Z_{40} *only*
(2) $ZZ\gamma$: h^Z_{10} and h^Z_{20} *only*
(3) $Z\gamma\gamma$: h^γ_{30} and h^γ_{40} *only*
(4) $Z\gamma\gamma$: h^γ_{10} and h^γ_{20} *only*

Due to the structure of the $ZZ\gamma$ and $Z\gamma\gamma$ vertex functions the experimental limits obtained for the anomalous parameters of (1) will be within $\sim 1\%$ of the limits obtained for the anomalous parameters of (2). Similarly, the experimental limits obtained for the anomalous parameters of (3) will be within $\sim 1\%$ of the limits obtained for the anomalous parameters of (4). The experimental limits on anomalous couplings for the $Z\gamma\gamma$ vertex function are $\sim 5\%$ greater than the equivalent anomalous couplings for the $ZZ\gamma$ vertex function. We therefore present the experimental upper limits only on h^Z_{30} and h^Z_{40} anomalous $ZZ\gamma$ couplings. The corresponding experimental limits on h^Z_{10} and h^Z_{20} are then within $\sim 1\%$ of those for h^Z_{30} and h^Z_{40} respectively. The experimental limits on anomalous $Z\gamma\gamma$ couplings are then obtained by inflating the limits

Table 9.1: Sample Monte Carlo predictions for the Number of Muon $W\gamma$ Events. The statistical uncertainty associated with each quantity is given.

Anomalous Coupling		$E_T^\gamma > 5$ GeV	$5 < E_T^\gamma \leq 15$ GeV	$E_T^\gamma > 15$ GeV
μ $W\gamma$:	$\Delta\kappa = 0,\ \lambda = 0$ (SM)	2.5 ± 0.2	2.0 ± 0.2	0.5 ± 0.1
μ $W\gamma$:	$\Delta\kappa = 7,\ \lambda = 0$	6.0 ± 0.6	2.5 ± 0.2	3.5 ± 0.3
μ $W\gamma$:	$\Delta\kappa = 0,\ \lambda = 3$	7.3 ± 0.7	2.3 ± 0.2	5.0 ± 0.5
μ $W\gamma$:	$\Delta\kappa = 5,\ \lambda = 5$	22.6 ± 2.2	3.1 ± 0.3	19.5 ± 1.9

on anomalous $ZZ\gamma$ couplings by 5%, *i.e.* $h_{i0}^\gamma = 1.05 h_{i0}^Z$ for $i = 1 - 4$. These derived limits on the other anomalous couplings will be accurate to within a few tenths of a percent.

9.1 General Method of Obtaining Limits on the Anomalous Parameters

In order to determine limits on the anomalous parameters for $W\gamma$ ($Z\gamma$) the Baur Monte Carlo programs were run to generate a grid in $\Delta\kappa$-λ (h_{30}^Z-h_{40}^Z) space. For each point in the grid, the four-vector data produced by the Baur generator(s) were analyzed with the fast $W\gamma/Z\gamma$ Monte Carlo detector simulation programs, and the $\sigma \cdot BR(V_\mu + \gamma)_{gen}$ and $\sigma \cdot BR(V_\mu + \gamma)_{cuts}$, the kinematic and geometrical acceptances, and the resulting predicted number of $W\gamma/Z\gamma$ events passing all cuts, and all statistical uncertainties associated with each of these values were recorded. Thus a 3-dimensional surface of $\sigma \cdot BR(V_\mu + \gamma)_{cuts}$ was generated for the range of anomalous coupling parameters in the grid.

Table 9.1 summarizes the photon E_T spectrum in several E_T bins, for a few of the grid points in the $\Delta\kappa$-λ plane. Note that not only does the total number of expected photons increase as the grid points get further away for the SM Monte Carlo prediction, but the ratio of photons with $E_T^\gamma > 15$ GeV to photons with $5 \leq E_T^\gamma \leq 15$ GeV increases rapidly.

This 3-dimensional surface was then fit with MINUIT[56] to get a 3-dimensional analytic description of the $\sigma \cdot BR(V_\mu + \gamma)_{cuts}$ surface in the $\Delta\kappa$-λ (h_{30}^Z-h_{40}^Z) plane. The generic form of this parameterization the 3-dimensional surface of a complex elliptic paraboloid:

$$\sigma(x,y)_{cuts} \; = \; \sigma_{SM} \; + \; ax \; + \; bx^2 \; + \; cy \; + \; dy^2 \; + \; exy \tag{9.1}$$

where $x \; = \; \Delta\kappa \; (h_{30}^Z)$ and $y \; = \; \lambda \; (h_{40}^Z)$. Since the invariant amplitude $\mathcal{M}_{V\gamma}$ is linear in the anomalous parameters, no higher order terms are needed in the analytic parameterization. The linear terms arise from the cross terms due to interference between the various anomalous amplitudes that contribute to the $W\gamma/Z\gamma$ processes.

As an example, the parameterization for the $\sigma \cdot BR(W_\mu + \gamma)_{cuts}$ surface is

$$\begin{aligned}\sigma \cdot B(\Delta\kappa, \lambda)_{W\gamma} \quad &= \; (19.17 \pm 0.07) \; - \; (0.18 \pm 0.02)\Delta\kappa \; + \; (0.41 \pm 0.002)(\Delta\kappa)^2 \\ &+ (0.06 \pm 0.04)\lambda \; + \; (1.90 \pm 0.01)\lambda^2 \; + \; (0.88 \pm 0.03)(\Delta\kappa \cdot \lambda) \quad \text{(pb)}\end{aligned}$$

and the parameterization for the $\sigma \cdot BR(Z_\mu + \gamma)_{cuts}$ surface, for a compositeness scale $\Lambda_Z = 500$ GeV, is

$$\begin{aligned}\sigma \cdot B(h_{30}^Z, h_{40}^Z)_{Z\gamma} \quad &= \; (4.72 \pm 0.03) \; - \; (0.02 \pm 0.004)h_{30}^Z \; + \; (0.16 \pm 7 \times 10^{-4})(h_{30}^Z)^2 \\ &- (0.06 \pm 0.03)h_{40}^Z \; + \; (2.31 \pm 0.05)(h_{40}^Z)^2 \; - \; (1.01 \pm 0.006)(h_{30}^Z \cdot h_{40}^Z) \quad \text{(pb)}\end{aligned}$$

The determination of the 1σ, 90% and 95% confidence level upper limits on anomalous $WW\gamma$, $ZZ\gamma$, and $Z\gamma\gamma$ must take into account not only the systematic uncertainties on $\sigma \cdot BR(V_\mu + \gamma)$ for $W\gamma$ and $Z\gamma$, but the correlations between the Monte Carlo results and the experimental results due to the common use of the kinematic/geometric acceptances in both calculations. The systematic uncertainty used when comparing the experimental results with those of the Monte Carlo are the overall relative systematic uncertainty *difference* between the Monte Carlo prediction and the experimental result, $\Delta\sigma \cdot BR(V_\mu + \gamma)^{overall}_{MC-expt}$. The contour in the $\Delta\kappa$,λ (h^Z_{30},h^Z_{40}) plane that is formed by the intersection of

- the plane of 1 σ (68%), 90%, or 95% confidence level upper limit on the experimental $\sigma \cdot BR(V_\mu + \gamma)$ ^{expt}
- the analytic cross section surface expression found from the MINUIT fit to the Baur Monte Carlo $\sigma \cdot BR(V_\mu + \gamma)_{cuts}$ cross section surface, shifted relative to its nominal central value by $-\Delta\sigma \cdot BR(V_\mu + \gamma)^{overall}_{MC-expt}$.

is the limiting contour of the respective anomalous couplings for $W\gamma$ ($Z\gamma$).

9.2 Limits on $WW\gamma$ Anomalous Couplings

The 1σ, 90%, and 95% confidence level limits on $\Delta\kappa$ and λ for the muon, electron and combined $\mu + e$ channels are listed in Tables 9.2, 9.3 and 9.4. Figure 9.1 show the projections of the predicted $W\gamma$ cross section on the $\Delta\kappa/\lambda$ axes. The value of the $\sigma \cdot BR(W + \gamma)_{expt}$ is shown as a solid horizontal line, with the $\pm 1\sigma$ (stat+syst) uncertainties indicated by dotted horizontal lines. The 90% and 95% single-sided confidence level upper limits on the experimental cross section are show as horizontal dashed lines.

Figure 9.2 shows the 1σ, 90%, and 95% single sided confidence level contours in the $\Delta\kappa$-λ plane. Also shown are the $\sigma \cdot BR(W + \gamma)$ minimum at $\Delta\kappa = 0.33$, $\lambda = -0.09$, and the

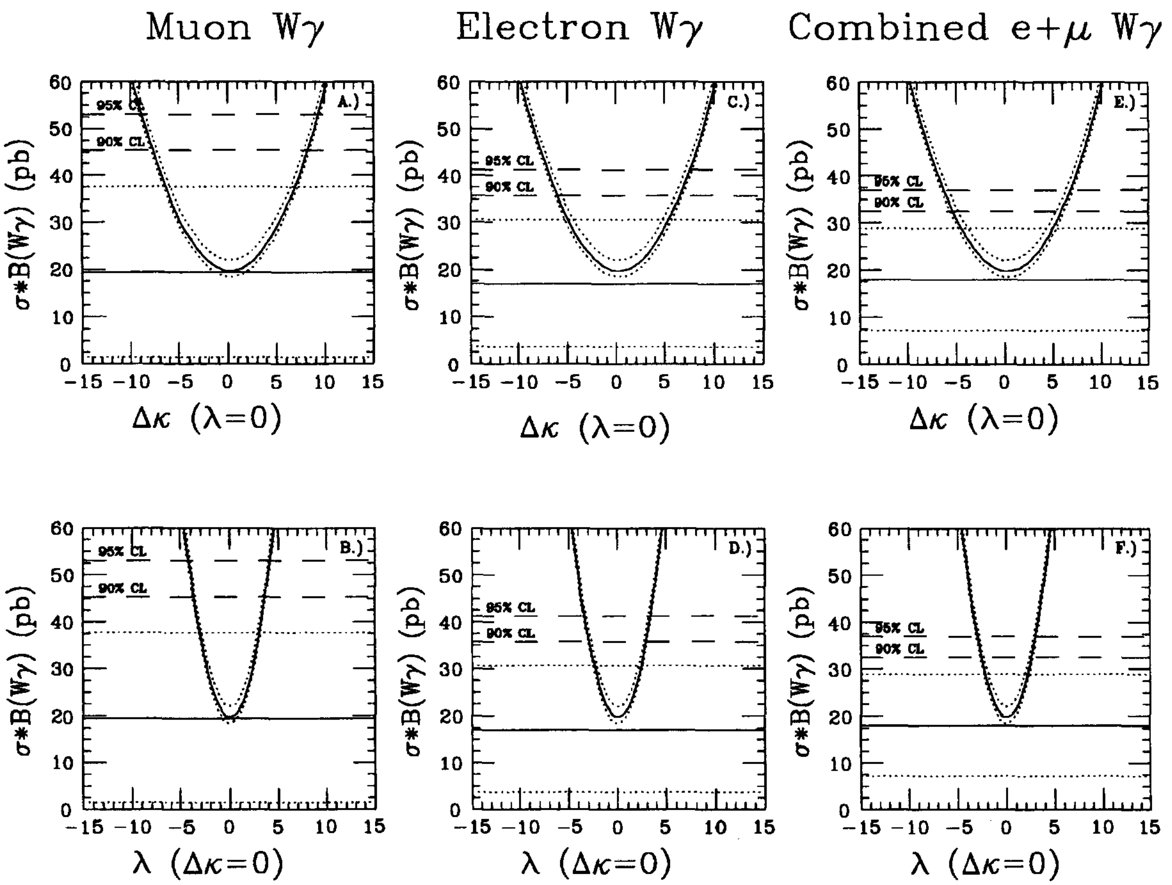

Figure 9.1: Figures A), C) and E): Limits on $\sigma \cdot BR(W+\gamma)$ as a function of $\Delta\kappa$ with $\lambda = 0$. Figures B),D) and F): Limits on $\sigma \cdot BR(W+\gamma)$ as a function of λ with $\Delta\kappa = 0$. The central value and the associated double sided $\pm 1 - \sigma$ (stat+syst) confidence interval, and the 90% and 95% upper limit confidence levels are indicated by the respectively labeled horizontal lines. The central value of the predicted $\sigma \cdot BR(W+\gamma)$ as a function of $\Delta\kappa$ or λ is shown as a solid curve. The dotted curves are the $\pm 1\sigma$ common systematic uncertainty differences between the theoretical predictions and the experimental measurement.

orthogonal dashed lines where the magnetic dipole and electric quadrupole moment of the W are zero. The unitarity limits on the anomalous parameters, discussed in the next section, are also indicated in Figure 9.2.

Table 9.2: Muon $W\gamma$ $\Delta\kappa - \lambda$ Limits. The $\pm 1\sigma$, (68.3% CL) double-sided (DS) limits and the the 68.3%, 90.0% and 95.0% single-sided (SS) CL upper limits on $\Delta\kappa$ and λ are given. See text for further details.

Parameter	CL Range	Muon Limits
$\Delta\kappa$	68.3% DS CL	$0.0^{+6.6}_{-6.1}(stat) \pm 0.5(syst) = 0.0^{+7.1}_{-6.6}(stat + syst)$
	68.3% SS CL	$-5.0 < \Delta\kappa < +5.4$
$(\lambda = 0)$	90.0% SS CL	$-7.9 < \Delta\kappa < +8.3$
	95.0% SS CL	$-9.0 < \Delta\kappa < +9.4$
λ	68.3% DS CL	$0.0^{+2.9}_{-2.9}(stat) \pm 0.3(syst) = 0.0^{+3.2}_{-3.2}(stat + syst)$
	68.3% SS CL	$-2.4 < \lambda < +2.4$
$(\Delta\kappa = 0)$	90.0% SS CL	$-3.8 < \lambda < +3.7$
	95.0% SS CL	$-4.3 < \lambda < +4.2$

Table 9.3: Electron $W\gamma$ $\Delta\kappa - \lambda$ Limits. The $\pm 1\sigma$ (68.3% CL) double-sided (DS) limits and the the 68.3%, 90.0% and 95.0% single-sided (SS) CL upper limits on $\Delta\kappa$ and λ are given. See text for further details.

Parameter	CL Range	Electron Limits
$\Delta\kappa$	68.3% DS CL	$0.0^{+5.0}_{-4.5}(stat) \pm 0.7(syst) = 0.0^{+5.7}_{-5.2}(stat + syst)$
	68.3% SS CL	$-3.5 < \Delta\kappa < +3.9$
$(\lambda = 0)$	90.0% SS CL	$-6.3 < \Delta\kappa < +6.7$
	95.0% SS CL	$-7.2 < \Delta\kappa < +7.7$
λ	68.3% DS CL	$0.0^{+2.2}_{-2.2}(stat) \pm 0.3(syst) = 0.0^{+2.5}_{-2.5}(stat + syst)$
	68.3% SS CL	$-1.7 < \lambda < +1.7$
$(\Delta\kappa = 0)$	90.0% SS CL	$-3.0 < \lambda < +3.0$
	95.0% SS CL	$-3.5 < \lambda < +3.4$

Table 9.4: Combined $\mu + e$ channel $W\gamma$ $\Delta\kappa - \lambda$ Limits. The $\pm 1\sigma$, (68.3%) CL double-sided (DS) limits and the the 68.3%, 90.0% and 95.0% single-sided (SS) CL upper limits on $\Delta\kappa$ and λ are given. See text for further details.

Parameter	CL Range	Combined $e + \mu$ Limits
$\Delta\kappa$	68.3% DS CL	$0.0^{+4.7}_{-4.2}(stat) \pm 0.6(syst) = 0.0^{+5.3}_{-4.8}(stat + syst)$
	68.3% SS CL	$-3.2 < \Delta\kappa < +3.7$
$(\lambda = 0)$	90.0% SS CL	$-5.7 < \Delta\kappa < +6.1$
	95.0% SS CL	$-6.5 < \Delta\kappa < +7.0$
λ	68.3% DS CL	$0.0^{+2.0}_{-2.0}(stat) \pm 0.3(syst) = 0.0^{+2.3}_{-2.4}(stat + syst)$
	68.3% SS CL	$-1.6 < \lambda < +1.6$
$(\Delta\kappa = 0)$	90.0% SS CL	$-2.7 < \lambda < +2.7$
	95.0% SS CL	$-3.1 < \lambda < +3.1$

9.3 Limits on the Higher Order EM Moments of the W Boson

Experimental limits on the $\Delta\kappa$ and λ anomalous $WW\gamma$ couplings also place bounds on the higher order electromagnetic multipole-moments of the W boson, in the static limit (photon energy → 0). The magnetic dipole, electric quadrupole moment and the mean-square charge radius of the W boson are related to the $\Delta\kappa$ and λ parameters by: (with $\hbar = c = 1$)

$$\begin{aligned} \mu_W &= \tfrac{e}{2M_W}(2 + \Delta\kappa + \lambda) && \text{Magnetic Dipole Moment} && (9.2) \\ Q^e_W &= -\tfrac{e}{M^2_W}(1 + \Delta\kappa - \lambda) && \text{Electric Quadrupole Moment} && (9.3) \\ <R^2_W> &= \tfrac{1}{M^2_W}(1 + \Delta\kappa + \lambda) && \text{Mean} - \text{Squared Charge Radius} && (9.4) \end{aligned}$$

In Figure 9.3 the contours of Figure 9.2 have been transformed into the Q^e_W/Q^{e0}_W-μ_W/μ^0_W plane, where $Q^e_W = \frac{-e}{M^2_W} = -e\,\lambda\!\!\!^-{}^2_W$ and $\mu_W = \frac{e\,\hbar}{2M_W}$. Table 9.5 lists the muon channel limits for the W EM moments, and Tables 9.6 and 9.7 list the W EM moments for the electron and combined $\mu + e$ channels respectively.

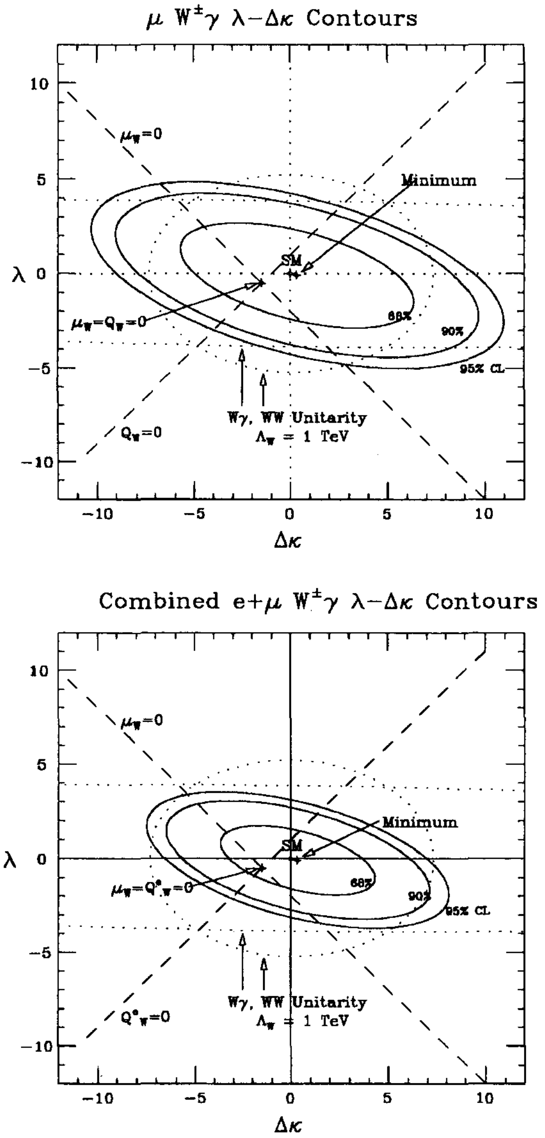

Figure 9.2: $\Delta\kappa$-λ contour limits for μ and combined $\mu + e$ $W\gamma$, top and bottom plots respectively. The 1σ, 90% and 95% single sided confidence upper limits are shown as solid line ellipses. The W^+W^- and $W\gamma$ unitarity limits for a compositeness scale $\Lambda_W = 1\,TeV$ and form factor power $n = 2$, are indicated by the dotted curves. The dashed lines labeled $Q_W = 0$ and $\mu_W = 0$ are the axes along which the electric quadrupole and the magnetic dipole of the W vanishes. These axes intersect at $(\Delta\kappa, \lambda) = (-\frac{3}{2}, -\frac{1}{2})$.

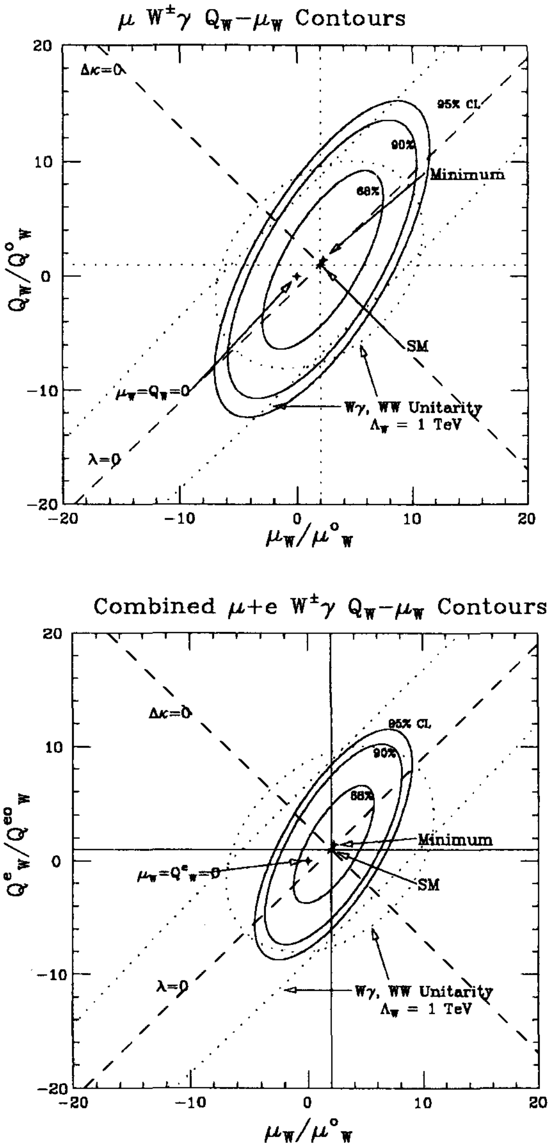

Figure 9.3: $\frac{Q^e_W}{Q^{eo}_W} - \frac{\mu_W}{\mu^o_W}$ contour limits for μ and combined $\mu + e$ $W\gamma$, top and bottom plots respectively. The solid ellipses show the 1σ, 90.0% and 95.0% single-sided CL upper limits in the μ_W/μ^o_W – Q^e_W/Q^{eo}_W plane. The $\Delta\kappa$ and λ axes are indicated by (orthogonal) dashed lines, intersecting at the point $(\mu_W/\mu^o_W,\ Q^e_W/Q^{eo}_W) = (2,\ 1)$. The W^+W^- and $W\gamma$ unitarity limits for a compositeness scale $\Lambda_W = 1$ TeV and form factor power $n = 2$ are indicated by the dotted curves. See text for further details.

Table 9.5: Muon Limits on W Boson EM Moments. The $\pm 1\sigma$, (68.3%) CL double-sided (DS) limits and the the 68.3%, 90.0% and 95.0% single-sided (SS) CL upper limits on μ_W/μ_W° and Q_W^e/Q_W^{eo} are given. See text for further details.

Parameter	CL Range	Muon Limits
μ_W/μ_W°	68.3% $DS\ CL$	$2.0\ ^{+4.6}_{-4.5}\ (\boldsymbol{stat})\ \pm\ 0.4\ (\boldsymbol{syst})\ =\ 2.0\ ^{+4.9}_{-4.8}\ (\boldsymbol{stat}+\boldsymbol{syst})$
	68.3% $SS\ CL$	$-3.7\ <\ \mu_W/\mu_W^\circ - 2\ \equiv\ g_W - 2\ <\ +3.7$
$(Q_W^e/Q_W^{eo} = 1)$	90.0% $SS\ CL$	$-5.7\ <\ \mu_W/\mu_W^\circ - 2\ \equiv\ g_W - 2\ <\ +5.8$
	95.0% $SS\ CL$	$-6.5\ <\ \mu_W/\mu_W^\circ - 2\ \equiv\ g_W - 2\ <\ +6.6$
Q_W^e/Q_W^{eo}	68.3% $DS\ CL$	$1.0\ ^{+6.9}_{-6.6}\ (\boldsymbol{stat})\ \pm\ 0.6\ (\boldsymbol{syst})\ =\ 1.0\ ^{+7.5}_{-7.1}\ (\boldsymbol{stat}+\boldsymbol{syst})$
	68.3% $SS\ CL$	$-5.4\ <\ Q_W^e/Q_W^{eo} - 1\ \equiv\ q_W^e - 1\ <\ +5.7$
$(\mu_W/\mu_W^\circ = 2)$	90.0% $SS\ CL$	$-8.4\ <\ Q_W^e/Q_W^{eo} - 1\ \equiv\ q_W^e - 1\ <\ +8.8$
	95.0% $SS\ CL$	$-9.7\ <\ Q_W^e/Q_W^{eo} - 1\ \equiv\ q_W^e - 1\ <+10.0$
$<R_W>^2\ /\ \bar{\lambda}_W^2$	68.3% $DS\ CL$	$1.0\ ^{+4.6}_{-4.5}\ (\boldsymbol{stat})\ \pm\ 0.5\ (\boldsymbol{syst})\ =\ 1.0\ ^{+4.9}_{-4.8}\ (\boldsymbol{stat}+\boldsymbol{syst})$
	68.3% $SS\ CL$	$-3.7\ <\ <R_W^2>\ /\ \bar{\lambda}_W^2 - 1\ \equiv\ r_W^2 - 1\ <\ +3.7$
$(Q_W^e/Q_W^{eo} = 1)$	90.0% $SS\ CL$	$-5.7\ <\ <R_W^2>\ /\ \bar{\lambda}_W^2 - 1\ \equiv\ r_W^2 - 1\ <\ +5.8$
	95.0% $SS\ CL$	$-6.5\ <\ <R_W^2>\ /\ \bar{\lambda}_W^2 - 1\ \equiv\ r_W^2 - 1\ <\ +6.6$

Table 9.6: Electron Limits on W Boson EM Moments. The $\pm 1\sigma$, (68.3%) CL double-sided (DS) limits and the the 68.3%, 90.0% and 95.0% single-sided (SS) CL upper limits on μ_W/μ_W° and Q_W^e/Q_W^{eo} are given. See text for further details.

Parameter	CL Range	Electron Limits
μ_W/μ_W°	68.3% $DS\ CL$	$2.0\ ^{+3.4}_{-3.4}\ (\boldsymbol{stat})\ \pm\ 0.5\ (\boldsymbol{syst})\ =\ 2.0\ ^{+3.9}_{-3.9}\ (\boldsymbol{stat}+\boldsymbol{syst})$
	68.3% $SS\ CL$	$-2.6\ <\ \mu_W/\mu_W^\circ - 2\ \equiv\ g_W - 2\ <\ +2.7$
$(Q_W^e/Q_W^{eo} = 1)$	90.0% $SS\ CL$	$-4.6\ <\ \mu_W/\mu_W^\circ - 2\ \equiv\ g_W - 2\ <\ +4.7$
	95.0% $SS\ CL$	$-5.3\ <\ \mu_W/\mu_W^\circ - 2\ \equiv\ g_W - 2\ <\ +5.4$
Q_W^e/Q_W^{eo}	68.3% $DS\ CL$	$1.0\ ^{+5.3}_{-4.9}\ (\boldsymbol{stat})\ \pm\ 0.7\ (\boldsymbol{syst})\ =\ 1.0\ ^{+5.9}_{-5.6}\ (\boldsymbol{stat}+\boldsymbol{syst})$
	68.3% $SS\ CL$	$-3.8\ <\ Q_W^e/Q_W^{eo} - 1\ \equiv\ q_W^e - 1\ <\ +4.1$
$(\mu_W/\mu_W^\circ = 2)$	90.0% $SS\ CL$	$-6.8\ <\ Q_W^e/Q_W^{eo} - 1\ \equiv\ q_W^e - 1\ <\ +7.1$
	95.0% $SS\ CL$	$-7.8\ <\ Q_W^e/Q_W^{eo} - 1\ \equiv\ q_W^e - 1\ <\ +8.1$
$<R_W>^2\ /\ \bar{\lambda}_W^2$	68.3% $DS\ CL$	$1.0\ ^{+3.4}_{-3.4}\ (\boldsymbol{stat})\ \pm\ 0.5\ (\boldsymbol{syst})\ =\ 1.0\ ^{+3.9}_{-3.9}\ (\boldsymbol{stat}+\boldsymbol{syst})$
	68.3% $SS\ CL$	$-2.6\ <\ <R_W^2>\ /\ \bar{\lambda}_W^2 - 1\ \equiv\ r_W^2 - 1\ <\ +2.7$
$(Q_W^e/Q_W^{eo} = 1)$	90.0% $SS\ CL$	$-4.6\ <\ <R_W^2>\ /\ \bar{\lambda}_W^2 - 1\ \equiv\ r_W^2 - 1\ <\ +4.7$
	95.0% $SS\ CL$	$-5.3\ <\ <R_W^2>\ /\ \bar{\lambda}_W^2 - 1\ \equiv\ r_W^2 - 1\ <\ +5.4$

Table 9.7: Combined Limits on W Boson EM Moments. The $\pm 1\sigma$, (68.3%) CL double-sided (DS) limits and the the 68.3%, 90.0% and 95.0% single-sided (SS) CL upper limits on μ_W/μ_W^o and Q_W^e/Q_W^{eo} are given. See text for further details.

Parameter	CL Range	Combined $e+\mu$ Limits
μ_W/μ_W^o	68.3% $DS\ CL$	$2.0\ ^{+3.2}_{-3.1}\ (\boldsymbol{stat}) \pm 0.5\ (\boldsymbol{syst}) = 2.0\ ^{+3.6}_{-3.6}\ (\boldsymbol{stat}+\boldsymbol{syst})$
	68.3% $SS\ CL$	$-2.4 < \mu_W/\mu_W^o - 2 \equiv g_W - 2 < +2.5$
$(Q_W^e/Q_W^{eo} = 1)$	90.0% $SS\ CL$	$-4.2 < \mu_W/\mu_W^o - 2 \equiv g_W - 2 < +4.2$
	95.0% $SS\ CL$	$-4.8 < \mu_W/\mu_W^o - 2 \equiv g_W - 2 < +4.9$
Q_W^e/Q_W^{eo}	68.3% $DS\ CL$	$1.0\ ^{+4.9}_{-4.5}\ (\boldsymbol{stat}) \pm 0.7\ (\boldsymbol{syst}) = 1.0\ ^{+5.6}_{-5.2}\ (\boldsymbol{stat}+\boldsymbol{syst})$
	68.3% $SS\ CL$	$-3.5 < Q_W^e/Q_W^{eo} - 1 \equiv q_W^e - 1 < +3.8$
$(\mu_W/\mu_W^o = 2)$	90.0% $SS\ CL$	$-6.1 < Q_W^e/Q_W^{eo} - 1 \equiv q_W^e - 1 < +6.4$
	95.0% $SS\ CL$	$-7.0 < Q_W^e/Q_W^{eo} - 1 \equiv q_W^e - 1 < +7.4$
$<R_W>^2 / \bar{\lambda}_W^2$	68.3% $DS\ CL$	$1.0\ ^{+3.2}_{-3.1}\ (\boldsymbol{stat}) \pm 0.5\ (\boldsymbol{syst}) = 1.0\ ^{+3.6}_{-3.6}\ (\boldsymbol{stat}+\boldsymbol{syst})$
	68.3% $SS\ CL$	$-2.4 < <R_W^2> / \bar{\lambda}_W^2 - 1 \equiv r_W^2 - 1 < +2.5$
$(Q_W^e/Q_W^{eo} = 1)$	90.0% $SS\ CL$	$-4.2 < <R_W^2> / \bar{\lambda}_W^2 - 1 \equiv r_W^2 - 1 < +4.2$
	95.0% $SS\ CL$	$-4.8 < <R_W^2> / \bar{\lambda}_W^2 - 1 \equiv r_W^2 - 1 < +4.9$

The unitarity limits discussed in Chapter 2 are shown in Figure 9.2 as a dotted ellipse, and a pair of dotted horizontally oriented segments of an ellipse, for the unitarity limits associated with WW and $W\gamma$ production respectively. The 90% and 95% CL limits on $\Delta\kappa$ and λ are outside the unitarity bounds associated with WW and $W\gamma$ production in certain regions of the $\Delta\kappa - \lambda$ plane, for $\Lambda_W = 1$ TeV. Note that the muon 95% CL contour limits on $\Delta\kappa - \lambda$ are within the unitarity limits for a compositeness scale of $\Lambda_W \simeq 850$ GeV.

For $W\gamma$, a compositeness scale $\Lambda_W = 10$ TeV and form factor power $n = 2$ was used in obtaining limits on $\Delta\kappa$ and λ, see Equation 2.3. As can be seen in Figure 9.4, the limits on anomalous $WW\gamma$ couplings are only slightly different if a compositeness scale of $\Lambda_W = 1$ TeV is chosen. If instead of $n = 2$, a form factor power of $n = 1$ had been chosen, the unitarity bounds on $\Delta\kappa$ and λ are more strict by a factor of ~ 4. The *experimental* limits are not significantly changed for $n = 1$.

The experimentally allowed region in $|\Delta\kappa| - \Lambda_W$ ($|\lambda| - \Lambda_W$) space is that which is below both the experimental curve (for 68%, 90% or 95% CL upper limit) and *both* the $W\gamma$ and W^+W^-

unitarity limit curves. As can be seen in Figure 9.4, the sensitivity limits on the compositeness scale are determined by the point where unitarity is saturated, i.e. the intersection of the experimental 68%, 90% or 95% CL upper limit with the lower of the $W\gamma$ or W^+W^- unitarity curve.

9.4 Comparison with Existing Limits on Anomalous $WW\gamma$ Couplings

Low-energy bounds on $\Delta\kappa$ and λ are quite model-dependent [57]. Non-SM loop contributions to the muon $(g_\mu - 2)$ anomaly imply [58, 59]

$$\left|\Delta\kappa \ln\left(\frac{\Lambda^2}{M_W^2}\right) + \frac{1}{3}\lambda\right| < 3.7 \tag{9.5}$$

where Λ is a cutoff to regulate divergences in the loop calculation. For $\Lambda = 1$ TeV, the muon $(g_\mu - 2)$ result constrains

$$|\Delta\kappa| < 0.7 \quad (\lambda = 0) \qquad\qquad |\lambda| < 11.1 \quad (\Delta\kappa = 0)$$

The factor of 1/3 in front of the λ parameter and associated bounds on λ depend on the regularization scheme used in the calculation (see first paper of reference [55]).

The only other direct measurement of $W\gamma$ has been done by the UA2 Collaboration, which has recently published limits on $\Delta\kappa$ and λ from an analysis of 13 pb^{-1} of $\bar{p}\,p \rightarrow e^\pm\nu\gamma$ electron data [60], where 16 $W\gamma$ candidate events were found. Their event selection required photons of

Muon $|\Delta\kappa|$ and $|\lambda|$ Limits vs. Λ_W

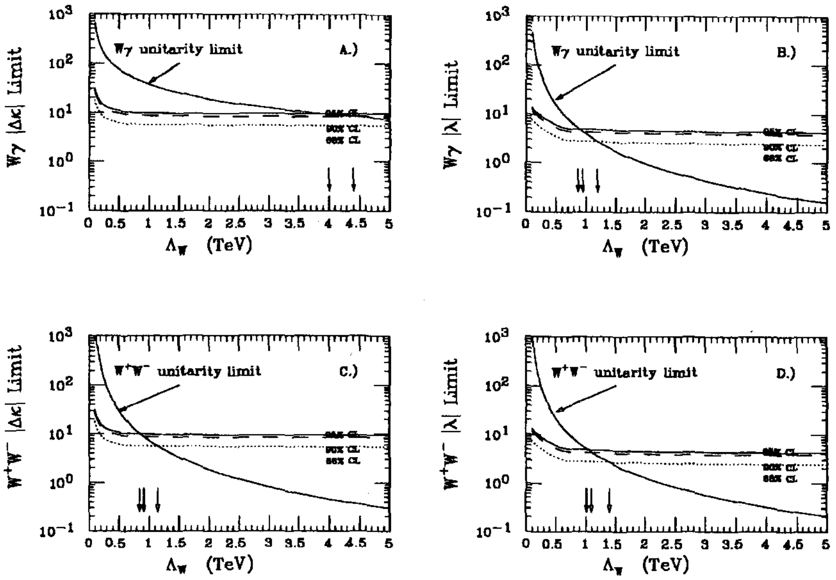

Combined e+μ $|\Delta\kappa|$ and $|\lambda|$ Limits vs. Λ_W

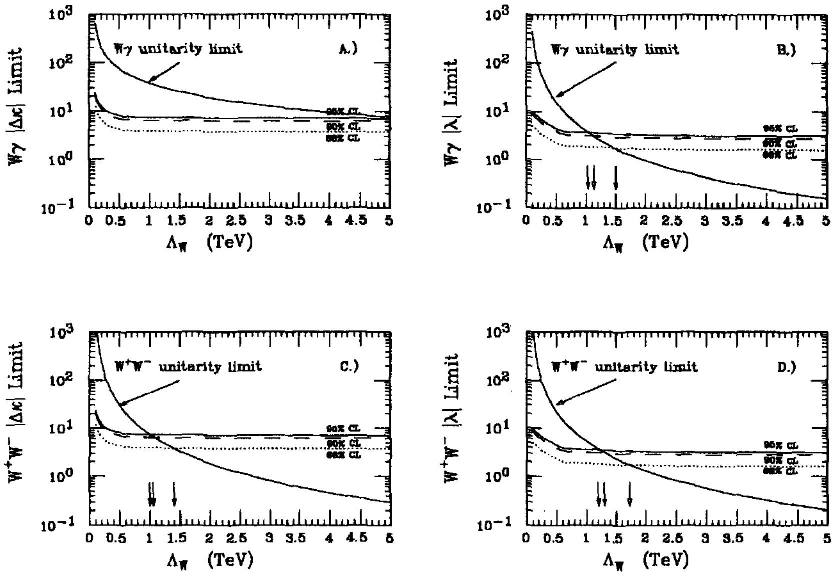

Figure 9.4: The top set of plots are for the muon channel, while the lower set of plots are for the combined $\mu + e$ channel. For anomalous $W\gamma$ couplings, the unitarity limit as a function of compositeness scale Λ_W for; (A) $|\Delta\kappa|$ (with $\lambda = 0$) (B) $|\lambda|$ (with $\Delta\kappa = 0$) For anomalous W^+W^- couplings, the unitarity limit as a function of compositeness scale Λ_W for; (C) $|\Delta\kappa|$ (with $\lambda = 0$) (D) $|\lambda|$ (with $\Delta\kappa = 0$) Also shown in each figure are the experimental muon (combined $\mu + e$) channel 1σ, 90.0% and 95.0% single-sided CL upper limits (dotted, dashed and solid curve, respectively) on $|\Delta\kappa|$ (or $|\lambda|$) as a function of compositeness scale Λ_W. The downward-pointing arrows indicate the value of Λ_W associated with the intersection of the experimental limits with the unitarity curve in each figure.

$E_T^\gamma > 4.5$ GeV and angular separation $\Delta\theta_{e\gamma}^{open} > 15^\circ$, with an expected background of 6.8 ± 1.0 events, for a $W\gamma$ signal of $9.2 \pm 4.0(stat) \pm 1.0(syst)$ events.

The UA2 Collaboration analyzed their data in two ways: first, similar to our method, comparing the number of signal events to the expected number of events, obtaining limits of:

$$\Delta\kappa = 0^{+4.6}_{-4.2} \pm 1.0\ (syst) \qquad (\lambda = 0) \tag{9.6}$$

$$\lambda = 0^{+2.9}_{-2.9} \pm 0.7\ (syst) \qquad (\kappa = 0) \tag{9.7}$$

with 95% CL limits of:

$$-6.3 < \Delta\kappa < 6.9 \qquad (\lambda = 0) \tag{9.8}$$

$$-4.4 < \lambda < 4.4 \qquad (\kappa = 0) \tag{9.9}$$

They also fitted the observed E_T^γ spectrum to that expected from the Monte Carlo, obtaining better limits of:

$$\Delta\kappa = 0^{+2.6}_{-2.2} \qquad (\lambda = 0) \tag{9.10}$$

$$\lambda = 0^{+1.7}_{-1.8} \qquad (\kappa = 0) \tag{9.11}$$

with a 95% CL limits of:

$$-4.5 < \Delta\kappa < 4.9 \qquad (\lambda = 0) \tag{9.12}$$

$$-3.6 < \lambda < 3.5 \qquad (\kappa = 0) \tag{9.13}$$

In order to be conservative in our limits on the anomalous $WW\gamma$ couplings, we chose not to use the E_T^γ spectrum fitting method for our determinations of the limits on the anomalous couplings. Significant additional studies of systematics would have to have been undertaken in order to obtain a result via this method, which would have been hard to confirm with the limited statistics of our data samples.

Note that at the $\sqrt{s} = 630$ GeV the interference effects between $\Delta\kappa$ and λ are such that the contour in the $\Delta\kappa$-λ plane of the 68% and 95% CL limit is rotated more with respect to the $\Delta\kappa$-λ axes than the our corresponding CL limit contours, as shown in Figure 9.5(left-hand figure).

The area enclosed by our muon channel limit contours is $\sim$ 30% greater than from the UA2 result, however the smaller rotation of our limit contours with respect to the $\Delta\kappa$ axis allows us to exclude part of the region allowed by the UA2 result. Likewise, the UA2 results exclude part of our allowed region.

9.4.1 Combined $W\gamma$ Results

The individual $\Delta\kappa$ and λ limits obtained from the the combined $\mu + e$ cross section results are listed in Table 9.4. The combined $\mu + e$ single sided 95% CL limit on $\Delta\kappa$ is $\sim$ 70% of the equivalent muon channel limit, and $\sim$ 90% of the equivalent electron channel limit. Comparing the plots of Figure 9.5, the combined $\mu + e$ channel 95% CL limit contour in the $\Delta\kappa - \lambda$ plane encloses approximately 55% of the area enclosed by the muon channel 95% CL limit contour.

The CDF combined $\mu + e$ channel $W\gamma$ limit contours enclose significantly less area of the $\Delta\kappa - \lambda$ plane than the UA2 results do. The CDF combined $\mu + e$ channel 95% limit contour in

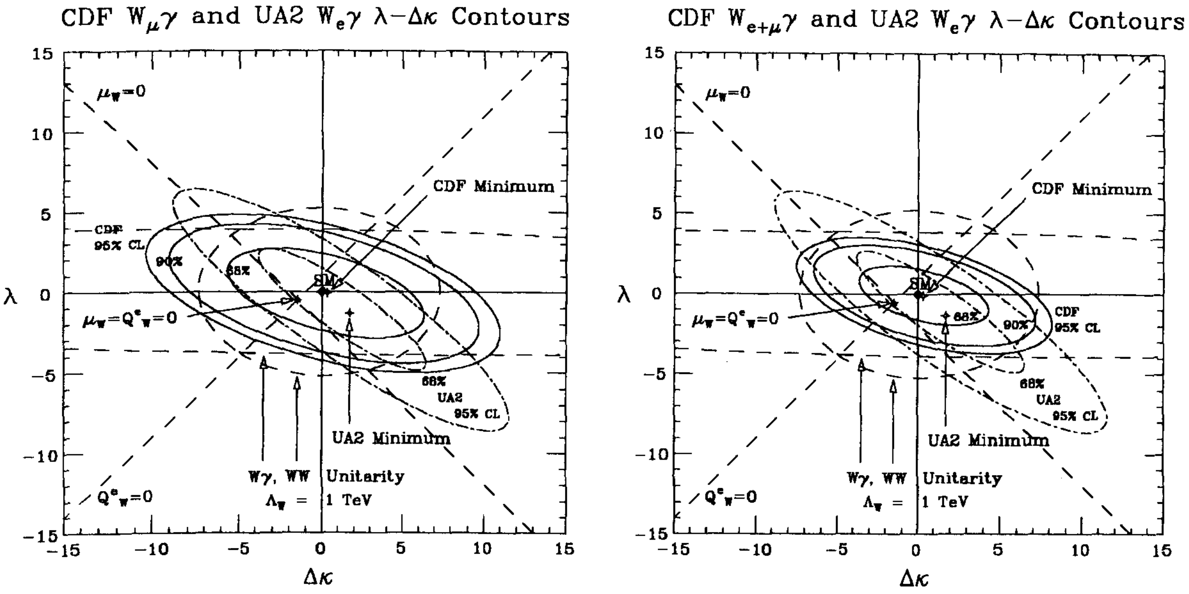

Figure 9.5: CDF and UA2 $\Delta\kappa - \lambda$ contour limits. The left hand plot is the CDF muon result channel result, while the right hand plot is the result from the combined $\mu + e$ channels. The solid curves show the CDF 1σ, 90.0% and 95.0% single-sided CL upper limits in the $\Delta\kappa - \lambda$ plane. The dot-dashed ellipses show the UA2 1σ and 95.0% single-sided CL upper limits in the $\Delta\kappa - \lambda$ plane. The different orientation of the CDF and UA2 contours relative to the $\Delta\kappa$ and λ axes is due to energy-dependent interference effects between these parameters in the overall invariant amplitude $\mathcal{M}_{W\gamma}$ for the $W + \gamma$ process. The CDF and UA2 global minima for the $\sigma \cdot B(W\gamma)$ surfaces are displaced from the SM prediction, due to energy-dependent $\Delta\kappa - \lambda$ interference effects. The μ_W/μ^0_W ($Q^e_W = 0$) and Q^e_W/Q^{eo}_W ($\mu_W = 0$) axes are indicated in this figure by orthogonal dashed lines. The W^+W^- and $W\gamma$ unitarity limits for a compositeness scale $\Lambda_W = 1$ TeV are indicated by dashed curves. See text for further details.

the $\Delta\kappa - \lambda$ plane encloses approximately 65% of the area enclosed by the UA2 95% CL limit contour.

As was the case in the muon channel results, the rotation of the CDF limit contour with respect to the $\Delta\kappa - \lambda$ axes is less than the UA2 limit contour, resulting in even more stringent limits on λ (with $\Delta\kappa = 0$) than would have been expected by simply comparing the respective area enclosed by the 95% CL limit contours.

9.5 Limits on $ZZ\gamma$ and $Z\gamma\gamma$ Anomalous Couplings

Direct limits on $ZZ\gamma$ and $Z\gamma\gamma$ couplings are obtained using similar methods as used to obtain direct limits on the anomalous $WW\gamma$ couplings. As previously mentioned, we explicitly obtain limits on only two of the possible anomalous coupling parameters for $ZZ\gamma$ and $Z\gamma\gamma$, the h^Z_{30} and h^Z_{40} anomalous $ZZ\gamma$ couplings.

In the case of $Z\gamma$, the dependence on the compositeness scale Λ_Z is much greater than in the $W\gamma$ case, so the limits on the anomalous couplings are obtained for three different Λ_Z values, $\Lambda_Z = 250, 500$ and 750 GeV.

The 1σ, 90% and 95% confidence level limits on the h^Z_{30} and h^Z_{40} parameters are listed in Table 9.8. Figure 9.6 shows the projections of the predicted $Z\gamma$ cross section on the h^Z_{30} and h^Z_{40} axes. The central value of the $\sigma \cdot BR(Z + \gamma)$ results is shown as a solid horizontal line in each figure, and the $\pm 1\sigma(stat + syst)$, 90% and 95% single sided confidence level upper limits are shown and labeled appropriately.

Figure 9.7a-c shows the muon channel 1σ, 90% and 95% single sided confidence level contours in the h^Z_{30}-h^Z_{40} and h^Z_{10}-h^Z_{20} planes, for the range of Λ_Z values, Λ_Z = 250, 500, and 750 GeV, for the anomalous $ZZ\gamma$ couplings. Figure 9.7d-f shows the muon channel 1σ 90% and 95% single sided confidence level contours in the h^Z_{30}-h^Z_{40} and h^Z_{10}-h^Z_{20} planes, for the range of Λ_Z values, Λ_Z = 250, 500, and 750 GeV for anomalous $Z\gamma\gamma$ couplings.

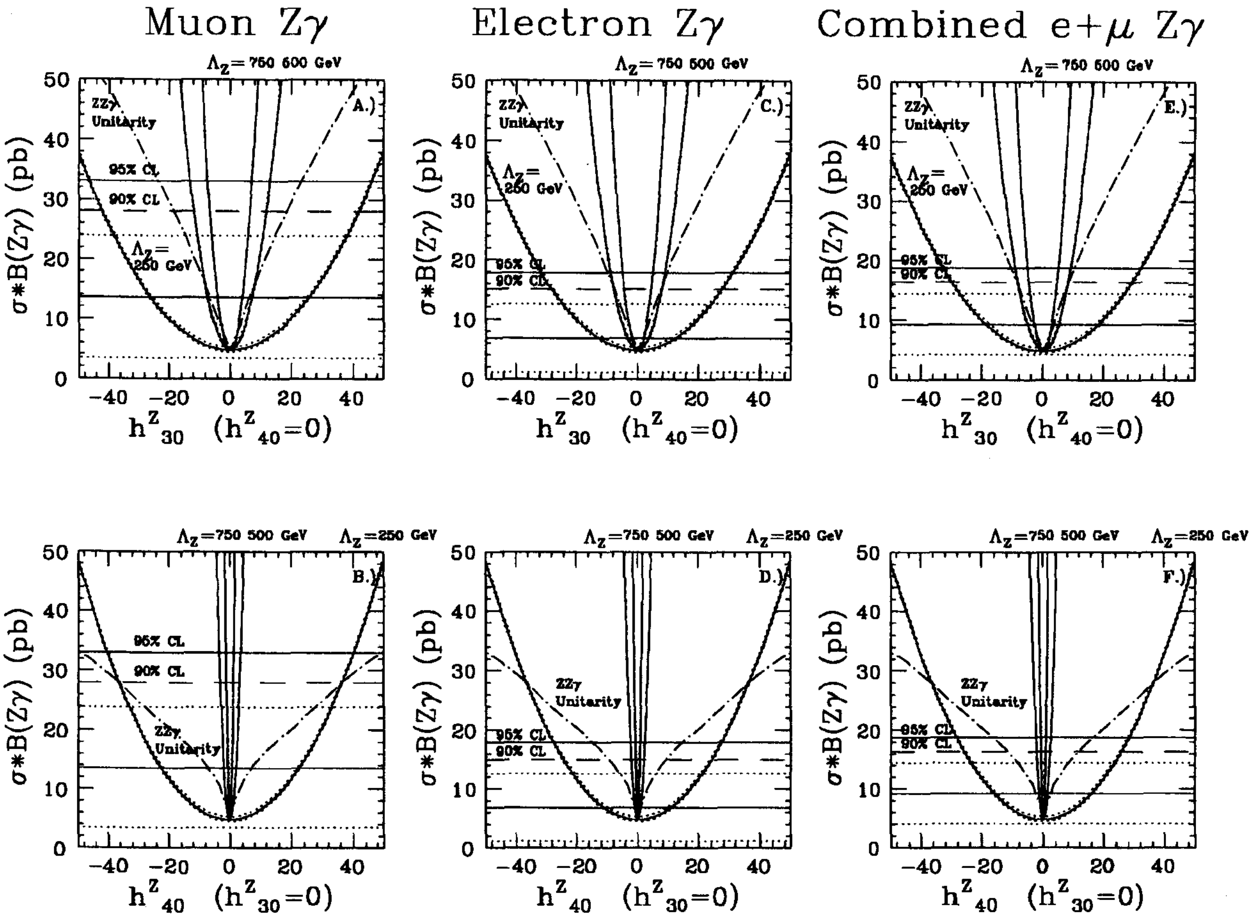

Figure 9.6: Limits on h^Z_{30} and h^Z_{40} (h^Z_{10} and h^Z_{20}) anomalous $ZZ\gamma$ couplings. Plots A),C), and E) show $\sigma \cdot B(Z\gamma)$ as a function of h^Z_{30} ($h^Z_{40} = 0$) for electron, muon and combined $\mu + e$ $Z\gamma$. Plots B),D), and F) show $\sigma \cdot B(Z\gamma)$ as a function of h^Z_{40} ($h^Z_{30} = 0$) for electron, muon and combined $\mu + e$ $Z\gamma$. For each of the figures, the unlabeled solid horizontal line is the central value for the measured $\sigma \cdot B(Z\gamma)$, while the dotted horizontal lines are the associated $\pm 1\sigma$ double-sided *stat* + *syst* uncertainty. The 90.0% and 95.0% single-sided CL upper limits on the measured $\sigma \cdot B(Z\gamma)$ are indicated by the appropriately labeled dashed and solid horizontal lines, respectively. The central values of the theoretical predictions for $\sigma \cdot B(Z\gamma)$ for compositeness scales $\Lambda_Z = 250$, 500, and 750 GeV as a function of h^Z_{30} (for $h^Z_{40} = 0$) or h^Z_{40} (for $h^Z_{30} = 0$) are shown as solid curves, with dotted curves for each as the $\pm 1\sigma$ common systematic uncertainty *differences* between the theoretical prediction and experimental measurement. The unitarity limit for the relevant anomalous $ZZ\gamma$ coupling is shown in each figure as a dotted-dash curve appropriately labeled. See text for further details.

Table 9.8: Muon $h^Z_{30} - h^Z_{40}$ ($h^Z_{10} - h^Z_{20}$) $ZZ\gamma$ limits. The $\pm 1\sigma$, (68.3%) CL double-sided (DS) limits and the the 68.3%, 90.0% and 95.0% single-sided (SS) CL upper limits on h^Z_{30}, h^Z_{10} (with $h^Z_{20}, h^Z_{40} = 0$) and h^Z_{40}, h^Z_{20} (with $h^Z_{30}, h^Z_{10} = 0$) are given. See text for further details.

Parameter	CL Range	$h^Z_{30} - h^Z_{40}$ ($h^Z_{10} - h^Z_{20}$) $ZZ\gamma$ Limits
$h^Z_{30},\ h^Z_{10}$	68.3% $DS\ CL$	$0.0^{+37.6}_{-37.8}(stat) \pm 0.7(syst) \ = \ 0.0^{+38.2}_{-38.5}(stat + syst)$
	68.3% $SS\ CL$	$-32.3 < h^Z_{30},\ h^Z_{10} < +32.0$
($h^Z_{40},\ h^Z_{20} = 0$)	90.0% $SS\ CL$	$-42.4 < h^Z_{30},\ h^Z_{10} < +42.1$
($\Lambda_Z = 250$ GeV)	95.0% $SS\ CL$	$-46.7 < h^Z_{30},\ h^Z_{10} < +46.4$
$h^Z_{40},\ h^Z_{20}$	68.3% $DS\ CL$	$0.0^{+32.8}_{-32.8}(stat) \pm 0.5(syst) \ = \ 0.0^{+33.3}_{-33.3}(stat + syst)$
	68.3% $SS\ CL$	$-28.0 < h^Z_{40},\ h^Z_{20} < +27.9$
($h^Z_{30},\ h^Z_{10} = 0$)	90.0% $SS\ CL$	$-36.8 < h^Z_{40},\ h^Z_{20} < +36.7\dagger$
($\Lambda_Z = 250$ GeV)	95.0% $SS\ CL$	$-40.5 < h^Z_{40},\ h^Z_{20} < +40.4\dagger$
$h^Z_{30},\ h^Z_{10}$	68.3% $DS\ CL$	$0.0^{+10.7}_{-10.6}(stat) \pm 0.2(syst) \ = \ 0.0^{+10.9}_{-10.8}(stat + syst)$
	68.3% $SS\ CL$	$-9.0 < h^Z_{30},\ h^Z_{10} < +9.1\dagger$
($h^Z_{40},\ h^Z_{20} = 0$)	90.0% $SS\ CL$	$-11.9 < h^Z_{30},\ h^Z_{10} < +12.0\dagger$
($\Lambda_Z = 500$ GeV)	95.0% $SS\ CL$	$-13.1 < h^Z_{30},\ h^Z_{10} < +13.2\dagger$
$h^Z_{40},\ h^Z_{20}$	68.3% $DS\ CL$	$0.0\ ^{+2.9}_{-2.8}(stat) \pm 0.1(syst) \ = \ 0.0\ ^{+2.9}_{-2.9}(stat + syst)$
	68.3% $SS\ CL$	$-2.4 < h^Z_{40},\ h^Z_{20} < +2.4\dagger$
($h^Z_{30},\ h^Z_{10} = 0$)	90.0% $SS\ CL$	$-3.2 < h^Z_{40},\ h^Z_{20} < +3.2\dagger$
($\Lambda_Z = 500$ GeV)	95.0% $SS\ CL$	$-3.5 < h^Z_{40},\ h^Z_{20} < +3.5\dagger$
$h^Z_{30},\ h^Z_{10}$	68.3% $DS\ CL$	$0.0^{+5.9}_{-5.9}(stat) \pm 0.1(syst) \ = \ 0.0^{+6.0}_{-6.0}(stat + syst)$
	68.3% $SS\ CL$	$-5.0 < h^Z_{30},\ h^Z_{10} < +5.0\dagger$
($h^Z_{40},\ h^Z_{20} = 0$)	90.0% $SS\ CL$	$-6.6 < h^Z_{30},\ h^Z_{10} < +6.6\dagger$
($\Lambda_Z = 750$ GeV)	95.0% $SS\ CL$	$-7.3 < h^Z_{30},\ h^Z_{10} < +7.3\dagger$
$h^Z_{40},\ h^Z_{20}$	68.3% $DS\ CL$	$0.0^{+1.0}_{-1.0}(stat) \pm 0.1(syst) \ = \ 0.0^{+1.0}_{-1.0}(stat + syst)$
	68.3% $SS\ CL$	$-0.9 < h^Z_{40},\ h^Z_{20} < +0.9\dagger$
($h^Z_{30},\ h^Z_{10} = 0$)	90.0% $SS\ CL$	$-1.1 < h^Z_{40},\ h^Z_{20} < +1.1\dagger$
($\Lambda_Z = 750$ GeV)	95.0% $SS\ CL$	$-1.2 < h^Z_{40},\ h^Z_{20} < +1.2\dagger$

† Exceeds unitarity limit

Table 9.9: Electron $h^Z_{30} - h^Z_{40}$ $(h^Z_{10} - h^Z_{20})$ $ZZ\gamma$ limits. The $\pm 1\sigma$, (68.3%) CL double-sided (DS) limits and the the 68.3%, 90.0% and 95.0% single-sided (SS) CL upper limits on h^Z_{30}, h^Z_{10} (with $h^Z_{20}, h^Z_{40} = 0$) and h^Z_{40}, h^Z_{20} (with $h^Z_{30}, h^Z_{10} = 0$) are given. See text for further details.

Parameter	CL Range	$h^Z_{30} - h^Z_{40}$ $(h^Z_{10} - h^Z_{20})$ Limits
$h^Z_{30},\ h^Z_{10}$	68.3% $DS\ CL$	$0.0^{+24.0}_{-24.3}(stat) \pm 0.6(syst) = 0.0^{+24.6}_{-24.8}(stat + syst)$
	68.3% $SS\ CL$	$-19.7 < h^Z_{30},\ h^Z_{10} < +19.4$
$(h^Z_{40},\ h^Z_{20} = 0)$	90.0% $SS\ CL$	$-28.4 < h^Z_{30},\ h^Z_{10} < +28.1$
$(\Lambda_Z = 250$ GeV$)$	95.0% $SS\ CL$	$-32.0 < h^Z_{30},\ h^Z_{10} < +31.7$
$h^Z_{40},\ h^Z_{20}$	68.3% $DS\ CL$	$0.0^{+21.0}_{-21.0}(stat) \pm 0.5(syst) = 0.0^{+21.4}_{-21.5}(stat + syst)$
	68.3% $SS\ CL$	$-17.0 < h^Z_{40},\ h^Z_{20} < +17.0$
$(h^Z_{30},\ h^Z_{10} = 0)$	90.0% $SS\ CL$	$-24.6 < h^Z_{40},\ h^Z_{20} < +24.5$
$(\Lambda_Z = 250$ GeV$)$	95.0% $SS\ CL$	$-27.7 < h^Z_{40},\ h^Z_{20} < +27.6$
$h^Z_{30},\ h^Z_{10}$	68.3% $DS\ CL$	$0.0\ ^{+6.9}_{-6.7}(stat) \pm 0.2(syst) = 0.0\ ^{+7.0}_{-6.9}(stat + syst)$
	68.3% $SS\ CL$	$-5.4 < h^Z_{30},\ h^Z_{10} < +5.5$
$(h^Z_{40},\ h^Z_{20} = 0)$	90.0% $SS\ CL$	$-7.9 < h^Z_{30},\ h^Z_{10} < +8.0$
$(\Lambda_Z = 500$ GeV$)$	95.0% $SS\ CL$	$-8.9 < h^Z_{30},\ h^Z_{10} < +9.0$†
$h^Z_{40},\ h^Z_{20}$	68.3% $DS\ CL$	$0.0\ ^{+1.8}_{-1.8}(stat) \pm 0.1(syst) = 0.0\ ^{+1.9}_{-1.8}(stat + syst)$
	68.3% $SS\ CL$	$-1.5 < h^Z_{40},\ h^Z_{20} < +1.5$†
$(h^Z_{30},\ h^Z_{10} = 0)$	90.0% $SS\ CL$	$-2.1 < h^Z_{40},\ h^Z_{20} < +2.1$†
$(\Lambda_Z = 500$ GeV$)$	95.0% $SS\ CL$	$-2.4 < h^Z_{40},\ h^Z_{20} < +2.4$†
$h^Z_{30},\ h^Z_{10}$	68.3% $DS\ CL$	$0.0^{+3.8}_{-3.8}(stat) \pm 0.1(syst) = 0.0^{+3.9}_{-3.9}(stat + syst)$
	68.3% $SS\ CL$	$-3.1 < h^Z_{30},\ h^Z_{10} < +3.1$†
$(h^Z_{40},\ h^Z_{20} = 0)$	90.0% $SS\ CL$	$-4.4 < h^Z_{30},\ h^Z_{10} < +4.4$†
$(\Lambda_Z = 750$ GeV$)$	95.0% $SS\ CL$	$-5.0 < h^Z_{30},\ h^Z_{10} < +5.0$†
$h^Z_{40},\ h^Z_{20}$	68.3% $DS\ CL$	$0.0^{+0.6}_{-0.6}(stat) \pm 0.1(syst) = 0.0^{+0.7}_{-0.7}(stat + syst)$
	68.3% $SS\ CL$	$-0.5 < h^Z_{40},\ h^Z_{20} < +0.5$†
$(h^Z_{30},\ h^Z_{10} = 0)$	90.0% $SS\ CL$	$-0.8 < h^Z_{40},\ h^Z_{20} < +0.8$†
$(\Lambda_Z = 750$ GeV$)$	95.0% $SS\ CL$	$-0.9 < h^Z_{40},\ h^Z_{20} < +0.9$†

† Exceeds unitarity limit

Table 9.10: Combined $e + \mu$ $h^Z_{30} - h^Z_{40}$ $(h^Z_{10} - h^Z_{20})$ $ZZ\gamma$ Limits. The $\pm 1\sigma$, (68.3%) CL double-sided (DS) limits and the the 68.3%, 90.0% and 95.0% single-sided (SS) CL upper limits on h^Z_{30}, h^Z_{10} (with $h^Z_{20}, h^Z_{40} = 0$) and h^Z_{40}, h^Z_{20} (with $h^Z_{30}, h^Z_{10} = 0$) are given. See text for further details.

Parameter	CL Range	$h^Z_{30} - h^Z_{40}$ $(h^Z_{10} - h^Z_{20})$ $ZZ\gamma$ Limits
h^Z_{30}, h^Z_{10}	68.3% DS CL	$0.0^{+26.8}_{-27.1}(stat) \pm 0.6(syst) = 0.0^{+27.4}_{-27.7}(stat + syst)$
	68.3% SS CL	$-23.2 < h^Z_{30}, h^Z_{10} < +22.9$
(h^Z_{40}, $h^Z_{20} = 0$)	90.0% SS CL	$-30.2 < h^Z_{30}, h^Z_{10} < +29.9$
(Λ_Z = 250 GeV)	95.0% SS CL	$-33.1 < h^Z_{30}, h^Z_{10} < +32.8$
h^Z_{40}, h^Z_{20}	68.3% DS CL	$0.0^{+23.4}_{-23.5}(stat) \pm 0.5(syst) = 0.0^{+23.9}_{-24.0}(stat + syst)$
	68.3% SS CL	$-20.0 < h^Z_{40}, h^Z_{20} < +20.0$
(h^Z_{30}, $h^Z_{10} = 0$)	90.0% SS CL	$-26.1 < h^Z_{40}, h^Z_{20} < +26.1$
(Λ_Z = 250 GeV)	95.0% SS CL	$-28.6 < h^Z_{40}, h^Z_{20} < +28.6$
h^Z_{30}, h^Z_{10}	68.3% DS CL	$0.0^{+7.7}_{-7.5}(stat) \pm 0.2(syst) = 0.0^{+7.8}_{-7.7}(stat + syst)$
	68.3% SS CL	$-6.4 < h^Z_{30}, h^Z_{10} < +6.5$
(h^Z_{40}, $h^Z_{20} = 0$)	90.0% SS CL	$-8.4 < h^Z_{30}, h^Z_{10} < +8.5$
(Λ_Z = 500 GeV)	95.0% SS CL	$-9.2 < h^Z_{30}, h^Z_{10} < +9.4$†
h^Z_{40}, h^Z_{20}	68.3% DS CL	$0.0^{+2.0}_{-2.0}(stat) \pm 0.1(syst) = 0.0^{+2.1}_{-2.1}(stat + syst)$
	68.3% SS CL	$-1.7 < h^Z_{40}, h^Z_{20} < +1.7$†
(h^Z_{30}, $h^Z_{10} = 0$)	90.0% SS CL	$-2.3 < h^Z_{40}, h^Z_{20} < +2.3$†
(Λ_Z = 500 GeV)	95.0% SS CL	$-2.5 < h^Z_{40}, h^Z_{20} < +2.5$†
h^Z_{30}, h^Z_{10}	68.3% DS CL	$0.0^{+4.2}_{-4.2}(stat) \pm 0.1(syst) = 0.0^{+4.3}_{-4.3}(stat + syst)$
	68.3% SS CL	$-3.6 < h^Z_{30}, h^Z_{10} < +3.6$†
(h^Z_{40}, $h^Z_{20} = 0$)	90.0% SS CL	$-4.7 < h^Z_{30}, h^Z_{10} < +4.7$†
(Λ_Z = 750 GeV)	95.0% SS CL	$-5.1 < h^Z_{30}, h^Z_{10} < +5.1$†
h^Z_{40}, h^Z_{20}	68.3% DS CL	$0.0^{+0.7}_{-0.7}(stat) \pm 0.1(syst) = 0.0^{+0.7}_{-0.7}(stat + syst)$
	68.3% SS CL	$-0.6 < h^Z_{40}, h^Z_{20} < +0.6$†
(h^Z_{30}, $h^Z_{10} = 0$)	90.0% SS CL	$-0.8 < h^Z_{40}, h^Z_{20} < +0.8$†
(Λ_Z = 750 GeV)	95.0% SS CL	$-0.9 < h^Z_{40}, h^Z_{20} < +0.9$†

† Exceeds unitarity limit

The $Z\gamma$ unitarity constraints discussed in Chapter 2 are indicated on Figure 9.7 as the dotted-ellipses. It can be seen that the experimental limits obtained are sensitive to a Λ_Z compositeness scale (with the assumed generalized form factor and form factor powers, Equation 2.11) of about $\sim 300 - 400$ GeV.

9.6 Limits on the Transition Moments of the Z Boson

Similar to the classical parameters we defined for the W boson, we define and calculate the numerical values of the following parameters, for the Z boson;

$$\begin{aligned}
d^{\circ}_{Z_T} &= -e\left(\frac{\hbar}{2M_Z c}\right) = -\tfrac{1}{2}e\,\bar{\lambda}_Z &&= -1.0820 \pm 0.0001 \times 10^{-3}\ e - \mathrm{fm} \\
Q^{m\circ}_{Z_T} &= \left(\frac{e\hbar^2}{M_Z^2 c}\right) &&= 1.4038 \pm 0.0002 \times 10^{-18}\ \mathrm{MeV - fm/T} \\
\mu^{\circ}_{Z_T} &= -\left(\frac{e\hbar}{2M_Z}\right) &&= -3.2437 \pm 0.0003 \times 10^{-16}\ \mathrm{MeV/T} \\
Q^{e\circ}_{Z_T} &= e\left(\frac{\hbar}{M_Z c}\right)^2 = e\,\bar{\lambda}_Z^2 &&= 4.6828 \pm 0.0007 \times 10^{-6}\ e - \mathrm{fm}^2 \\
\bar{\lambda}_Z &= \left(\frac{\hbar}{M_Z c}\right) &&= 2.1640 \pm 0.0002 \times 10^{-3}\ \mathrm{fm}
\end{aligned}$$

where $\bar{\lambda}_Z$ is the reduced Compton wavelength of the Z boson.

To facilitate examining the deviation of the higher order EM transistion moments of the Z boson from their Standard Model values, we define the following dimensionless quantities for the Z boson:

$$\delta_{Z_T} \equiv \frac{d_{Z_T}}{d^{\circ}_{Z_T}} = \sqrt{2}\left(\frac{k^2}{M_Z^2}\right)\left(h^Z_{30} - h^Z_{40}\right) \tag{9.14}$$

$$q^m_{Z_T} \equiv \frac{Q^m_{Z_T}}{Q^{m\circ}_{Z_T}} = \sqrt{10}\left(2h^Z_{30}\right) \tag{9.15}$$

$$g_{Z_T} \equiv \frac{\mu_{Z_T}}{\mu^{\circ}_{Z_T}} = \sqrt{2}\left(\frac{k^2}{M_Z^2}\right)\left(h^Z_{10} - h^Z_{20}\right) \tag{9.16}$$

$$q^e_{Z_T} \equiv \frac{Q^e_{Z_T}}{Q^{e\circ}_{Z_T}} = \sqrt{10}\left(2h^Z_{10}\right) \tag{9.17}$$

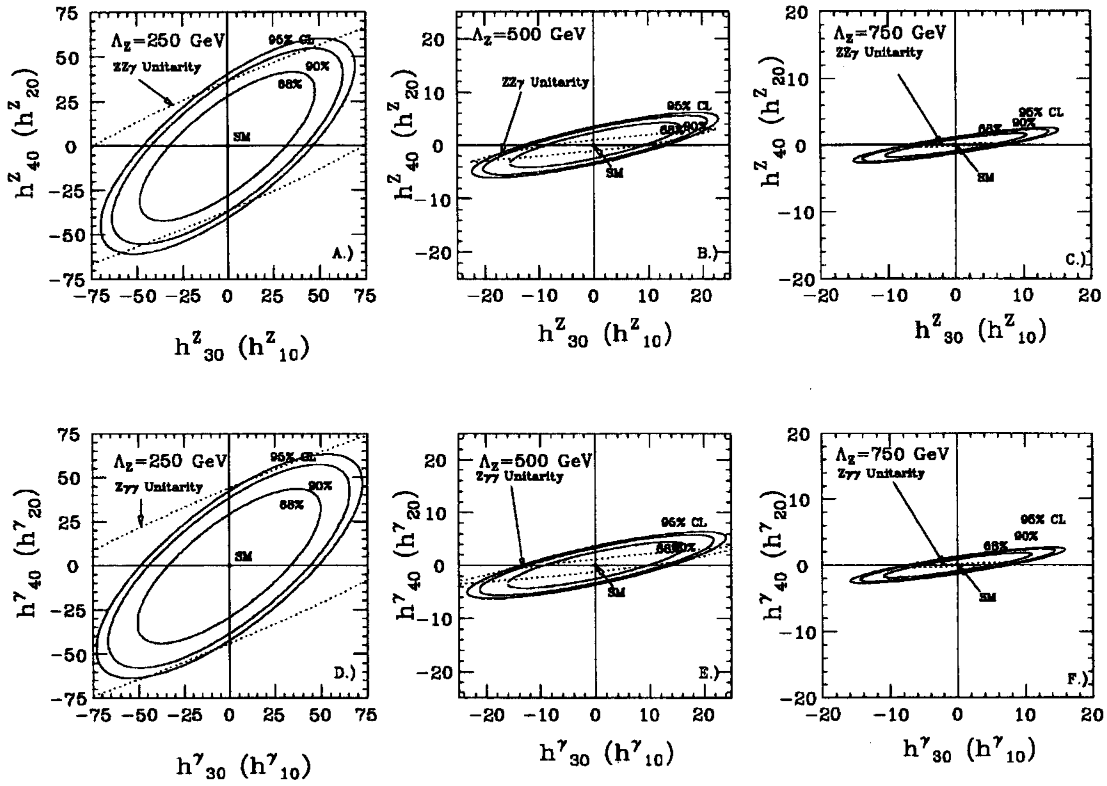

Figure 9.7: Figures (A)-(C) show the limits for muon $Z\gamma$ in the $h_{30}^V - h_{40}^V$ ($h_{10}^V - h_{20}^V$) plane. The solid ellipses show the 1σ, 90.0% and 95.0% single-sided CL upper limits in the $h_{30}^V - h_{40}^V/h_{10}^V - h_{20}^V$ ($V = Z, \gamma$) plane for anomalous $ZZ\gamma$ ($Z\gamma\gamma$) couplings. Figures (A)-(C) and (D)-(F) use $\Lambda_Z = 250$, 500, 750 GeV, respectively. The $ZZ\gamma$ and $Z\gamma\gamma$ unitarity limits for the relevant compositeness scale Λ_Z are indicated by dotted curves in Figures (A)-(C) and (D)-(F) respectively. See text for further details.

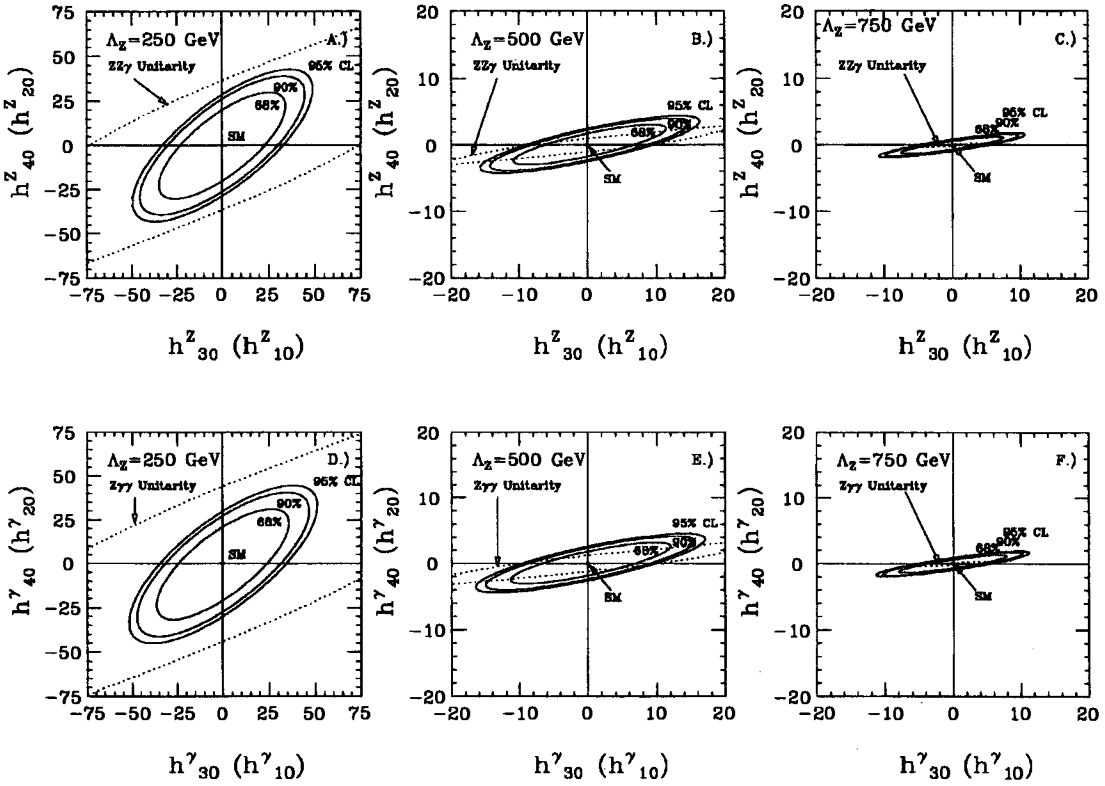

Figure 9.8: Figures (A)-(C) show the limits for $\mu + e$ $Z\gamma$ in the $h^V_{30} - h^V_{40}$ ($h^V_{10} - h^V_{20}$) plane. The solid ellipses show the $\mu + e$ 1σ, 90.0% and 95.0% single-sided CL upper limits in the $h^V_{30} - h^V_{40}/h^V_{10} - h^V_{20}$ ($V = Z, \gamma$) plane for anomalous $ZZ\gamma$ ($Z\gamma\gamma$) couplings. Figures (A)-(C) and (D)-(F) use $\Lambda_Z = 250$, 500, 750 GeV, respectively. The $ZZ\gamma$ and $Z\gamma\gamma$ unitarity limits for the relevant compositeness scale Λ_Z are indicated by dotted curves in Figures (A)-(C) and (D)-(F) respectively. See text for further details.

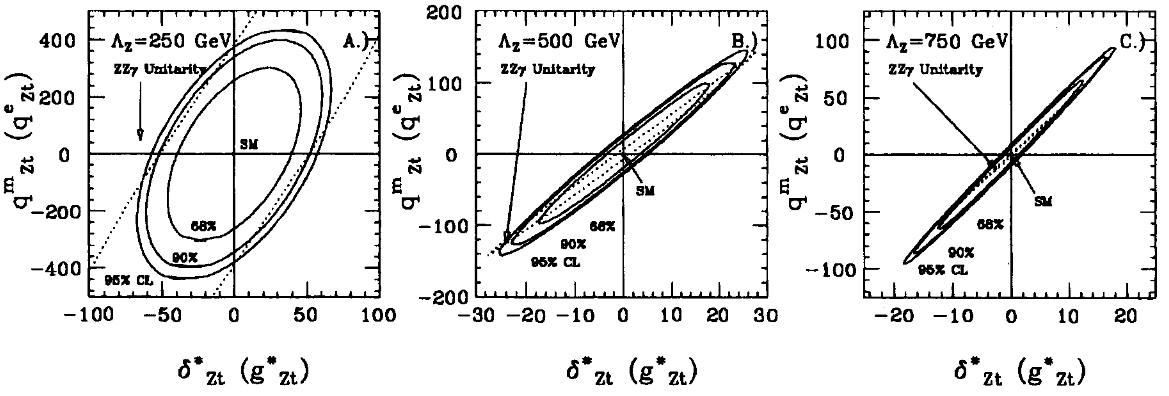

Figure 9.9: Limits on the muon channel $Z\gamma$ transition moments.

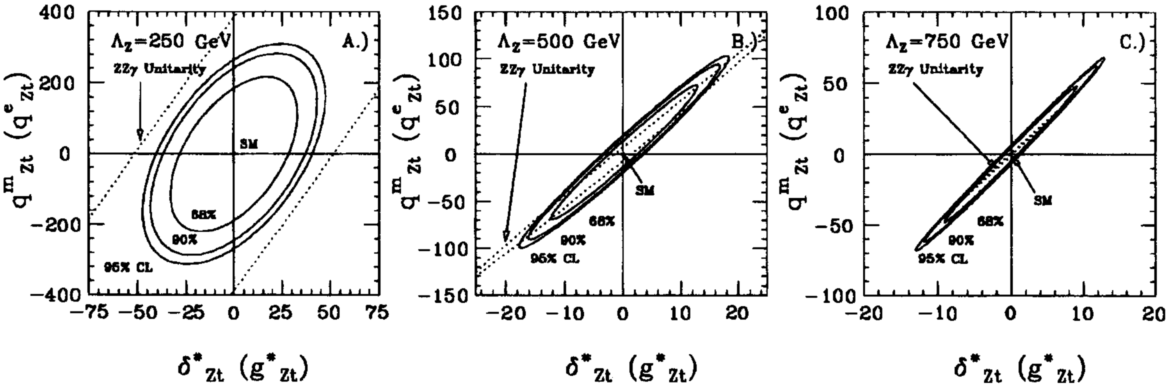

Figure 9.10: Limits on the combined $\mu + e$ channel $Z\gamma$ transition moments.

(9.18)

With regard to setting limits on the traditional transition moments associated with well defined initial and final quantum states, the factor k^2/M_Z^2 is experimentally ill-defined due to the nature of the $Z\gamma$ process. Thus we define the following substitution variables:

$$\delta^*_{Z_T} \equiv \delta_{Z_T}\left[\frac{M_Z^2}{k^2}\right] = \left[\frac{d_{Z_T}}{d^{\circ}_{Z_T}}\right]\left[\frac{M_Z^2}{k^2}\right] = \sqrt{2}\left(h^Z_{30} - h^Z_{40}\right) \tag{9.19}$$

$$g^*_{Z_T} \equiv g_{Z_T}\left[\frac{M_Z^2}{k^2}\right] = \left[\frac{\mu_{Z_T}}{\mu^{\circ}_{Z_T}}\right]\left[\frac{M_Z^2}{k^2}\right] = \sqrt{2}\left(h^Z_{10} - h^Z_{20}\right) \tag{9.20}$$

See Figures 9.9 and 9.10. Thus the dimensionless transition moments simply reduce to linear combination of the h_{i0} parameters. Then the limits on these transition moments are simply the limits on the h_{i0} anomalous couplings (taken one at a time) scaled by a constant factor of $\sqrt{2}$ or $2\sqrt{10}$.

For $Z\gamma$ the anomalous contributions to the helicity amplitudes are of higher order than those in the $W\gamma$ case, resulting in a much greater sensitivity to the compositeness scale Λ_Z.

9.7 Comparison with Existing Limits on Anomalous $ZZ\gamma/Z\gamma\gamma$ Couplings

Low-energy bounds on anomalous $ZZ\gamma$ and $Z\gamma\gamma$ couplings due to non-SM loop contributions to the muon $(g_\mu - 2)$ anomaly have been considered in Reference [61]. Only $Z\gamma\gamma$ couplings are found to give a non-zero contribution. For $h^\gamma_{40} = 0$, the muon $(g_\mu - 2)$ constraint implies

$$\left| h^\gamma_{30} \ln\left(\frac{\Lambda^2}{M_Z^2}\right) \right| < 9.0 \tag{9.21}$$

where Λ is a cutoff to regulate the divergence in the loop calculation. For $\Lambda = 250,\ 500,\ 750$ GeV, the muon $(g_\mu - 2)$ result constrains $|h^\gamma_{30}| < 4.5,\ 2.6,\ 2.1$, respectively. It should be noted that these bounds also depend on the regularization scheme used in the calculation.

The L3 Collaboration has recently obtained an experimental upper limit on the h^Z_3 form factor from a measurement of the cross section for the process $e^+e^- \to Z^0 \to \nu\bar{\nu}\gamma$ [62]. From the absence of an excess of such events in the Z resonance region from 11.2 pb^{-1} data, for

$E_\gamma > \frac{1}{2}E_{beam}$ they obtain a limit on the h_3^Z form factor of:

$$\left| h_3^Z(P^2 = M_Z^2,\ q_1^2 < M_Z^2,\ q_2^2 = 0) \right| < 1.6 \ \ (95\%\ CL) \tag{9.22}$$

Translating this result into limits on the h_{30}^Z parameter, using equation (2.11) with a generalized form-factor power of $n = 3$, the L3 result is $|h_{30}^Z| < 2.3,\ 1.8,\ 1.7\ \ (95\%\ CL)$, for $\Lambda_Z = 250,\ 500,\ 750$ GeV, respectively. The L3 h_{30}^Z results are well within the $|h_{30}^Z|$ unitarity limit for the assumed values of Λ_Z. Unitarity is violated for $\Lambda_Z > 840$ GeV.

The L3 $Z \rightarrow \nu\bar{\nu}\gamma$ results are sensitive only to anomalous $ZZ\gamma$ couplings, and place no constraints on anomalous $Z\gamma\gamma$ couplings. The CDF limits on anomalous $Z\gamma\gamma$ couplings from obtained from direct measurement of the $\sigma \cdot B(Z_\ell + \gamma)$ are therefore unique in this regard.

9.7.1 Combined $Z\gamma$ Results

For $Z\gamma$, Tables 9.8 and 9.10 and Figures 9.7 and Figure 9.8 show the effects of combining the muon and electron channel results.

Comparing the plots of Figure 9.7 with the equivalent plots in Figure 9.8 shows a decrease in the enclosed area of the limit contours for the combined $\mu + e$ results versus the muon channel results(See Table 6.5). As in the $W\gamma$ case, the sensitivity limits on the compositeness scale Λ_Z are determined by the intersection of the experimental 68%, 90% and 95% CL upper limits, and the lower of the $ZZ\gamma$ ($Z\gamma$) unitarity curve, see Figure 9.11. For saturation of unitarity, these combined results are sensitive to a compositeness scale $\Lambda_Z \simeq 300 - 500$ GeV at 95% CL.

Muon $|h_{i0}|$ Limits vs. Λ_Z

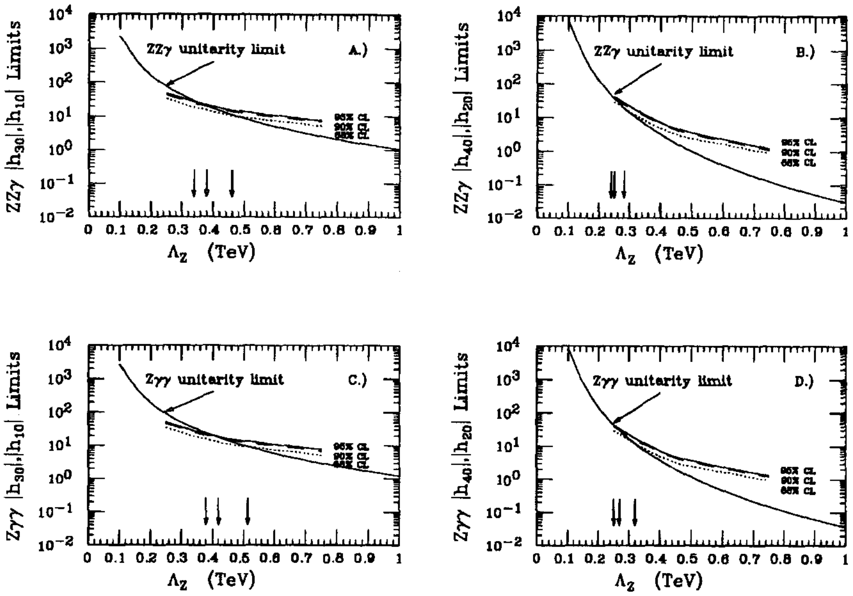

Combined e+μ $|h_{i0}|$ Limits vs. Λ_Z

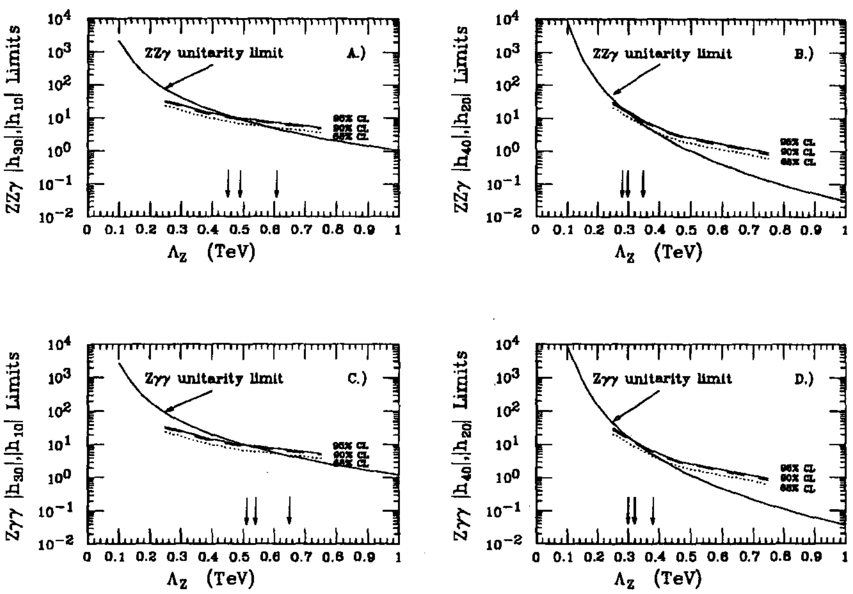

Figure 9.11: Unitarity limits as a function of Λ_Z for anomalous $ZZ\gamma$ and $Z\gamma\gamma$ couplings. The top set of plots are for the muon channel results, while the bottom set of plots are for the combined $\mu + e$ channel. The unitarity limits as a function of compositeness scale Λ_Z for anomalous $ZZ\gamma$ couplings, (A) $|h^Z_{30}|$, $|h^Z_{10}|$ (with $h^Z_{20}, h^Z_{40} = 0$), (B) $|h^Z_{40}|$, $|h^Z_{20}|$(with $h^Z_{30}, h^Z_{10} = 0$). The unitarity limits as a function of compositeness scale Λ_Z for anomalous $Z\gamma\gamma$ couplings, (C) $|h^\gamma_{30}|$, $|h^\gamma_{10}|$(with $h^Z_{20}, h^Z_{40} = 0$), (D) $|h^\gamma_{40}|$, $|h^\gamma_{20}|$(with $h^Z_{30}, h^Z_{10} = 0$). Also shown in each figure are the muon channel experimental 1σ, 90.0% and 95.0% single-sided CL upper limits (dotted, dashed and solid curve, respectively) on $|h^V_{30}|$, $|h^V_{10}|$ (or $|h^V_{40}|$, $|h^V_{20}|$) where $V = Z$, γ as a function of compositeness scale Λ_Z. The downward-pointing arrows indicate the value of Λ_Z associated with the intersection of the experimental limits with the unitarity curve in each figure.

Chapter 10

Conclusions

We have analyzed the $3.54 \pm 0.24\ \mathrm{pb}^{-1}$ of inclusive muon W and Z data from the '88-'89 run, and have obtained $W\gamma$ and $Z\gamma$ candidate samples whose statistics are such that they are compatible with the SM predictions and background expectations. For central $W\gamma$ with $E_T^\gamma > 5.0$ GeV and $\Delta R_{\ell\gamma} > 0.7$, we observe 5 muon $W\gamma$ candidates and 2 muon $Z\gamma$ candidates. The electron channel analysis found 8 electron $W\gamma$ and 2 electron $Z\gamma$ candidates, in $4.05 \pm 0.28\ \mathrm{pb}^{-1}$ of data, using identical photon selection requirements.

From these events the measured $\sigma \cdot B(W\gamma)$ and $\sigma \cdot B(Z\gamma)$ for the muon, electron, and combined $\mu + e$ samples are:

$$\begin{aligned}
\sigma \cdot B(W\gamma)_\mu &= 19.4^{+18.3}_{-17.9} \quad (stat + syst)\ \mathrm{pb} \\
\sigma \cdot B(W\gamma)_e &= 17.0^{+13.7}_{-13.4} \quad (stat + syst)\ \mathrm{pb} \\
\sigma \cdot B(W\gamma)_{e+\mu} &= 17.9^{+11.1}_{-10.7} \quad (stat + syst)\ \mathrm{pb} \\
\sigma \cdot B(W\gamma)_{SM} &= 19.0^{+\ 3.3}_{-\ 0.9} \quad (stat + syst)\ \mathrm{pb}
\end{aligned}$$

$$\sigma \cdot B(Z\gamma)_{\mu} = 13.6^{+10.3}_{-10.1} \quad (stat + syst) \text{ pb}$$

$$\sigma \cdot B(Z\gamma)_{e} = 6.8^{+\,5.7}_{-\,5.7} \quad (stat + syst) \text{ pb}$$

$$\sigma \cdot B(Z\gamma)_{e+\mu} = 9.2^{+\,5.2}_{-\,5.1} \quad (stat + syst) \text{ pb}$$

$$\sigma \cdot B(Z\gamma)_{SM} = 4.7^{+\,0.7}_{-\,0.2} \quad (stat + syst) \text{ pb}$$

Three new cross section ratio results were obtained, along with the previous CDF measurements of the W/Z cross section ratio. The muon channel, and combined $\mu + e$ channel results are:

Cross section Ratio	$\mathcal{R}\ \mu_{\text{Experiment}}$	$\mathcal{R}\ e_{\text{Experiment}}$	$\mathcal{R}\ \mu + e_{\text{Experiment}}$	$\mathcal{R}_{\text{SM Predicted}}$
$\mathcal{R}(W\gamma/W)_{\ell}$	$0.9^{+0.8}_{-0.8}\%$	$0.8^{+0.6}_{-0.6}$	$0.8^{+0.5}_{-0.5}\%$	$0.92 \pm 0.02\%$
$\mathcal{R}(Z\gamma/Z)_{\ell}$	$6.0^{+4.6}_{-4.4}\%$	$3.3^{+2.7}_{-2.7}$	$4.3^{+2.5}_{-2.4}\%$	$2.42 \pm 0.04\%$
$\mathcal{R}(W\gamma/Z\gamma)_{\ell}$	$1.4^{+1.8}_{-1.3}$	$2.5^{+2.7}_{-2.4}$	$1.9^{+2.0}_{-1.3}$	4.00 ± 0.07
$\mathcal{R}(W/Z)_{\ell}$	$9.8^{+1.2}_{-1.2}$	$10.2^{+0.9}_{-0.9}$	$10.0^{+0.7}_{-0.7}$	10.69 ± 0.22

These cross section ratios are sensitive to anomalous couplings of of the W and Z bosons.

From the absolute cross section measurements of $W\gamma$ and $Z\gamma$, we obtain direct limits on the $WW\gamma$, $ZZ\gamma$ and $Z\gamma\gamma$ anomalous couplings of the W boson and Z boson.

For the W boson we obtain direct limits on the anomalous couplings in the muon, electron and combined $\mu + e$ channels of:

$W\gamma$ coupling	Muon Channel	Electron Channel	Combined $\mu + e$ Channel
$\Delta\kappa\ (\lambda = 0)$	$0.0^{+7.1}_{-6.6}$	$0.0^{+5.7}_{-5.2}$	$0.0^{+5.3}_{-4.8}$
$\lambda\ (\Delta\kappa = 0)$	$0.0^{+3.2}_{-3.2}$	$0.0^{+2.5}_{-2.5}$	$0.0^{+2.3}_{-2.4}$
$\Delta\kappa\ (\lambda = 0\ \ 95\% CL)$	$-9.0 < \Delta\kappa < +9.4$	$-7.2 < \Delta\kappa < +7.7$	$-6.5 < \Delta\kappa < +7.0$
$\lambda\ (\Delta\kappa = 0\ \ 95\%\ \mathrm{CL})$	$-4.3 < \lambda < +4.2$	$-3.5 < \lambda < +3.4$	$-3.1 < \lambda < +3.1$

The muon channel limits obtained on the static limit higher-order electromagnetic moments of the W boson are:

$$\frac{\mu_W}{\mu_W^o} \equiv g_W = 2.0^{+4.9}_{-4.8}\ (stat + syst) \qquad (Q_W^e/Q_W^{eo} = 1)$$

$$\frac{Q_W^e}{Q_W^{eo}} \equiv q_W^e = 1.0^{+7.5}_{-7.1}\ (stat + syst) \qquad (\mu_W/\mu_W^o = 2)$$

$$\frac{\langle R_W^2 \rangle}{\bar{\lambda}_W^2} \equiv r_W^2 = 1.0^{+4.9}_{-4.8}\ (stat + syst) \qquad (Q_W^e/Q_W^{eo} = 1)$$

The 95% CL limits on these quantities are:

$$-6.5 < \frac{\mu_W}{\mu_W^o} - 2 \equiv g_W - 2 < +6.6 \qquad (Q_W^e/Q_W^{eo} = 1\quad 95\% CL)$$

$$-9.7 < \frac{Q_W^e}{Q_W^{eo}} - 1 \equiv q_W^e - 1 < +10.0 \qquad (\mu_W/\mu_W^o = 2\quad 95\% CL)$$

$$-6.5 < \frac{\langle R_W^2 \rangle}{\bar{\lambda}_W^2} - 1 \equiv r_W^2 - 1 < +6.6 \qquad (Q_W^e/Q_W^{eo} = 1\quad 95\% CL)$$

The limits $g_W - 2$, $q_W^e - 1$, and $r_W^2 - 1$ in terms of $\Delta\kappa$ with $\lambda = 0$ are identical to the limits on $\Delta\kappa$. Likewise the limits on $g_W - 2$, $q_W^e - 1$, and $r_W^2 - 1$ in terms of λ with $\Delta\kappa = 0$ are identical to the limits on λ. For the electron channel, the limits are:

$$\frac{\mu_W}{\mu^o_W} \equiv g_W = 2.0^{+3.9}_{-3.9}\ (stat + syst) \qquad (Q^e_W/Q^{eo}_W = 1)$$

$$\frac{Q^e_W}{Q^{eo}_W} \equiv q^e_W = 1.0^{+5.9}_{-5.6}\ (stat + syst) \qquad (\mu_W/\mu^o_W = 2)$$

$$\frac{\langle R^2_W \rangle}{\lambda^2_W} \equiv r^2_W = 1.0^{+3.9}_{-3.9}\ (stat + syst) \qquad (Q^e_W/Q^{eo}_W = 1)$$

The 95% CL limits on these quantities are:

$$-5.3 < \frac{\mu_W}{\mu^o_W} - 2 \equiv g_W - 2 < +5.4 \qquad (Q^e_W/Q^{eo}_W = 1 \ \ 95\% CL)$$

$$-7.8 < \frac{Q^e_W}{Q^{eo}_W} - 1 \equiv q^e_W - 1 < +8.1 \qquad (\mu_W/\mu^o_W = 2 \ \ 95\% CL)$$

$$-5.3 < \frac{\langle R^2_W \rangle}{\lambda^2_W} - 1 \equiv r^2_W - 1 < +5.4 \qquad (Q^e_W/Q^{eo}_W = 1 \ \ 95\% CL)$$

while for the combined $\mu + e$ channel limits are:

$$\frac{\mu_W}{\mu^o_W} \equiv g_W = 2.0^{+3.6}_{-3.6}\ (stat + syst) \qquad (Q^e_W/Q^{eo}_W = 1)$$

$$\frac{Q^e_W}{Q^{eo}_W} \equiv q^e_W = 1.0^{+5.6}_{-5.2}\ (stat + syst) \qquad (\mu_W/\mu^o_W = 2)$$

$$\frac{\langle R^2_W \rangle}{\lambda^2_W} \equiv r^2_W = 1.0^{+3.6}_{-3.6}\ (stat + syst) \qquad (Q^e_W/Q^{eo}_W = 1)$$

The 95% CL limits on these quantities are:

$$-4.8 < \frac{\mu_W}{\mu^o_W} - 2 \equiv g_W - 2 < +4.9 \qquad (Q^e_W/Q^{eo}_W = 1 \ \ 95\% CL)$$

$$-7.0 < \frac{Q^e_W}{Q^{eo}_W} - 1 \equiv q^e_W - 1 < +7.4 \qquad (\mu_W/\mu^o_W = 2 \ \ 95\% CL)$$

$$-4.8 < \frac{\langle R^2_W \rangle}{\lambda^2_W} - 1 \equiv r^2_W - 1 < +4.9 \qquad (Q^e_W/Q^{eo}_W = 1 \ \ 95\% CL)$$

For saturation of unitarity, these results are sensitive to a compositeness scale of $\Lambda_W \geq 1.0$ TeV and probe possible internal structure of the W boson at a distance scale of order $\leq 2.0 \times 10^{-4}$ fm at 95% CL.

For a compositeness scale $\Lambda_Z = 500$ GeV the muon channel limits obtained on h^Z_{30} and h^Z_{40} channel $Z\gamma$ are:

$$\begin{array}{rcll}
h^Z_{30,10} & = & 0.0^{+10.9}_{-10.8} & (h^Z_{40}, h^Z_{20} = 0) \\
h^Z_{40,20} & = & 0.0^{+2.9}_{-2.9} & (h^Z_{30}, h^Z_{10} = 0) \\
-13.1 & < h^Z_{30}, h^Z_{10} < & +13.2\ \dagger & (h^Z_{40}, h^Z_{20} = 0, \quad 95\%\ CL) \\
-3.5 & < h^Z_{40}, h^Z_{20} < & +3.5\ \dagger & (h^Z_{30}, h^Z_{10} = 0, \quad 95\%\ CL)
\end{array}$$

The limits on these anomalous couplings obtained using the combined $\mu + e$ channel measurements are:

$$\begin{array}{rcll}
h^Z_{30,10} & = & 0.0^{+7.8}_{-7.7} & (h^Z_{40}, h^Z_{20} = 0) \\
h^Z_{40,20} & = & 0.0^{+2.1}_{-2.1} & (h^Z_{30}, h^Z_{10} = 0) \\
-9.2 & < h^Z_{30}, h^Z_{10} < & +9.4\ \dagger & (h^Z_{40}, h^Z_{20} = 0, \quad 95\%\ CL) \\
-2.5 & < h^Z_{40}, h^Z_{20} < & +2.5\ \dagger & (h^Z_{30}, h^Z_{10} = 0, \quad 95\%\ CL)
\end{array}$$

For the limits on $ZZ\gamma$ anomalous couplings at the other compositeness scales, $\Lambda_Z = 250, 750$ GeV, see the Tables 9.8 and 9.10. Note that the limits marked with † violate unitarity. Note also that the limits on anomalous $Z\gamma\gamma$ couplings are a factor of 1.05 greater than the respective couplings for $ZZ\gamma$.

For saturation of unitarity, these results are sensitive to a compositeness scale of $\Lambda_Z \geq 300 - 500$ GeV and probe possible internal structure of the Z boson at a distance scale of order $\leq 4 - 7 \times 10^{-4}$ fm at 95% CL.

The experimental results obtained and presented here are in good agreement with the Standard Model, and represent significant new limits on the $WW\gamma$, and $Z\gamma\gamma$ anomalous couplings of the W and Z bosons. We anticipate improving the measurements of $W\gamma$ and $Z\gamma$ cross sections with data obtained from future Tevatron collider runs, as well as improving the limits on the anomalous coupling parameters for $W\gamma$ by fitting the observed E_T^γ distribution to the predicted E_T^γ spectrum.

Appendix A

Electromagnetic Clustering Algorithm

The procedure used to form EM clusters is

- A list of all towers with E_T above the seed tower threshold is made, where the E_T is calculated using the event vertex location and the centroid of the EM calorimeter at roughly shower maximum.
- A list of towers with E_T over threshold is made (threshold = 0.05 GeV).

1 The highest E_T seed tower is removed from the list of seeds, as well as from the list of towers over threshold. This tower becomes the base tower for this EM cluster.

2 The list of towers over threshold is searched for towers that are adjacent to a tower in the cluster (i.e. any of the 8 towers surrounding the current tower). If the distance to the seed tower is less than 4 towers in eta and 2 towers in phi in the CEM, the tower is added to the cluster. In other regions of the calorimeter this distance parameter is different. Also, the new tower being considered for addition to the cluster must have a ratio of E_T with the current tower of less than 1, in order to prevent EM clusters being formed with valleys in them. If a tower is added to the cluster, it is removed from the list of towers over threshold, and from the list of seed towers.

3 Steps **1** and **2** above are repeated recursively until there are no more towers over threshold that satisfy the requirements.

4 Once the cluster is formed, it is kept if the total E_T of the cluster is greater than the sum value, by default 5 GeV, and the ratio of the Hadronic to EM energy of the cluster is smaller than 0.10.

- The next highest E_T seed tower is then picked, and steps **1-4** are recursively applied until there are no more clusters found.

Appendix B

Selection of the Jet-20 Event Sample

The Jet-20 sample was formed from a 4.2 pb^{-1} sample of inclusive jet data collected during the run. The Jet-20 trigger required an uncorrected Jet with $E_T > 20$ GeV, and was pre-scaled to record one of every 300 events that satisfied the trigger.

We impose further requirements on the Jet-20 events:

- $|Z_{\mathrm{vertex}}| < 60\ cm$
- $\not\!\!E_T < 20.0$ GeV, $\not\!\!E_T$ significance, $\sigma_{\not E_T} < 2.4$. These cuts were imposed to suppress badly mis-measured events, for instance when one jet of a di-jet event is centered on a calorimeter crack and a significant portion of its energy is not detected.
- At least three jets in a Jet-20 event.

- The energy of the jets is corrected [63] for the EM/Hadronic energy response nonlinearity. An absolute energy scale correction is made for Jet P_T dependent calorimeter non-linearity.

- Require that at least one of the two leading jets be in the central ($|\eta_{\text{det}}| < 1.1$) region of the detector, the other central or plug ($|\eta_{\text{det}}| < 2.4$).

- For the two leading jets, require that each corrected jet have $E_T^J > 15.0$ GeV and that $M_{JJ} > 40.0\ GeV/c^2$.

Bibliography

[1] S. J. Brodsky, R.W. Brown, Phys. Rev. Lett. **49** 966 (1982).

[2] R.W. Robinett, Phys Rev **D28** 1185 (1983).

[3] J. P. Eboli, Angela V. Olinto, Phys. Rev. **D38** 3461 (1988).

[4] F. Abe *et al.*, Phys. Rev. Lett. **64**, 152 (1990); F. Abe *et al.*, Phys. Rev. Lett. **68**, 3398 (1992)

[5] F. Abe *et al.*, Phys. Rev. Lett. **62**, 1005 (1989); F. Abe *et al.*, Phys. Rev. D **44**, 29 (1991); F. Abe *et al.*, Phys. Rev. Lett. **69**, 28 (1992); P. Derwent, Ph.D. thesis, University of Chicago (1990); R. Swartz, Jr., Ph.D. thesis, University of Illinois at Urbana-Champaign (1993)

[6] U. Baur and D. Zeppenfeld, Nucl. Phys. **B308** 127 (1988).

[7] U. Baur, E. L. Berger, Phys Rev **D41** 1476 (1990)

[8] U. Baur and D. Zeppenfeld, Phys. Lett. **B201** 383 (1988)

[9] K. Hagiwara et. al. Nucl. Phys. **B282** 253 (1987)

[10] U. Baur and E.L. Berger, Phys. Rev. D **47**, 4889 (1993).

[11] F. Boudjema, private communication via S. Errede.

[12] A. Barroso et al. Z. Phys. **C28** 149 (1985)

[13] U. Baur, private communication.

[14] J. M. Cornwall, D. N. Levin and G. Tiktopoulos, Phys. Rev. Lett. **30** 1268 (1973); Phys. Rev. **D10** 1145 (1974); C. H. Llewellyn Smith, Phys. Lett. **46B** 233 (1973); S. D. Joglekar, Ann. of Phys. **83** 427 (1974).

[15] "The CDF Detector: An Overview.", F. Abe, et al., Nucl. Inst. and Meth. **A271**:387-403, (1988).

[16] "The CDF Vertex Time Projection Chamber System.", F. Abe, et al., Nucl. Inst. and Meth. **A268**:75-91, (1988).

[17] "Design and Construction of the CDF Central Tracking Chamber", F. Bedeschi, et al., Nucl. Inst. and Meth. **A268**:50-74, (1988).

[18] "The CDF Central Electromagnetic Calorimeter", L. Balka, et al., Nucl. Inst. and Meth. **A267**:272-279, (1988).

[19] "The CDF Central and Endwall Hadron Calorimeter", G. Apollinari, et al., Nucl. Inst. and Meth. **A267**:301-314, (1988).

[20] "CDF Central Muon Detector", G. Ascoli, et al., Nucl. Inst. and Meth. **A268**:33-40, (1988).

[21] F. Abe et al., Phys. Rev. Lett. **64** 152 (1990); F. Abe et al., Phys. Rev. **D44**, 29 (1991); P. Derwent et al., **CDF-1107**; P. Derwent et al., **CDF-1254**; P. Derwent and M. Miller, **CDF-1166**; M. Miller, **CDF-1086**; F. Abe et al., Phys. Rev. Lett. **69** 28 (1992); S. Eno et al., **CDF-1349**; S. Eno et al., **CDF-1629**; R. Swartz and D. Kardelis, **CDF-1220**; A. Byon et al., **CDF-1263**; D.A. Smith and R. Swartz, **CDF-1259**

[22] C. Grosso-Pilcher and S. White, **CDF-1202**.

[23] "A Two Level FASTBUS Based Trigger System for CDF", D. Amidei, et al., Nucl. Inst. and Meth. **A269**:51-62, (1988).

[24] T. Liss, "Luminosity Monitoring and Beam-Beam Counter Performance" **CDF-552** (1987)

[25] "CDF Central Muon Level 1 Trigger Electronics", G. Ascoli, et al., Nucl. Inst. and Meth. **A269**:63-67, (1988).

[26] G. W. Foster, et al., Nucl. Inst. and Meth. **A269** 93, (1988).

[27] A. Byon et al., Cosmic Filtering of Central Muon Events, **CDF-1260**.

[28] F. Abe, et al Phys. Rev. D **44** 29 (1991)

[29] A. Gauthier, *"Efficiency of the Level 1 Central Muon Trigger"*, **CDF-937** (1991); A. Gauthier and D. Kardelis, *"Efficiency of the Level 2 Central Muon Trigger"*, **CDF-1106** (1990); A. Gauthier, *Efficiency of the Level 3 Central Muon Trigger*, **CDF-1145**. (1990) A. Gauthier, *Milestones of the Central Muon Trigger*, **CDF-1029**.

[30] D. Kardelis, *Efficiency of the "Standard" Muon Tower Calorimeter Cuts for W/Z Muon Analysis*, **CDF-1301**.
D. Kardelis, *A Study of the CTC-CMU Matching Cut Efficiency for W/Z Muon Analysis.* **CDF-1336**

[31] F. Abe et al., Phys. Rev. **D43**, 2070 (1991); F. Abe et al., Phys. Rev. Lett. **65** 2243 (1990); W. Trischuk, Ph.D. thesis, Harvard University (1990); P. Schlabach, Ph.D. thesis, University of Illinois at Urbana-Champaign (1990).

[32] F. Abe *et al.*, Phys. Rev. Lett. **63**, 720 (1989); H. Keutelian, Ph.D. thesis, University of Illinois at Urbana-Champaign (1990).

[33] G. Peter Lepage, J. Comp. Phys. **27**, 192-202 (1978), Academic Press (1978); G. Peter Lepage, CLNS-80/447 (1980).

[34] PDFLIB version 3.11, H. Plothow-Besch, Computer Phys. Commun. **75**, 396 (1993); H. Plothow-Besch, CERN Report W5051, (1992).

[35] M. Kobayashi and M. Maskawa, Prog. Theor. Phys. **49**, 652 (1973).

[36] The VVJET Monte Carlo, U. Baur, E.W.N. Glover and J.J. van der Bij, Nucl. Phys. B **318**, 106 (1989).

[37] ISAJET Monte Carlo version 6.24, F.E. Paige and S.D. Protopopescu, BNL Technical Report No. 38034, 1986 (unpublished).

[38] PAPAGENO Monte Carlo version 3.12, I. Hinchliffe, (to be published).

[39] PYTHIA version 5.4, T. Sjöstrand, Computer Phys. Commun. **39**, 347 (1986); T. Sjöstrand and M. Bengtsson, Computer Phys. Commun. **43**, 367 (1987); H.-U. Bengtsson and T. Sjöstrand, Computer Phys. Commun. **46**, 43 (1987).

[40] R.G. Wagner, Comp. Phys. Commun. **70**, 15 (1992); see also F.A. Berends, J.P. Revol and R. Kleiss, Z. Phys. C **27**, 155 (1985); F.A. Berends and R. Kleiss, *ibid.* C **27**, 365 (1985).

[41] C. Campagnari, **CDF-1025**.

[42] S. Errede, "Methodology for the Measurement of $W\gamma$ and $Z\gamma$ in the Muon Channel at CDF", **CDF-1732** (1992).

[43] F. Abe et al., Phys. Rev. Lett. **66** 2951 (1991); F. Abe et al., Phys. Rev. Lett. **67** 2937 (1991); B. Winer, Ph.D. thesis, University of California at Berkeley (1991); J. Ng, Ph.D. thesis, Harvard University (1991).

[44] M. Mangano, "The Unweighting of Matrix Element Monte Carlos", **CDF-1665**

[45] P.B. Arnold and M.H. Reno, Nucl. Phys. B **319**, 37 (1989); P.B. Arnold and R.P. Kauffman, Nucl. Phys. B **349**, 381 (1991).

[46] M. Diemoz, F. Ferroni, E. Longo, and G. Martinelli, Z. Phys. C **39**, 21 (1988).

[47] A.D. Martin, R.G. Roberts and W.J. Stirling, Phys. Lett. B **206**, 327 (1989).

[48] P.N. Harriman, A.D. Martin, R.G. Roberts and W.J. Stirling, Phys. Rev. D **42**, 798 (1990).

[49] A.D. Martin, R.G. Roberts and W.J. Stirling, Phys. Rev. D **47**, 867 (1993).

[50] J.G. Morfin and Wu-Ki Tung, Z. Phys. C **52**, 13 (1991).

[51] Review of Particle Properties, Phys. Rev. D **45**, III.39, (1992).

[52] F. Abe *et al.*, to be published in Phys. Rev. D., D. Benjamin PhD. thesis, Tufts University (1994), M. Roach PhD. thesis Tufts University (1994)

[53] U. Baur, S. Errede and J. Ohnemus, Phys. Rev. D**48** 4103 (1993).

[54] Review of Particle Properties, Phys. Rev. D **45**, II.25, (1992).

[55] F. Boudjema, K. Hagiwara, C. Hamazaoui and K. Numata, Phys. Rev. D **43**, 2223 (1991); W.J. Marciano and A. Queijeiro, Phys. Rev. D **33**, 3449 (1986).

[56] MINUIT, F. James and M. Roos, CERN Report D506, (1988).

[57] G.L. Kane, J. Vidal and C.P. Yuan, Phys. Rev. D**39**, 2617 (1989).

[58] F. Herzog, Phys. Lett. B**148**, 355 (1984); F. Herzog, *erratum, ibid.* B**155**, 468 (1984); J.C. Wallet, Phys. Rev. D**32**, 813 (1985).

[59] M. Suzuki, Phys. Lett. B**153**, 289 (1985). **CDF-1665** (1992).

[60] J. Alitti, *et al.*, Phys. Lett. B **277**, 194 (1992).

[61] P. Méry, S.E. Moubarik, M. Perottet and F.M. Renard, Z. Phys. C **46**, 229 (1990).

[62] O. Adriani, *et al.*, Phys. Lett. B **297**, 469 (1992). and J. Busenitz, private communication via S. Errede.

[63] L. Keeble *New jet correction function Qdjsco Version 2.0* **CDF-1513** (1991)

Vita

[redacted] [redacted] this researcher set out to find out why things exist. In short order his parents became exasperated by his continually repeated "Why is ...?", and sentenced him to public school. Emerging from this travail unscathed, a few years were spent at New Mexico State University trying to learn everything. A combination of the finite length of the human lifespan, and the unwillingness of the University to allow a penta-major forced Chris to pick **one**. The agonizing choice was made, and after a few more semesters, in a B.S. in physics was the result. Going on to Gradual School, Chris gradually decided not be be in school any more, and finished, much to the delight of his parents.